DEPARTMENT OF PHYSICS
UNIVERSITY OF JYVÄSKYLÄ
RESEARCH REPORT No. 1/2017

# ON-CHIP PURIFICATION OF ARC-DISCHARGE SYNTHESIZED MULTIWALLED CARBON NANOTUBES VIA MOBILE LIQUID INTERFACE

**BY**
**MATTI HOKKANEN**

Academic Dissertation
for the Degree of
Doctor of Philosophy

*To be presented, by permission of the*
*Faculty of Mathematics and Science*
*of the University of Jyväskylä,*
*for public examination in Auditorium KEM 1 of the*
*University of Jyväskylä on January 20th, 2017*
*at 12 o'clock noon*

Jyväskylä, Finland
January 2017

# Preface

The content of this thesis is based on research that was first envisioned during my Master's work in 2011 and before, and then carried out during my 2012-2016 graduate studies at the Univ. of Jyväskylä Dept. of Physics and Nanoscience center.

I am very grateful to my thesis supervisor, Prof. Markus Ahlskog for his tutelage and support during our common journey since 2008 that first lead to my Master's thesis, and then, to Doctorate. Not only has this given me an opportunity to learn a lot about science, but also a privilege to meet and work with some truly wonderful people who have helped me along my way on numerous occasions. Sadly, only some of these people can be properly recognized here.

First, my past and present teammates in the MolTech research group deserve great credit. Drs. Jarkko Lievonen, Davie Mtsuko, Olli Herranen and Peerapong Yotprayoonsak taught me everything I know about the practicalities of nanoscience, from cleanroom work to sample fabrication and imaging techniques. Likewise, I mention my close colleague, Mr. Shao Dongkai, with whom I have learned together.

I also recognize past Master's students and interns of the MolTech group, Mrs. Ilkka Pekkala, Hannu Pasanen, Joonas Saari and Antti Lukkarinen who have worked under my supervision in various projects; unfortunately, I could not always give due attention to your work. And how could I possibly not mention Ms. Saara Lautala, whose efforts were so vital in preparation of the last papers incorporated in this thesis? Truly, I could not have done this without her hard work.

Of my other co-workers, I must mention Mr. Roope Lehto and Prof. Jussi Timonen, whose efforts enabled us to carry out the study described in the first paper of this thesis. For the other two papers, I humbly recognize the assistance of Dr. Tuomas Turpeinen, who helped me so much without any incentive or requirement. Prof. Matti Haukka, Dr. Margarita Bulatova and Dr. Elina Laurila from the Dept. of Chemistry are recognized for their help during the latter stages of my thesis work.

From the Nanoscience center, laboratory engineers Mr. Antti Nuotajärvi, Mr. Tarmo Suppula and Dr. Kimmo Kinnunen have always been friendly and helpful towards me; their continued technical support has been vital to this work. Similarly, the practicalities of this work could not have been managed without our helpful departmental office staff; I really hope the future works out well for you all.

This work would not have been possible without support from our colleagues abroad. At the Univ. of Witwatersrand, South Africa, Mr. Christopher Coleman and

Dr. Rudolph Erasmus carried out Raman measurements on our samples, expanding upon the efforts of Mr. Juha Koivistoinen here in Jyväskylä. In the Univ. of Karlstad, Sweden, Dr. Krister Svensson lended us his unique instrumentation and expertise. And finally, Prof. Emmanuel Flahaut from CIRIMAT, Univ. of Toulouse, kindly provided us with materials for the experiments in the final paper.

During troubled times, I have also benefited greatly from the support of several senior colleagues. Profs. Markku Kataja and Timo Sajavaara deserve recognition for serving in the follow-up group of my Ph. D. project; those discussions brought great relief to me. Drs. Andreas Johansson, Juha Merikoski, Sami Räsänen and Pekka Koskinen have always had time for my concerns, whether scientific or personal. This was by no means an easy path for me to tread, and I believe the reassurance and encouragement you provided was what ultimately helped me over the worst.

From my years here at the Univ. of Jyväskylä, I will always remember my friends and student colleagues. Mr. Jussi Viinikainen was my close friend throughout my undergraduate years, while Mr. Kosti Tapio became my closest co-worker during my doctoral studies. Both of them have helped me in numerous ways over these years, not least with course exercise problems. I would also like to thank my graduate student colleagues past and present, with whom I've shared laboratories of the Nanoscience Center: Mr. Shen Boxuan, Mr. Geng Zhuoran, Dr. Yaolan Tian, Dr. Tommi Isoniemi, Dr. Svetlana Baieva, Mr. Andrii Torgovkin, Dr. Janne Lehtinen and Dr. Tero Isotalo. Thank you for creating that unique spirit of openness and collaboration that makes the Nanoscience Center such a special place.

I also wish to thank my family: my father, Markku, has always been very supportive of my academic endeavours, and is one of the people who have shared my burdens throughout this journey; my mother Eila, who, along with Eino, have always been welcoming of me coming to visit, and reminded me of the other things besides the thesis; and my brothers, Ville and Eemil; thank you!

Financial support enabling this Thesis work has been provided by the National Graduate School in Material Physics (NGSMP), the National Doctoral Programme in Nanoscience (NGS-NANO), and the Univ. of Jyväskylä Department of Physics. I gratefully acknowledge their patience on the matter.

Finally, as it is said that science is about standing on the shoulders of giants, so I also stand with not just the help of fellow scientists, but also educators and teachers who have cherished my ambitions. As such, I would like to dedicate this thesis to all the people who have taught me over the years: Eija, Eila, Anneli, Tuomo, Arto, Vilho, Yrjö, and everyone else; this is for you. I may not have always been able to answer your questions correctly, but as it turns out science is less about giving answers, and more of knowing to ask the right questions. Thank you all for what you do.

Jyväskylä, December 2016

Matti Hokkanen

# Abstract

Hokkanen, Matti
On-chip purification of arc-discharge synthesized multiwalled carbon nanotubes via mobile liquid interface
Jyväskylä: University of Jyväskylä, 2017, 132 p.
(Research report/Department of Physics, University of Jyväskylä,
ISSN 0075-465X; 1/2017)
ISBN 978-951-39-6916-5 (paper copy)
ISBN 978-951-39-6917-2 (e-print)
diss.

This thesis reports a novel approach for purification of carbon nanotube (CNT) samples deposited on smooth silicon substrates through a mobile liquid interface interacting with carbonaceous debris particles that contaminate the deposition. The method is based on physical interaction of the particles and the three-phase contact line via capillary interface forces, i.e. the surface tension, which results in the detachment of chemically indispersible colloids from the sample surface.

In the experiments reported in this work, we focus primarily on arc-discharge grown multi-walled carbon nanotubes, whose synthesis is particularly plagued by carbonaceous debris that is difficult to remove without harsh chemical treatments. The irregular debris particles are preferentially captured by the mobile contact line, while tubular CNTs are retained in large numbers due to their appreciably stronger adhesion. Our cleaning method has the added benefit that the intrinsic chemical properties of the CNTs are fully preserved, since no chemical treatments are needed; only prerequisite is the hydrophilic treatment of the underlying substrate, which on silicon wafers can be accomplished through oxygen plasma.

Various aspects of the cleaning process, including the effects of contact line velocity, chemical composition of the immersion liquid, and the CNT orientation relative to the liquid front are investigated in this thesis. Furthermore, atomic force microscopy (AFM) imaging and the image analysis methodology is discussed. Additionally, we demonstrate some research applications that directly benefit from our technique, e.g. microraman spectroscopy of individual carbon nanotubes, and nanomechanical investigation of suspended tubes via AFM-deflection measurements.

Theoretical treatment of the detachment process is presented in the framework developed for spherical microcolloids in existing works. In this model, the particle detachment is primarily attributed to the surface tension force. Other forces affecting the process include adhesion, which in liquid electrolyte medium can be estimated via the DLVO adhesion theory, and hydrophobic interactions.

We conclude that the particle detachment is qualitatively well-explained by the physical interactions at the contact line, while the selectivity of the process for the irregular debris particles in favor of the tubular CNTs probably stems from differences in the magnitude of the adhesion force. Chemical factors associated with the composition of the immersion liquid on the other hand seem to only have very limited effect on the quantitative cleaning result. Regarding to detachment of CNTs, orientation-dependent behavior is implied, with species oriented perpendicular to the advancing contact line reflecting the greatest probability to be retained. Overall, the detachment of all particles is found to increase with decreasing velocity of the liquid interface. These results are generally in qualitative agreement with existing works dealing with spherical microcolloids.

**Keywords** carbon nanotube, contact line, surface tension, wetting, surface chemistry, adhesion, atomic force microscopy

**Author**

Matti Hokkanen
Nanoscience Center
Department of Physics
University of Jyväskylä
Finland

**Supervisor**

Professor Markus Ahlskog
Nanoscience Center
Department of Physics
University of Jyväskylä
Finland

**Reviewers**

Prof. Marina Ruths
Department of Chemistry
University of Massachusetts Lowell
USA

Dr. Marko Burghard
Nanoscale Science Department
Max Planck Institute for Solid State Research, Stuttgart
Germany

**Opponent**

Prof. Oren Regev
Department of Chemical Engineering
Ben-Gurion University of the Negev, Beer Sheva
Israel

# Tiivistelmä (abstract in Finnish)

Hokkanen, Matti
On-chip purification of arc-discharge synthesized multiwalled carbon nanotubes via mobile liquid interface
Jyväskylä: University of Jyväskylä, 2017, 132 p.
(Research report/Department of Physics, University of Jyväskylä,
ISSN 0075-465X; 1/2017)
ISBN 978-951-39-6916-5 (nid.)
ISBN 978-951-39-6917-2 (verkkoj.)
diss.

Tässä väitöskirjatyössä esitetään uusi lähestymistapa piipinnoille valmistettujen hiilinanoputkinäytteiden (carbon nanotubes, CNT) puhdistamiseen hiilipohjaisista kuonapartikkeleista liikkuvan nesterajapinnan avulla. Menetelmä perustuu partikkelien ja nestepinnan väliseen fysikaaliseen kapillaarivuorovaikutukseen, eli pintajännitysvoimaan, kolmen faasin rajapinnalla, joka aiheuttaa nesteeseen kemiallisesti liukenemattomien kolloidien irtoamiseen näytepinnalta.

Keskitymme kokeellisessa työskentelyssä erityisesti valokaarisyntetisoituihin nanoputkiin, joiden synteesin yhteydessä syntyy runsaasti hiilipohjaisia kuonapartikkeleita joiden poistaminen on hankalaa ilman voimakkaita kemiallisia käsittelyjä. Muodoltaan epäsäännölliset partikkelit ensisijaisesti tarttuvat mobiiliin nesterajapintaan, kun taas putkimaiset hiilinanoputket jäävät enimmäkseen näytepinnalle voimakkaamman adheesiovoiman ansiosta. Puhdistusmenetelmämme erityinen etu on, että hiilinanoputkien kemialliset ominaisuudet säilyvät prosessissa muuttumattomana, sillä niiden kemiallisia käsittelyä ei tarvita; ainoana edellytyksenä on substraattipinnan hydrofiilisyyskäsittely, mikä piilevyjen tapauksessa voidaan helposti toteuttaa happiplasmalla.

Väitöskirjassa tutkitaan useita puhdistusprosessiin liittyviä tekijöitä, mukaan lukien kontaktirajapinnan nopeus, immersionesteen kemiallinen kompositio ja hiilinanoputkien tapauksessa niiden orientaatio rajapintaan nähden. Lisäksi käsittelemme kokeissa hyödynnettävää atomivoimamikroskopiaa (atomic force microscopy, AFM), sekä siihen liittyvää kuva-analyysimetodologiaa. Lopuksi esittelemme joitakin tutkimussovelluksia, jotka hyötyvät suoraan puhdistustekniikastamme, mukaan lukien

yksittäisten nanoputkien raman-spektroskopia sekä vapaasti roikkuvien putkien nanomekaanisten ominaisuuksien määrittäminen AFM-menetelmin.

Puhdistusprosessiin liittyvä teoreettinen käsittely perustuu aiemmissa töissä pallomaisille mikrokolloideille kehitettyyn teoriaan. Tässä mallissa partikkelin poistuma liitetään pääasiassa pintajännitysvoimaan. Tämän lisäksi prosessiin vaikuttavat hydrofobiset vuorovaikutukset, sekä adheesiovoima, joka nestemäisessä ympäristössä voidaan ilmaista nk. DLVO-teorian avulla.

Tutkimuksen loppupäätelmät ovat, että partikkelien poistuma pinnoilta on kvalitatiivisesti ymmärrettävissä kontaktilinjan fysikaalisten vuorovaikutusten pohjalta, ja prosessin selektiivisyys epäsäännöllisiin partikkeleihin on seurausta nanoputkiin verrattuna eroavasta adheesiovoimasta. Nesteen kemiaan liittyvät tekijät näyttävät toisaalta vaikuttavan verrattain vähän kvantitatiiviseen puhdistumistulokseen. Hiilinanoputkien poistuman osalta havaittiin orientaatioriippuvaista käyttäytymistä, jossa etenevän rajapinnan kanssa vastakkaisuuntaisesti suuntautuneet putket selvisivät todennäköisimmin näytepinnalta irtoamatta. Kaikkien partikkelien poistuma yleisesti kasvaa rajapinnan nopeuden hidastuessa. Nämä tulokset ovat yleisesti kvalitatiivisella tasolla yhteensopivia aiempien, pallomaisia mikrokolloideja käsittelevien tutkimusten kanssa.

**Avainsanat** carbon nanotube, contact line, surface tension, wetting, surface chemistry, adhesion, atomic force microscopy

# List of Publications

**A.I.** HOKKANEN, M. J., LEHTO, R., TAKALO, J., SALMELA, J., HAAVISTO, S., BYKOV, A., MYLLYLÄ, R., TIMONEN, J., AHLSKOG, M., *Depletion of carbon nanotube depositions and tube realignment in the spreading of sessile drops*. Colloids. Surf. A **482**, 624–630 (2015).

**A.II.** HOKKANEN, M. J., LAUTALA, S., SHAO, D., TURPEINEN, T., KOIVISTOINEN, J., AHLSKOG, M., *On-chip purification via liquid immersion of arc-discharge synthesized multiwalled carbon nanotubes*. Appl. Phys. A **122**, 634 (2016).

**A.III.** HOKKANEN, M. J., LAUTALA, S., FLAHAUT, E., AHLSKOG, M., *Experimental studies on the detachment of multi-walled carbon nanotubes by a mobile liquid interface*. Submitted for publication in Langmuir (2016).

## Author's contribution

This thesis is a compilation of three journal articles, as well as three additional written chapters of novelty value. The work highlights an entirely unprecedented approach on the purification of carbon nanotube depositions that has been fully conceptualized, developed and experimentally verified by the author of the thesis and his supervisor. Some related results have been previously published in the author's Master's thesis [48].
The author has had a dominant role in the execution of all practical research work presented in the thesis. This includes the design and preparation of all experiments and samples, execution of all preliminary and primary experimental work, as well as interpretation and analysis of all the experimental results, with the following exceptions:

In **A.I.**, the practical experiments were carried out in collaboration with R. Lehto. The orientation analysis of electron micrographs was done by J. Takalo. J. Timonen made significant input to the writing of the article.

In **A.II.**, the author directed and oversaw the sample preparation and primary experiments carried out by S. Lautala. The algorithm utilized in the image analysis method was initially developed by T. Turpeinen.
In **A.III.**, the author directed and oversaw the sample preparation and primary experiments carried out by S. Lautala.

In addition, the author of this work was also the primary author of each of the article publications incorporated in the thesis. The author wrote the initial draft of each publication, finalized them with his supervisor, and produced majority of the graphics and illustrations presented in them.

## Other publications to which the author has contributed:

WHITLOW, H. J., GORELICK, S., PUTTARAKSA, N., NAPARI, M., HOKKANEN, M. J., NORARAT, R., *Development of procedures for programmable proximity aperture lithography*. Nucl. Instr. Meth. Phys. Res. B **306**, 307–310 (2013).

# Contents

# Chapter 1

# Introduction

The carbon nanotube (CNT), i.e. a tubular arrangement of graphene (single sheet of graphite), has attracted a great deal of interest as a topic of scientific inquiry ever since its discovery in 1991. The interest owes largely to the unique properties of the CNTs, which arise from the confinement of a graphene sheet into a tubule. The confinement leads to discrete energy states along the circumference of the tube, while in the longitudinal direction the native properties of graphene are largely preserved.

Together with the periodic confinement, the intrinsically high aspect ratio of CNTs means that their properties are radically different in the axial and radial directions. The remarkable features along the tube axis include high tensile strength, elastic modulus and hardness [128]. However, when measured in other directions, the values of the mechanical parameters become more modest [121]; bending, compressive or torsional stress causes CNTs to yield relatively easily due their hollow structure. This anisotropy also applies to the thermal conductivity, which is extraordinarily high in the axial direction [93], but far more modest when measured radially.

The thermal stability of CNTs, estimated up to $2800\,\mathrm{C}^\circ$ in vacuum, is remarkable [115]. The saturated carbon chain of the CNT side wall is highly robust; yet, covalent chemical modification of both the sidewall and the end-tip is possible. The

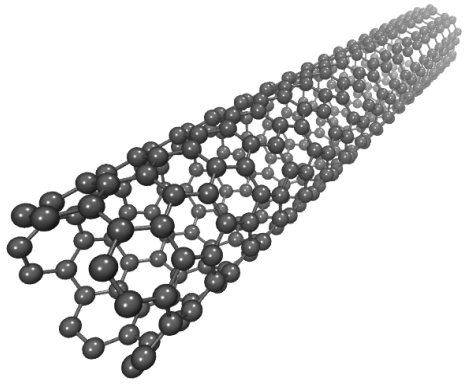

**FIGURE 1.1** Schematic of a single-walled carbon nanotube. Figure courtesy of Pekka Koskinen, used with permission.

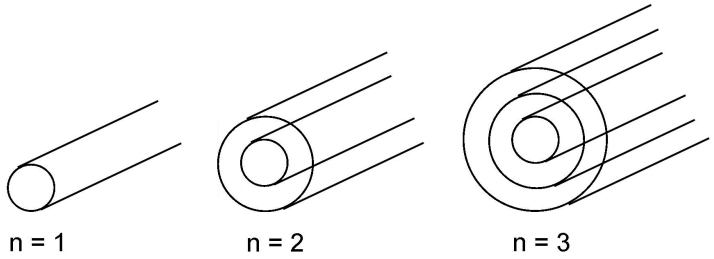


**FIGURE 1.2** Schematic structures of (a) single, (b) double and (c) triple-walled carbon nanotubes (CNTs). Tubes with more than one wall are collectively termed multi-walled carbon nanotubes (MWNTs). Figure courtesy of Peerapong Yotprayoonsak, used with permission (modified by the author).

one-dimensional nature of the tubes also brings about unique optical absorption properties; the absorbance of dense, vertically aligned carbon nanotube "forests" nears unity in a wide spectral range [81, 122], making them almost perfect black bodies, while individual carbon nanotubes can be Raman-active despite their small size. But perhaps the most noteworthy features of the CNTs are still found in their electric properties, which will be discussed separately.

CNTs can be broadly found in two distinct variants: single-walled and multi-walled, where the latter can be considered a concentric arrangement of individual tube shells that interact only weakly. Single-walled carbon nanotubes (SWNTs) often show the most remarkable properties; multi-walled carbon nanotubes (MWNTs) sometimes suffer from weak intershell interactions, that for example result to surprising reduction in their mechanical strength [38, 91]. Yet, the MWNTs have many redeeming features: some phenomena, such as telescopic extraction of the inner shells [23], are unique to the MWNTs, and the intershell interactions provide a rich field of study.

The past decade has seen the first signs of the CNTs breaking through as a credible candidate material for novel applications, however several technological challenges also remain before their large-scale industrial implementation in every-day products can be realized. Perhaps the most pressing of these, the availability of the material in sufficiently high quality and quantity, is quickly becoming rectified; this owes largely to the industrial-scale production of high-quality SWNTs, realized via evolution of the CVD growth technique which has greatly improved their availability [33]. Great progress has also been achieved in separation of different SWNT chiralities, which allows for uniformity in the tube properties.

Despite the high expectations and seemingly unlimited potential, the majority of established commercial applications of CNTs are still limited to the use of bulk, unorganized nanotubes as e.g. reinforcing agents in composite materials. While impressive in comparison to more traditional options, these materials still fall far short of the properties of the individual tubes, whose full potential cannot be realized until a high degree of control can be exerted upon the orientation of the tubes, either

during their deposition, or in-situ on the substrate.

For the purposes of electronic applications based on individual carbon nanotubes, CNTs synthesized with the arc-discharge method shows particular promise. Compared to CVD-grown tubes, the appreciably higher degree of crystalline uniformity translates to e.g. low electrical resistance of the devices fabricated out of arc-discharge grown material. This benefit, however, comes with a disadvantage of carbonaceous contamination by irregular debris, whose separation without altering the intrinsic properties of the nanotubes can be difficult.

**Description of this work**

In this work, we introduce a new method for purification of on-chip arc-discharge grown carbon nanotube depositions prepared on silicon surface via spin coating. The simple technique based on the mobile contact line of a liquid body allows for efficient detachment of irregular particulate debris originating from the arc-discharge synthesis while the CNTs themselves are retained on the surface in large numbers.

In the papers presented in this Thesis, the scrutiny is on multi-walled tubes, motivated primarily by experiments such as Raman spectroscopy and electrical transport measurements of individual tubes that benefit from clean samples and have previously been mostly focused on single-walled tubes. Although fundamentally compatible with all kinds of carbon nanotubes, the cleaning technique here is thus trialed for the purposes of selective separation of carbonaceous debris intrinsic to arc-discharge MWNTs.

In this introductory section, the historical background and key synthesis methods of CNTs are summarized briefly, and the difficulty of obtaining pure carbon nanotube depositions discussed. In the second and third chapters, some fundamental concepts that feature at the background and motivation of this work at large are presented in introductory manner. The fourth chapter discusses the research papers incorporated in this thesis, with emphasis placed on the experimental methodology and the key results. The fifth chapter is dedicated to theoretical considerations of the experimental work, as well as comparison with similar studies on colloidal particles. In the sixth chapter, the imaging and image analysis methodology utilized in the latter papers is introduced. The seventh chapter deals with the research applications devised for the cleaning technique, while the final, eight chapter is for a summary of the work.

## 1.1 History of carbon nanotubes

The discovery of carbon nanotubes is widely credited to Sumio Iijima, who in 1991, while working on the synthesis of fullerenes, also produced tubular species in his reactor [55]. It is a curious coincidence that CNTs were first synthesized in such a

serendipitous manner in conjunction with fullerenes, given that fullerenes themselves were initially also discovered by chance.

Although Iijima's work brought CNTs into the focal point of international attention, it is now recognized that there have been earlier mentions of CNTs in the scientific literature. Already in 1952 there was a research article in a soviet journal by Radushkevich and Lukyanovich where micrographs of tubular carbonaceous structures in the 50 nanometer diameter range were published [94], however the work was of course written in russian, and poorly accessible by the international community. In 1976, Oberlin *et al.* published about tubular carbon fibers synthesized via chemical vapor growth technique [89]. One of the co-authors of this paper, Morinobu Endo, is credited with the realization of the CVD-growth of CNTs, and the industrial process utilized today is referred as the Endo-process. In 1979, Abrahamson *et al.* presented a conference paper about growth of similar tubes via electric arc-discharge [1]. Later, in 1981, another soviet group characterized CNTs in more detail with TEM and electron diffraction, and argued that the structure might consist of wrapped-up graphene sheets. They noted that several different chiral arrangements could thus be possible, pointing out what we now refer as armchair and chiral nanotubes [59].

A lot of these early discoveries were associated with carbon fibers in general; they went largely unnoticed, and few parallels were drawn between them. It was the discovery of fullerenes (Fig. 1.3) in 1985 by Kroto *et al.* that initiated carbon nanomaterials as an independent research topic [70]. The expectations associated with fullerenes also latched onto Iijima's report, and sparked a global interest. The tubes initially observed by Iijima were from 5 to 20 nanometers in diameter, and therefore, multi-walled, but already a year later, in 1992, first predictions of the remarkable electrical properties of single-walled carbon nanotubes were published [80]. First SWNTs were intentionally produced in 1993, independently by the groups of Donald Bethune and Iijima [12, 56], through the use of transition-metal catalysts in arc-discharge.

Carbon nanotubes also exist in nature, albeit in minute quantities. They have been found in the combustion products of various organic compounds, as well as in ambient air, as irregular aggregates [84]. The presence of carbon nanotubes has also been implied in the famous Damascus steel that medieval blacksmiths used to forge sword blades in Near East [98]. The CNTs in this case were probably originated from biomass during the carburizing process of the steel, for it is now known that CNTs can also be derived from natural plant fibers [41]. The presence of carbon nanotubes in the Damascus steel is thought to have contributed to the legendary strength of weapons forged from it [87].

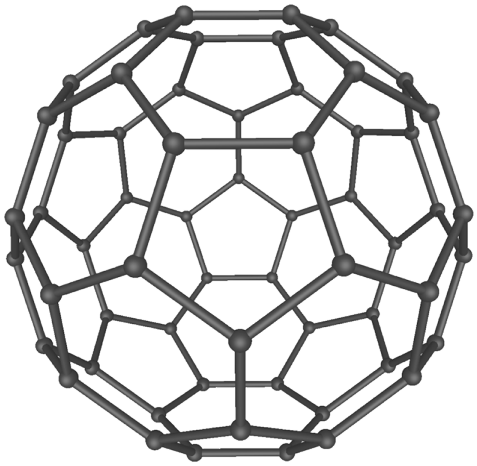

**FIGURE 1.3** $C_{60}$ fullerene, a.k.a. Buckminsterfullerene. © Michael Ströck, Wikimedia Commons / CC-BY-SA-3.0

## 1.2 Carbon nanotube synthesis

There are three well-established methods for the synthesis of carbon nanotubes. Of these methods, chemical vapor deposition (CVD) is by far the most pronounced one, because it is the only one that can at the present produce nanotubes at industrial quantities. CVD is a thermal vapor-phase method where the tubes are grown directly on a substrate with the help of metal catalyst particles. The substrate is typically silicon-based, for example $Si/SiO_2$ or $Si/Si_3N_4$, and Fe, Co and Ni are typically used as the catalyst [82]. The substrates are enclosed within a CVD furnace consisting of a quartz tube and heating apparatus, where carbon source gas (e.g. alcohol vapor) is fed in mixture with inert carrier gas (e.g. Ar). At a temperature of $900 - 1200\,^{\circ}\mathrm{C}$, the hydrocarbon decomposes in the presence of the catalyst, and carbon nanotubes grow from the catalyst particles. The CVD-method is primarily used in the growth of single-walled carbon nanotubes, although multi-walled tubes can be grown as well [8].

Depending on the growth parameters, the tubes may grow vertically from the catalyst particles, or along the sample surface. The vertical approach is primarily used in commercial, industrial-scale production with a plasma-enhanced process. Alternatively, vertical growth can also be used to synthesize thick nanotube "forests" up to several millimeters in height that are useful for e.g. device fabrications [46, 99]. Lateral growth is of use in *in-situ*, laboratory-scale applications where the tubes are synthesized directly on the final substrates, in for example growing them over etched openings to create suspended structures (see, for example, [85]).

CVD-method has the benefit of producing clean single-walled nanotubes relatively free from carbonaceous debris. The diameter of the CNTs generally relates to the particle size, and precise control of the tube diameter and chirality is possible with the help of "seed tubes" [109]. The drawback is that the individual tubes CVD-grown,

particularly MWNTs, tend to suffer from crystalline imperfections. Aside from the growth itself, imperfections may also arise during the subsequent processing steps required to remove the catalyst particles that can make up a significant fraction of the product mass. This generally requires oxidative processes or chemical treatments that may further degrade the CNT structure [52].

Arc-discharge method is the oldest approach for synthesizing CNTs; this approach, previously utilized in the synthesis of fullerenes, lead to Iijima's discovery in 1991 [55]. In arc-discharge growth, two separate graphite electrodes are placed within a chamber filled with inert gas such as He or Ar, and a high current in the order of $100\,\mathrm{A}$ is passed through them, resulting into discharge by an electric arc. Multi-walled carbon nanotubes are then found to have formed on the cathode electrode from the sublimated graphite, but if catalyst particles are added, single-walled tubes can then also be synthesized [12, 56].

A major drawback is that a lot of carbonaceous debris, e.g. carbon nanoparticles, graphite grains, fullerenes and amorphous carbon, is formed along with the nanotubes that cannot be easily separated [52]. Also, relatively little control can be had over the chirality and diameter of the tubes that form via arc-discharge. However, tubes synthesized in this way suffer from far fewer structural structural defects than CVD-grown tubes [32].

CNTs can also be formed through the means of a laser beam that is focused onto a graphite target compounded with catalyst particles under inert atmosphere [43]. The process takes place at elevated temperatures (about $1200\,^{\circ}\mathrm{C}$): the laser beam evaporates the target, and CNTs condensate onto a cold finger nearby. Similar laser irradiation was originally utilized in the initial synthesis of fullerenes [70]. It has been demonstrated that the diameter and the chirality of the tubes are specific to the synthesis parameters [114], but like arc-discharge growth, the method is however poorly scalable, and suffers from limited yield [32].

## 1.3 Existing methods for purification of CNTs

As mentioned before, the majority of researchers working in the nanotube field deal with CVD-grown carbon nanotubes, and in particular single-walled ones. Owing to the well-established growth and harvesting techniques, this type of material can be obtained in a relatively pure, refined form, and the throughput of these methods is sufficient for large-scale, commercial production. For this reason, much of the technical and industrial interest on carbon nanotubes is also focused on CVD-grown single-walled tubes.

Arc-discharge grown carbon nanotubes differ from the CVD-grown ones also in terms of contamination. Raw CVD material contains not only native carbonaceous debris, but also metallic catalyst particles that are prerequisite for the method of synthesis [52]. These metallic particles are covered in a layer of carbon during the

synthesis process, and act as seeds for the CNT growth. The arc-discharge method does not require the use of metal catalysts in the production of MWNTs, and this form of contamination is therefore absent in such materials. However, carbonaceous debris, consisting of e.g. fullerenes, amorphous carbon, graphite and miscellaneous carbon particles does still form in large quantities, and their elimination remains a challenge [52].

The carbonaceous debris tends to transfer onto the final sample surfaces along with the nanotubes in any deposition method (see Fig. 1.4). For the end-user, existing methods to improve the quality of the depositions made from commercial CNT powders are largely limited to improving the quality of the solutions. For this purpose, a variety of methods can be utilized that are either chemical, physical, or step-by-step combination of both. This review is primarily based on a previous presentation by Hou *et al.* (2008, [52]) which provides a good primer on the different techniques.

Chemical purification methods are generally based on selective oxidation of the impurities in gas or liquid phase, which allows their subsequent dissolution with acids. This is effective in the removal of many kinds of debris, however chemical methods, as a rule, always influence the structure and chemical nature of the CNTs [52]. This is very undesirable if the intrinsic properties of the CNTs are to be retained for the purposes of, e.g., electrical applications. For this reason, in the following I will focus on the physical methods of purification that are, in principle, gentler.

Physical methods for purification of CNT solutions rely on the contrasting morphological properties of CNTs and impurities, such as their size, weight and shape (aspect ratio). These methods include e.g. filtration, centrifugation, chromatography, electrophoresis and thermal annealing. Of these methods, the first two are most frequently applied. What is however common for all these methods is that they all require good dispersibility of the CNTs in the solution of choice. In aqueous solutions, this requires the use of surfactant additives to enhance the dispersibility of the CNTs, which may also be a risk for device applications should it not be possible to rinse them away later on.

Filtration is widely used as a purification method for bulk-quantity CNT solutions. Due to their high aspect ratio, CNTs have generally trouble to pass through filters. Typically, the objective is then to allow contaminant particles pass through while CNTs are caught, and subsequently harvested. Only particles smaller than the filter hole size can thus be efficiently separated this way. In practice, a major problem arises due to the tendency of the CNTs and the larger contaminants to block the filter, which greatly limits the throughput of the process. Thus, stability of the CNT suspensions is essential for filtration techniques to be useful.

Some variations of the standard process include sonication-assisted filtration, or microfiltration under over-pressurized conditions. These methods promise good purity of the final product with better yield, however they are experimental in nature and require specialized equipment.

Centrifugation works by the contrasting weight between different particles,

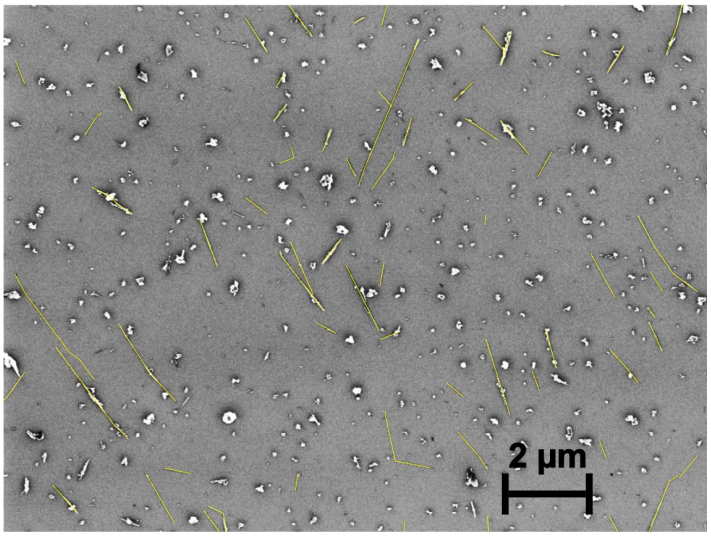


**FIGURE 1.4** Scanning electron micrograph of a typical native arc-discharge deposition spin-coated on a silicon substrate. Among the tubular CNTs, irregular debris densely populated the deposition. The CNTs were manually emphasized for clarity.

which settle at different rates in suspension in response to simulated centrifugal gravity. Centrifugation of CNT suspensions has been studied in detail not only as a laboratory-scale purification process, but also because separation by diameter of the tube has also been demonstrated [6]. In the context of CNT purification, effective separation requires modification of their surface charge state by an acid treatment that results in contrasting particulate stability of the CNTs, amorphous carbon and carbon nanoparticles in the solution. This naturally introduces functional groups onto the tubes that affects their properties.

It can thus be concluded that both of the most common physical CNT purification methods also rely upon chemical modification of the carbon nanotubes. Both filtration and centrifugation also suffer from other practical difficulties such as limited efficacy, throughput and yield. Other approaches either face similar issues (e.g. solubilization with functional groups), or are only applicable to removing the metallic catalyst particles associated with the growth of single-walled carbon nanotubes (high temperature annealing or magnetophoretic purification) that are not our prime concern. It is also worthwhile to note that majority of the works dealing with these techniques have been done with only single-walled carbon nanotubes in mind.

It follows that a simple physical purification technique that preserves all intrinsic properties of the CNTs and requires no specialized equipment is sought-after, particularly for electrical applications of arc-discharge grown multiwalled carbon nanotubes. The method described in our paper satisfies these requirements while still being very simple to apply *in-situ* for individual CNT samples.

# Chapter 2

# Structure & properties of carbon nanotubes

This chapter of the thesis deals with the properties of CNTs, starting from their atomic structure as tubular form of graphene. Given that purification of carbon nanotube depositions for the purposes of, e.g., CNT-based electronics is the main motivation of this work, the electrical properties are then discussed, placing emphasis on electrical transport in a practical CNT-based, two-probe device. Optical properties of CNTs will then be briefly introduced, focusing on the concepts relevant to our Raman characterization efforts. When applicable, a point will be made about how multi-walled carbon nanotube differ from single-walled ones in terms of these key properties.

## 2.1 Structure of CNTs

Carbon nanotubes consist of wrapped up sheets of graphene, i.e. a single-layer graphite. To that end, they owe much of their properties to the remarkable features of graphite that are modified as a result of periodic boundary conditions and wall curvature that the tubular conformation imposes. The following discussion is largely based on the description given in [102].

The two-dimensional crystal lattice of graphene, generally referred as honeycomb lattice, consists of hexagons defined by six carbon atoms where each atom is covalently bonded to three nearest neighbors. This is a result of $\mathrm{sp}^2$ hybridization[1], where the 2s orbital hybridizes with two of the 2p orbitals ($2\mathrm{p}_x$, $2\mathrm{p}_y$, $2\mathrm{p}_z$) to give rise to three hybrid $\mathrm{sp}^2$ orbitals. These strongly directional hybrid orbitals are all in plane, and form strong covalent bonds called $\sigma$ bonds when they overlap with similar orbitals of neighboring carbon atoms. This results in the planar carbon network of graphene, Fig. 2.1a.

[1]The ground-state electron configuration of carbon is naturally $1s^2 2s^2 2p^2$, but the energy of the excited state $1s^2 2s^1 2p^3$ is sufficiently small to allow the hybridization in crystalline phase.

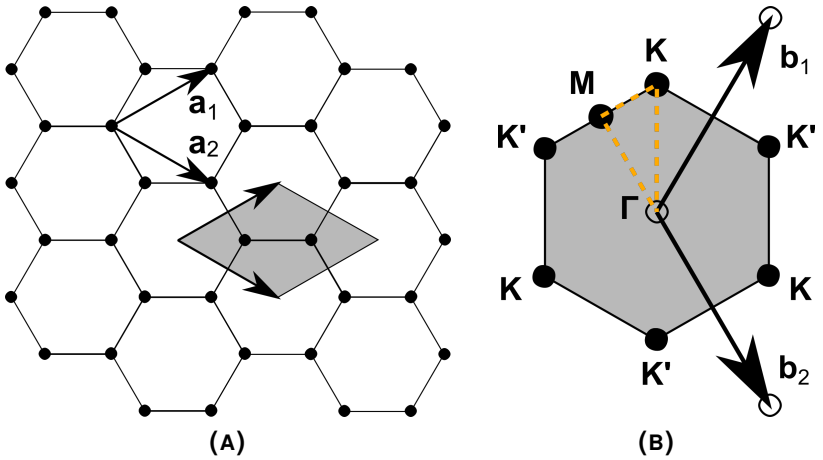


**FIGURE 2.1** (a) The honeycomb lattice of graphene, showing the lattice vectors $\mathbf{a}_1$, $\mathbf{a}_2$ and an highlighted unit cell. (b) The reciprocal lattice vectors $\mathbf{b}_1$, $\mathbf{b}_2$ and the the first Brillouin zone, also showing the high-symmetry points in the reciprocal space. The high-symmetry path $K \to \Gamma \to M \to K$ is highlighted in orange.

The final 2p orbital that was not part of the hybridization process points out of the graphene plane. These orbitals couple weakly among those of the other carbon atoms, giving rise the $\pi$ bands that are delocalized across the graphene surface. The delocalized $\pi$ electrons are responsible of the conductive properties of graphite, while the $\sigma$ electrons are strongly localized to the covalent bonds and thus do not contribute to electric transport.

The honeycomb lattice exhibits hexagonal symmetry, and as such the real-space unit vectors can be expressed in cartesian basis as

$$\mathbf{a}_1 = \left(\frac{\sqrt{3}}{2}\mathrm{a}, \frac{\mathrm{a}}{2}\right); \quad \mathbf{a}_2 = \left(\frac{\sqrt{3}}{2}\mathrm{a}, -\frac{\mathrm{a}}{2}\right), \tag{2.1}$$

where $\mathrm{a}$ is the lattice constant of graphene that relates to the carbon-carbon bond length ($1.42\,\text{Å}$) as follows: $\mathrm{a} = |\mathbf{a}_1| = |\mathbf{a}_2| = 1.42\,\text{Å} \times\sqrt{3} \approx 2.46\,\text{Å}$. The unit vectors $\mathbf{a}_1$ and $\mathbf{a}_2$ define the unit cell, which is thus rhombus-shaped. Given this definition, it can be seen that the honeycomb lattice is not a so-called bravais lattice[2], i.e. it cannot be properly formed by a set of discrete translations of the primitive vectors defining the positions of the nearest neighbor carbon atoms relative to a given central atom.

In the reciprocal space, the honeycomb lattice retains its hexagonal symmetry, and the unit vectors become

$$\mathbf{b}_1 = \left(\frac{2\pi}{\sqrt{3}\mathrm{a}}, \frac{2\pi}{\mathrm{a}}\right); \quad \mathbf{b}_2 = \left(\frac{2\pi}{\sqrt{3}\mathrm{a}}, -\frac{2\pi}{\mathrm{a}}\right), \tag{2.2}$$

[2]Unlike the hexagonal 2D lattice, which has an extra atom at the centre of the hexagon.

with the lattice constant of the reciprocal space $4\pi/\sqrt{3}a$. Contrary to the real-space picture where the unit cell does not coincide with the shape of the hexagon, in reciprocal space the first brillouin zone can be selected as such, and three kinds of high-symmetry points can be designated within: $\Gamma$ (the center), $K$ (the corner) and $M$ (the edge). The $K$-points further fall into two categories, $K$ and $K'$, that alternate along the perimeter. The energy dispersion relations (i.e. the band structure) of graphene are typically plotted along the intersecting path $K \to \Gamma \to M \to K$ when represented in two dimensions.

Carbon nanotubes are merely sheets of graphene that have been wrapped up into tubular shape in a seamless manner, and terminated with hemispherical caps. Ignoring the ends, the chiral vector $\mathbf{C}_h$ fully defines the structure of a single-walled nanotube:

$$\mathbf{C}_h = n\mathbf{a}_1 + m\mathbf{a}_2\,, \tag{2.3}$$

where $n$ and $m$ are positive integers ($m \leq n$) referred as chiral indices. Based on the chiral indices, two special cases of carbon nanotubes can be identified. These are the zigzag (n, 0) and the armchair (n, n) tubes, referred as such due to the distinctive shape of their cross-sections cut along the edges of the hexagons (Fig. 2.2). They are also commonly termed achiral tubes. All tubes that are neither zigzag nor armchair are then chiral; the hexagons of their graphene sheet curl in a spiral manner along the length of the tube.

In a single-walled carbon nanotube consisting of a wrapped-up graphene sheet, $\mathbf{C}_h$ twines around the circumference of the tube. As such, it gives its diameter

$$d = \frac{|\mathbf{C}_h|}{\pi} = \frac{a}{\pi}\sqrt{n^2 + nm + m^2} \tag{2.4}$$

given the non-orthogonal basis defined by $\mathbf{a}_1$ and $\mathbf{a}_2$, and carbon-carbon bond length $a \approx 1.44\,\text{Å}$ that is slightly larger for CNTs than for the graphite.

From the chiral vector, we can define two additional parameters of importance: the chiral angle $\theta$ and the translational vector $\mathbf{T}$. The angle $\theta$ is the angle between the vectors $\mathbf{C}_h$ and $\mathbf{a}_1$, and lies within the range from $0°$ to $30°$ due to the hexagonal symmetry of the lattice. It quantifies the extent of tilt of the hexagons with respect to the longitudinal axis of the tube, specifying spiral symmetry. It can be related to the vectors via the definition of the inner product:

$$\cos\theta = \frac{\mathbf{C}_h \cdot \mathbf{a}_1}{|\mathbf{C}_h||\mathbf{a}_1|} = \frac{2n + m}{2\sqrt{n^2 + nm + m^2}} \tag{2.5}$$

The vector $\mathbf{T}$ is defined as the unit vector of the carbon nanotube. It is perpendicular to the chiral vector $\mathbf{C}_h$, and as such runs along the axis of the tube, specifying a point in the honeycomb lattice that belongs to the unit cell of carbon nanotube like $\mathbf{C}_h$:

$$\mathbf{T} = t_1\mathbf{a}_1 + t_2\mathbf{a}_2\,. \tag{2.6}$$

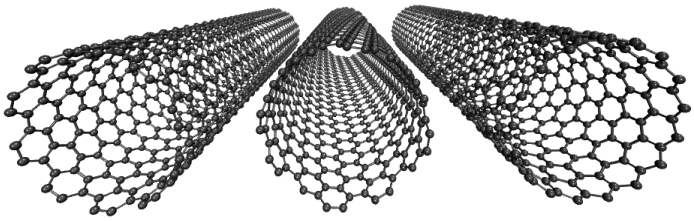

**FIGURE 2.2** Axial view of carbon nanotubes of different chiralities: (left) armchair $(n, m) = (10, 10)$; (middle) chiral $(12, 8)$; (right) zigzag $(17, 0)$. Figure courtesy of Pekka Koskinen, used with permission.

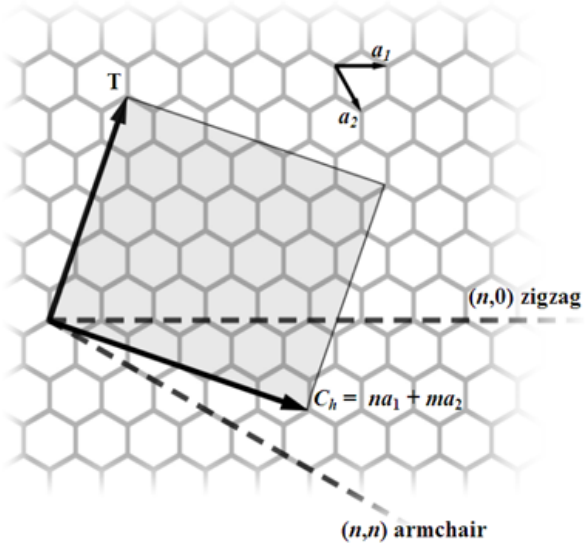


**FIGURE 2.3** Illustration of the structural parameters of a CNT superimposed onto a graphene sheet: the chiral vector $\mathbf{C}_h$ shows one possible wrapping of the sheet to make up a tube. In this particular case, chiral wrapping $(n, m) = (4, 2)$ is shown, with $\mathbf{C}_h$ that lies in between the extreme (armchair and zigzag) cases. The translational vector $\mathbf{T}$, i.e the unit vector of the CNT, lies perpendicular to $\mathbf{C}_h$, along the tube axis. Together, $\mathbf{C}_h$ and $\mathbf{T}$ define the unit cell of the tube. The chiral angle $\theta$ (not shown) is defined as the angle between $\mathbf{C}_h$ and the graphene lattice vector $\mathbf{a}_1$.

Using the condition $\mathbf{C}_h \cdot \mathbf{T} = 0$, we can find the values of the integers $t_1$ and $t_2$ in terms of $n$ and $m$:

$$t_1 = \frac{2m+n}{d_\mathrm{R}}, \quad t_2 = -\frac{2n+m}{d_R}\,, \tag{2.7}$$

where $d_\mathrm{R}$ is the greatest common divisor (gcd) of integers $(2n+m)$ and $(2m+n)$. The length of the translational vector can be expressed with the help of the tube diameter $d$:

$$T = |\mathbf{T}| = \frac{\sqrt{3}\pi}{d_R} d\,. \tag{2.8}$$

We can thus see that $T$ varies greatly depending on $d_\mathrm{R}$, which is in turn can be related to the gcd of the chiral indices $n$ and $m$.

As mentioned, the unit vectors $\mathbf{a}_1$ and $\mathbf{a}_2$ define the rhombus-shaped unit cell of the graphene, and its area $|\mathbf{a}_1 \times \mathbf{a}_2|$ equals that of the hexagon. The unit cell of carbon nanotube, defined by vectors $\mathbf{C}_h$ and $\mathbf{T}$, is much larger. The number of hexagons that the CNT unit cell encompasses, $N$, is then, simply,

$$N = \frac{|\mathbf{C}_h \times \mathbf{T}|}{|\mathbf{a}_1 \times \mathbf{a}_2|} = \frac{2(m^2+nm+n^2)}{d_\mathrm{R}} = \frac{2L^2}{a^2 d_R}\,. \tag{2.9}$$

Given that each graphene unit cell contains two carbon atoms, each CNT unit cell thus contains $2N$ of them. We note that $N$ also is strongly dependent on $d_\mathrm{R}$: for an armchair tube $(n,m) = (5,5)$, $d_\mathrm{R} = 15$ resulting in $N = 10$. But for for a less-regular chiral case, say $(n,m) = (6,5)$, $d_\mathrm{R} = 1$ and $N = 182$. The size of a CNT unit cell therefore varies greatly based on the chiral indices $(n,m)$.

## 2.2 Electrical properties

The energy dispersion relation for $\pi$ electrons in graphene can be calculated via the tight-binding model. An approximate solution reads

$$E(k_x, k_y) = \pm\gamma_0 \left[1 + 4\cos\left(\frac{\sqrt{3}k_x a}{2}\right)\cos\left(\frac{k_y a}{2}\right) + 4\cos^2\left(\frac{k_y a}{2}\right)\right]^{1/2}, \tag{2.10}$$

where $\gamma_0 \approx 2.9\,\mathrm{eV}$ is the so-called transfer integral for the $\pi$ orbitals. The signs of the function correspond to bonding, $\pi$, and anti-bonding, $\pi^*$, bands, that meet at the $K$ and $K'$ points of the first Brillouin zone at $E = 0$. In addition, it can be shown that $E(k_x, k_y)$ is linear in the vicinity of these points. No bandgap exists, but there is also no partially filled conduction band like in metals since the bands do not cross. Therefore, graphene is a zero-bandgap semiconductor, or a semimetal, where infinitely small thermal vibrations are sufficient to elevate charge carries from the valence band ($\pi$) to the conduction band ($\pi^*$) at the $K$ and $K'$ points (Fig. 2.4a).

Rolling up the graphene sheet into a tubule imposes periodic boundary con-

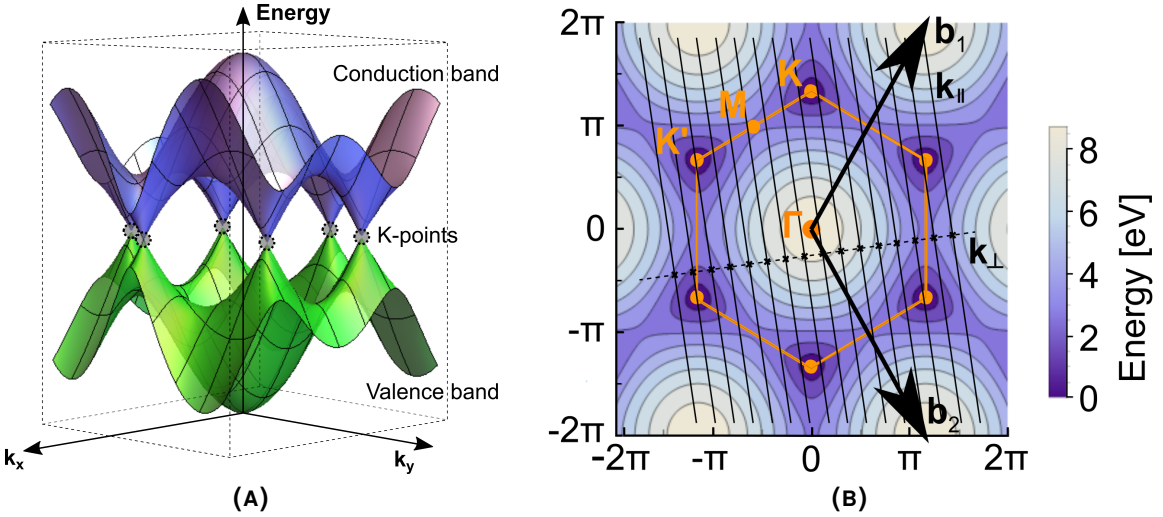


**FIGURE 2.4** (a) The $\pi$ (valence) and $\pi^*$ (conduction) bands of graphene presented in three dimensions, with the crossover K-points highlighted. (b) The first Brillouin zone of graphene superimposed over a contour plot of the graphene dispersion relation ($\pi^*$ branch). The allowed $k$-states of a SWNT are also shown as a set of parallel lines. The band structure for the carbon nanotube is made up of a set of one-dimensional cross-section of the graphene band structure along these $k$-lines.

ditions along the circumference of the tube. This affects the dispersion relation of graphene in the transverse direction along $\mathbf{C}_h$, while in the axial direction $\mathbf{T}$ it remains unhindered. The periodic boundary conditions can be described as

$$\mathbf{k} \cdot \mathbf{C}_h = 2\pi q \,, \tag{2.11}$$

where $q$ is an integer. The axial component of the wave vector $k$, $k_\parallel$ is continuous, but the component along the circumference $k_\perp$ is restricted. Two unit vectors, $\mathbf{K}_1$ and $\mathbf{K}_2$, can be defined in the reciprocal space for a single-walled carbon nanotube, but as a consequence of the periodic boundary conditions, only the vector $\mathbf{K}_2$ along the tube axis is a genuine reciprocal lattice vector. The circumferential $\mathbf{K}_1$ is instead restricted to series of discrete values of the wavevector $k_\perp$ in accordance with eq. (2.11).

As such, the first Brillouin zone of a CNT is a one-dimensional line segment parallel to $\mathbf{T}$, which can however be translocated along $\mathbf{C}_h$ by periodic intervals given by $k_\perp$. This gives rise a set of discrete, allowed wavevectors $k$ that make up a set of parallel $k$-lines depicted in Fig. 2.4b. The energy bands of a carbon nanotube consist of cross-sections of the graphene dispersion relation along these lines [102]. This is the so-called zone-folding approximation, valid for tubes of larger diameter. For very thin tubes, curvature effects give rise additional perturbations.

Since the $\pi$ and $\pi^*$ bands of graphene only meet at the $K$ and $K'$ points of the Brillouin zone, the electronic properties of a single-walled carbon nanotubes fully depend on whether any of the $k$-lines intersect one of them (Fig. 2.4b): if there is at

least one crossing, the CNT has a corresponding valence and a conduction bands that intersect, and the carbon nanotube exhibits metallic conductance (Fig. 2.5a). Conversely, if no $k$-line cross such point, there are no intersecting bands, and an energy gap must exists at the Fermi level. This gap is sufficiently small for the tube to behave as a semiconductor (Fig. 2.5b).

In practice, we do not need to consider the spatial location of the $k$-lines within the Brillouin zone of graphite in order to figure out whether a CNT is semiconducting or metallic. Equation (2.11) shows that the periodicity of the transverse wave vector $k_\perp$ depends on the chiral vector $\mathbf{C}_h$ that is, in turn, fully defined by the chiral indices $(n, m)$ (eq. (2.3)). As a result, a simple rule can be established: a single-walled carbon nanotube with chiral indices $(n, m)$ is metallic only if $n - m = 3l$, where $l$ is a positive integer; otherwise, the tube is semiconducting.

Based on this rule, we can estimate that in a random mixture of all chiralities, approximately $1/3$ of all tubes are metallic and the rest are semiconducting. Armchair tubes $(n, n)$ are always metallic. Zigzag and chiral tubes that satisfy the metallic condition are, in fact, "semi-metallic", i.e. semiconductors with a small bandgap ($E_\mathrm{g} \sim k_B T$ at room temperature) due to curvature effects. Tubes with $n - m = 3l \pm 1$ are on the other hand always semiconducting.

The magnitude of the energy gap, $E_\mathrm{g}$, can furthermore be directly related to the diameter of a semiconducting tube:

$$E_\mathrm{g} = \frac{2a\lambda_0}{d} \approx \frac{0.8\,\mathrm{eV}}{d\,(\mathrm{nm})}, \tag{2.12}$$

i.e. the band gap of a semiconducting tube is approximately inversely proportional to its diameter.

Another way to understand the conductive properties of CNTs is through their density of states, $D(E)$. It is defined as the number of states locally available per unit energy at energy $E$:

$$\mathrm{D}(E) = \frac{d\mathrm{N}(E)}{dE} \tag{2.13}$$

For a metallic CNT, eq. (2.13) has a finite value in the vicinity of the Fermi energy $E_\mathrm{F}$, and there is no band gap. For a semiconducting tube, there are no allowed states at $E_\mathrm{F}$ ($\mathrm{D}(E) = {}^{dN(E)}/_{dE} = 0$), i.e. the valence $E_\mathrm{V}$ and conduction $E_\mathrm{C}$ bands are separate, and thus an energy gap opens up with a magnitude $E_\mathrm{g} = E_\mathrm{C} - E_\mathrm{V}$.

In general, the plot of $\mathrm{D}(E)$ for a CNT exhibits characteristic features of a one-dimensional system. For such, $\mathrm{D}(E) \sim E^{1/2}$, so the density of states diverges at any $E$ corresponding to an edge of a one-dimensional band. This results into spike-like features in plot of $\mathrm{D}(E)$ (see Fig. 2.11) called Van Hove singularities that are present in both metallic and semiconducting CNTs. They are of importance in understanding the optical processes, e.g. Raman spectroscopy, in carbon nanotubes.

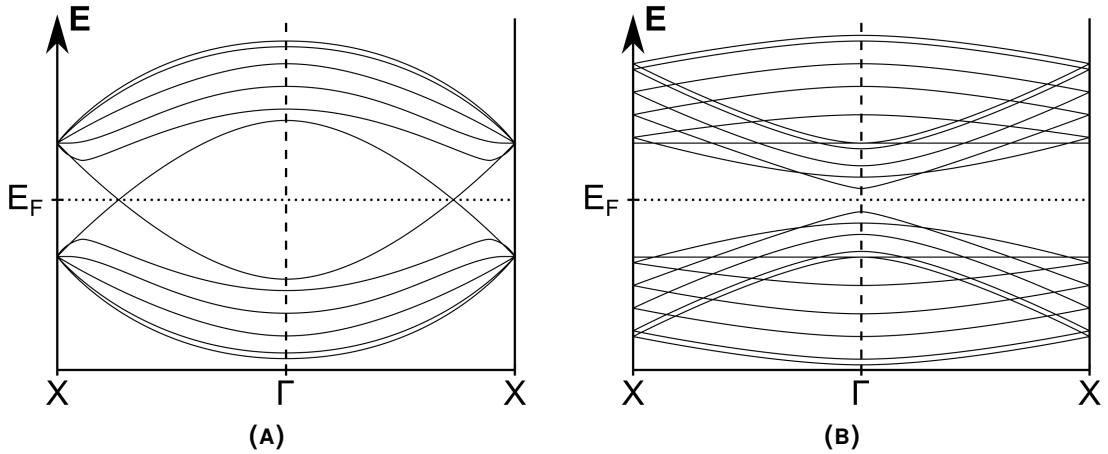


**FIGURE 2.5** Illustrative energy band schematics for (a) metallic and (b) semiconducting carbon nanotube, sketched after [19]. The exact band structure depends on the chiral indeces $(n, m)$ of the tube.

### 2.2.1 Electrical transport in a practical CNT-based device

In electronic transport measurements, carbon nanotubes need to be connected to metal source and drain electrodes. A voltage applied across these contacts gives rise to a current through the carbon nanotube. In a typical arrangement, a third electrode is utilized to provide an electric field that couples to the energy bands of nanotube, lifting and lowering them not unlike the gate electrode in a semiconductor-based field-effect transistor (MOSFET). Such devices are generally referred as CNT-FETs, with the third electrode often implemented via the bulk silicon substrate as a backgate, separated from the tube by a dielectric medium such as a $SiO_2$ layer grown on top of plain Si (Fig. 2.6). The carbon nanotube can then be ideally viewed as a one-dimensional conductive channel. A feature that separates CNT-FETs from traditional semiconductor transistors is that CNTs are intrinsically ambipolar, i.e. both electrons and holes may contribute to the transport in a given device.

Let us consider a practical CNT-FET device as described above, fabricated from a semiconducting single-walled carbon nanotube. The presence of metallic contacts has major ramifications for the transfer of charge carriers through the system. The nanotube-metal contact is subject to a potential energy barrier called the Schottky barrier (Fig. 2.7) that the charge carriers must cross in order to propagate through the system. It rises due to mismatch between the energy band structure of the CNT (defined by the dispersion relation) and the metal (the work function). The barriers for n-type and p-type charge carries (electrons and holes, respectively) are, in general, not equal; this results in either electrons or holes dominating the conductive behavior of semiconducting CNTs, inducing asymmetric behavior particularly in thin tubes. For CNTs of larger diameter, the impact of the Schottky barriers on transport is overall weakened [36].

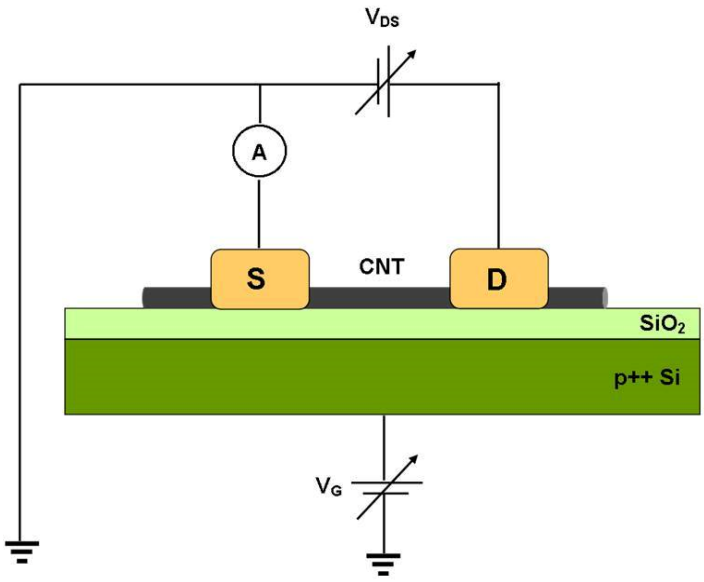


**FIGURE 2.6** Schematic of a carbon nanotube -based field effect transistor (CNT-FET) device, showing the source and drain electrodes and configuration of bias ($V_{\mathrm{G}}$) and gate voltage ($V_{\mathrm{DS}}$) sources. Figure courtesy of Peerapong Youtprayoonsak, used with permission.

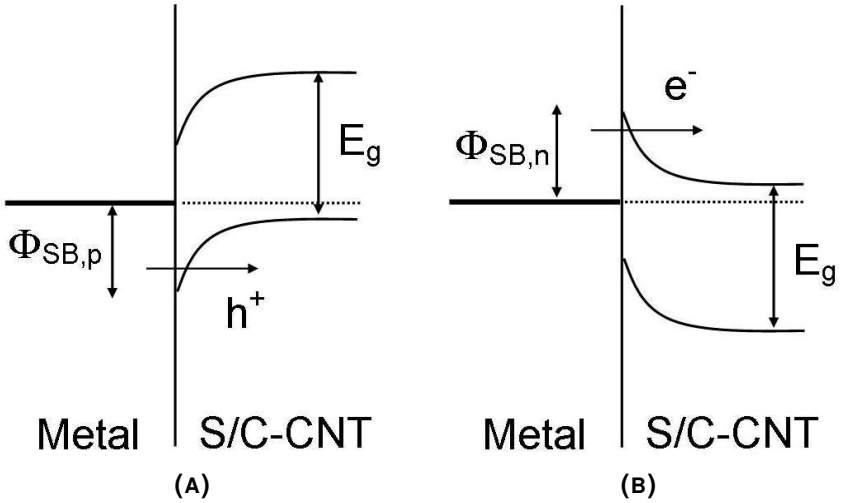


**FIGURE 2.7** Formation of (a) a p-type Schottky barrier (favoring in hole conduction) between a semiconducting CNT and a high work-function metal, and (b) a n-type Schottky barrier (electron conduction) for a low work-function metal. Figures courtesy of Peerapong Youtprayoonsak, used with permission (modified by the author).

Independent of the Schottky barrier, the electric field applied by the gate electrode affects the transport by lifting or lowering the CNT energy levels with respect to the Fermi level $\mathrm{E_F}$ (Fig. 2.8). Initially, the Fermi level lies in the middle of the conduction band $\mathrm{E_C}$ and the valence band $\mathrm{E_V}$, and the device does not conduct. Applying a positive gate voltage ($V_\mathrm{G} > 0$) brings the Fermi level closer to the conduction band, which enhances the injection of electrons from the metal contacts to the conduction band. However, the injection of holes (to the valence band) is in the meantime inhibited. A negative gate voltage ($V_\mathrm{G} < 0$) has the opposite effect: hole conduction is enhanced while electron conduction is inhibited.

In an intrinsic CNT-FET for a fixed drain-source voltage $V_\mathrm{DS}$, the plot of the source-drain current $I_\mathrm{DS}$ as a function of the gate voltage $V_\mathrm{G}$ is, then, a symmetrically raising curve centered around a minimum at $V_\mathrm{G} = 0$. The central valley is referred as the OFF-state of the device, while at large values of $|V_\mathrm{G}|$ the current $I_\mathrm{DS}$ saturates (the ON-state). In a practical experiment, the transport tends to be dominated by either electrons or holes, resulting in non-symmetric, unipolar gate response where one of the ON-states is suppressed[3]. For example, for noble metals with high work function such as gold (Au) or palladium (Pd) used in the contacts, a p-type Schottky barrier (Fig. 2.7a) rises, leading to predominant hole conduction with stronger ON-state at $V_\mathrm{G} < 0$. Furthermore, capacitive effects at the gate dielectric often result into the OFF-state shifting away from $V_\mathrm{G} = 0$ when the gate voltage is cycled (Fig. 2.9a).

The FET-type behavior described here is highly temperature-dependent. In room temperature, thermal vibrations tend to obscure the presence of the bandgap, considerably weakening the OFF-state in semiconducting tubes. Lowering the temperature to cryogenic levels then results into opening of the OFF-state (Fig. 2.9b). CNTs that are genuinely metallic in nature have no bandgap, and as such show no gate response at any temperature.

### 2.2.2 Dissipative mechanisms

The resistance one measures for a CNT-FET device is a sum of that of the CNT and the contact resistance at the CNT-metal interfaces. The contact resistance arises primarily due to the Schottky barrier, and as such it can be minimized via proper choice of the metal, i.e. one with appropriate work function and good wetting properties to CNTs, such as palladium [63]. The intrinsic resistance of the CNT depends on the charge carrier density as regulated by the gate voltage $V_\mathrm{g}$, and is also subject to the various dissipative mechanisms that appear in the channel of the nanotube. Generally, these transport mechanisms are divided into ballistic transport, diffusive transport and strong localization. Which of these are prevalent depends on the length of the

[3]It should be noted that unipolar response is, in fact, often desirable from the application viewpoint; in a practical CNT-FET, ambipolar nature results to high OFF-state leakage currents at higher bias voltages. In applications, this is a nuisance that must be suppressed by e.g. engineering the Schottky barriers [36].

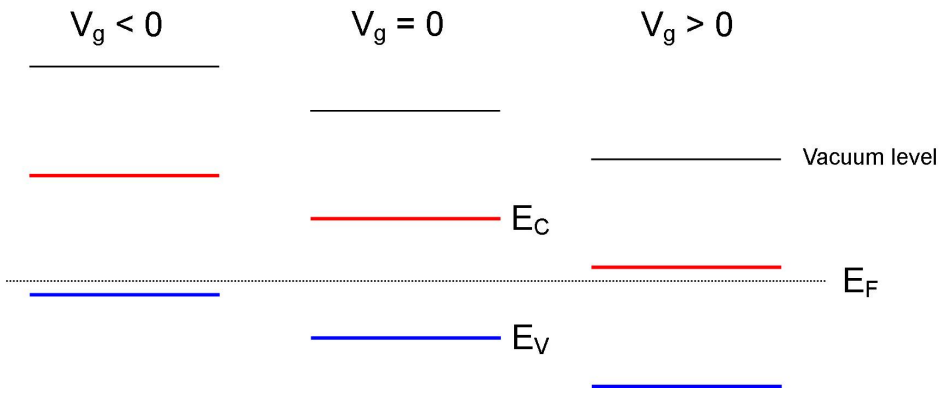


**FIGURE 2.8** Schematic of the effect of electric field to the band structure of a semiconducting CNT. Figures courtesy of Peerapong Youtprayoonsak, used with permission.

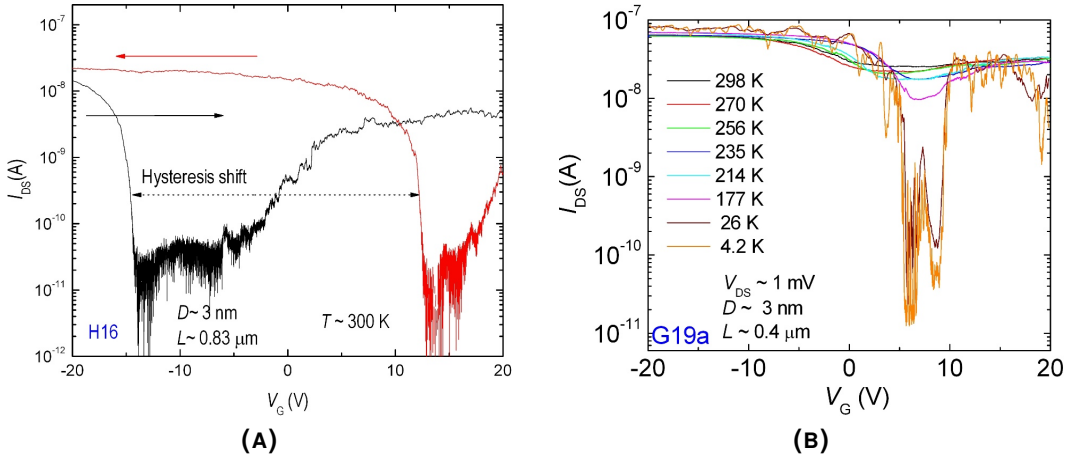


**FIGURE 2.9** (a) Two room-temperature gate curves recorded in opposite directions of the $V_{\mathrm{g}}$ sweep that illustrate the hysteresis due to capacitive effects. $V_{\mathrm{DS}}, D \,\&\, L$ designate the drain-source voltage, tube diameter and device length, respectively. (b) A set of CNT-FET transistor characteristics i.e. gate graphs ($V_{\mathrm{g}}$, $I_{\mathrm{ds}}$) recorded at different temperatures at a fixed drain-source bias voltage. The gap opening at low temperatures is clearly demonstrated. NOTE: these particular measurements reflect multi-walled carbon nanotubes. Figure courtesy of Davie Mtsuko, used with permission.

nanotube channel $L$, i.e. the length of the CNT segment in between the electrodes, with respect to the characteristic length scales of various scattering events in the nanotube: mean free path $L_{\mathrm{m}}$, localization length $L_0$ and phase coherence length $L_\phi$.

### Ballistic transport

Ballistic conduction takes place when the channel length is shorter than the characteristic lengths associated with the scattering events: $L < L_{\mathrm{m}}, L_0, L_\phi$. In this regime, no dissipative mechanisms exist within the channel, and there is no drop of voltage along the length of the CNT. The entire system is however still not free of dissipation,

because quantum resistances exist at the metal-CNT interfaces due to mismatch of discrete modes of the 1D CNT channel and the continuous states at the macroscopic contacts. This mismatch results into finite quantum conductance at the contact, which can be computed using Landauer-Büttiker formalism for a generic 1D conductor with $M$ transmission modes and average transmission probability $T$ [102]:

$$G_{\mathrm{q}} = \frac{2\mathrm{e}^2}{h} MT. \tag{2.14}$$

Thus, for a single-mode conductor ($M = 1$) with perfect contacts ($T = 1$), there exists a quantum resistance $R_{\mathrm{q}} = {}^{h}/_{2e^2} \approx 12.9\,\mathrm{k}\Omega$ that is always present in a practical, connected system. For SWNTs that behave ballistically, there are two modes ($M = 2$, for two $\pi$ subbands) available for transport, and as such $R_{\mathrm{q}} \approx 6.5\,\mathrm{k}\Omega$ is the theoretical minimum resistance for a SWNT-based device [7].

### Diffusive transport

In this regime, $L_\phi < L, L_0$. This results into inelastic scattering dominating the transport in a diffusive process, and ohmic behavior where the conductance is inversely proportional to the channel length $L$. A phenomenological description of the conductance $G$ then reads

$$G \approx \frac{2e^2}{h} \cdot \frac{L_{\mathrm{ie}}}{L}\ , \tag{2.15}$$

where $L_{\mathrm{ie}}$ is the characteristic length for inelastic scattering events [19]. Temperature affects the rate of scattering events via $L_{\mathrm{ie}}$, which is in the scale of a few microns in room temperature. Diffusive transport in CNTs is primarily observed for moderately defective samples at low source-drain bias voltage $V_{\mathrm{ds}}$.

### Strong localization regime

In the regime of strong localization, $L_0 < L < L_\phi$, the transport is governed by scattering events from crystalline defects and impurities. Once the density of these defects becomes sufficiently high, the charge carrier wave functions localize strongly around the defect sites that prevent them from propagating classically. The carriers may then propagate only through the means of quantum tunneling, hopping between the localized states [19]. In this case, the conductivity of the tube has exponentially decaying dependence on the channel length $L$:

$$G \approx G_0 \exp(-{}^{L}/_{L_0})\,. \tag{2.16}$$

This model explains the transport in carbon nanotubes at modest bias voltages in case the crystal structure is heavily populated by defects.

### 2.2.3 Electrical properties of multiwalled tubes

So far, our discussion has been exclusively in terms of single-walled carbon nanotubes. Multi-walled carbon nanotube (Fig. 2.10) can be regarded as a concentric assembly of several single-walled tubes, which provides an interesting departure from the straightforward theoretical picture presented above. The first approximation to understand electrical properties of MWNTs could be to assume that these properties are primarily dictated by the outermost tube shell and its chiral properties. This is equivalent to taking them as little more than particularly thick single-walled carbon nanotubes that may also be either metallic or semiconducting, with the semiconducting band gap $E_{\mathrm{g}} \propto d^{-1}$ much like in eq. (2.12).

This seemingly crude assumption is more justifiable than one might first think. If a single-walled carbon nanotube is considered a derivative of a graphene sheet, a multi-walled tube can be associated with few-layer graphite. Electrical conductance of graphite is primarily restricted along the plane of the graphene sheets; in the transverse direction, the conductance is severely limited due weak coupling between the layers. One may then argue reasonably that the shells of multi-walled carbon nanotubes should be similarly disconnected, with few intershell interactions in the radial direction.

Nevertheless, the applicability of eq. (2.12) in MWNTs has been subject to long-term debate; even if the intershell interactions are weak, it is still not clear whether it applies for the vastly broader range of diameters (i.e. strongly varying sidewall curvature) associated with MWNTs. The quality of the tubes probably plays even more significant role for multi-walled tubes: CVD-grown MWNTs have intrinsically curved shape, which is typically associated with defectiveness. Measurements have confirmed that transport in CVD-grown tubes resembles strong localization, at least for thicker diameters [113]. Particularly for large channel length $L$, the localization effects easily obscure the intrinsic energy gap.

Arc-discharge grown multi-wall tubes on the other hand tend to be straight, with better conductive properties than those of the CVD-grown tubes [62]. This is believed to reflect higher degree of crystalline integrity, and lower concentration of defects [32]. Recent measurements with intermediate-diameter, arc-discharge grown, semiconducting MWNTs suggest that, like SWNTs, they can exhibit either semiconducting or metallic conductive properties [2, 83]. Metallic tubes can be found within a broad diameter range, but they only make up a small fraction of all tubes [83]; more commonly, tubes that do not exhibit a distinct OFF-state in room-temperature measurements see a weak gap opening at cryogenic temperatures.

The bandgaps of semiconducting tubes were found diameter-dependent at least up to $d = 10\,\mathrm{nm}$ and $L < 600\,\mathrm{nm}$ in these measurement, but the gaps were smaller than predicted by eq. (2.12) for SWNTs [83]. This discrepancy is probably due to the interlayer effects, which likely become increasingly prevalent as the diameter of the tube increases. At larger diameters ($d > 10\,\mathrm{nm}$), systematic behavior is smeared

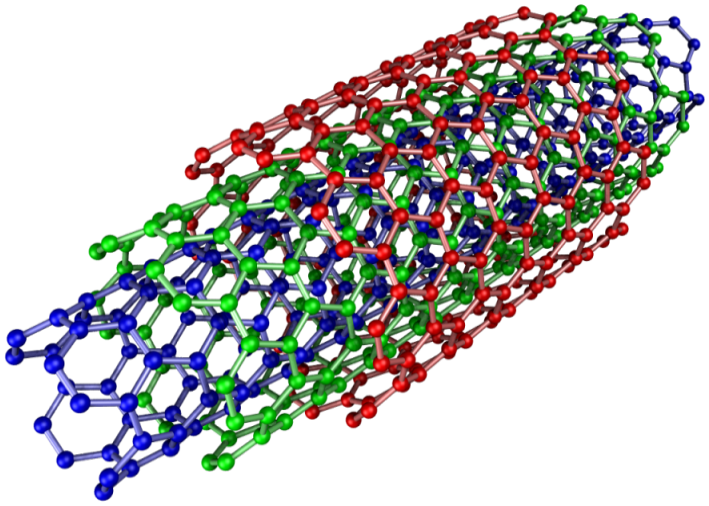

**FIGURE 2.10** Illustration of a multi-walled carbon nanotube. © Eric Wieser, Wikimedia Commons / CC-BY-SA-3.0 .

by thermal and disorder effects. The channel length $L$ was also found to influence the transport; as the length increases, quantum localization effects become more prevalent in the transport, while for $L < 600\,\mathrm{nm}$ it remains quasiballistic.

## 2.3 Optical properties: Raman spectroscopy of individual CNTs

Raman spectroscopy is one of the key experimental methods in the nanocarbon field. Traditionally, spectroscopic techniques have been used to study bulk materials, e.g. a composite of different CNTs, but contemporary Raman spectroscopy techniques allow spectra to be collected from individual carbon nanotubes. Such spectra exhibit some common features with nanocarbon materials in general, but details particular to carbon nanotubes are brought about by their intrinsic characteristics. Systematic discussion of these features would comprise the derivation of selection rules for Raman-active vibrations in a CNT via point group theory; this will be omitted here in favor of a qualitative discussion with the objective of understanding the essential features of the spectra.

As mentioned before, each CNT unit cell contains $2N$ carbon atoms, where $N$ is given by eg. (2.9). As such, there should be $6N$ phonon modes, but four of them turn out to be acoustic. Therefore, one can look forward up to $6N - 4$ optical modes that are of possible relevance in spectroscopy techniques. Previously, we saw that $N$ can vary greatly depending on the chirality of the CNT; however, for the purposes of spectroscopy, it turns out that group theory selection rules exclude the majority of these, and as a result there are only 15 or 16 Raman-active modes for any given single-walled nanotube. Furthermore, the interaction cross-section for some of

these is so tiny that only six or seven are intense enough to be relevant for practical measurements [102].

Van Hove singularities inherent to one-dimensional density of states (Fig. 2.11) play a crucial role in defining the optical properties of a carbon nanotube. If the positions of the singularities in the valence band are designated as $v_1, v_2, ...$, and those in the conduction band as $c_1, c_2, ...$, then electronic transitions ($v_1 \rightarrow c_1, v_2 \rightarrow c_2$) between these states are possible as a result of photon absorption[4]. These transitions are generally labeled as $E_{11}, E_{22}, ...,$ , where the transition $E_{11} = E_g$ in a semiconducting tube. Raman scattering is greatly enhanced if the energy of the exciting laser equals such an optical transition; this is referred as resonant Raman scattering.

All practical Raman experiments with CNTs are dependent on the fulfillment of these resonance conditions, because the Raman cross-sections of the phonon modes in individual CNTs are too small to be detected. Due to the sharpness of the Van Hove singularities, resonance condition provides a substantial enhancement of the signal for CNTs which enables their resolution. When bulk SWNT depositions are investigated, this results in the selection of species that have at least one transition that coincides with the excitation energy. For individual tubes, the laser frequency needs to be tuned based on the chiral properties of the nanotube before Raman signal can be resolved.

[4]It should be noted that crossover transitions, such as $c_1 \rightarrow v_2, v_2 \rightarrow c_1$, are, in contrast, forbidden.

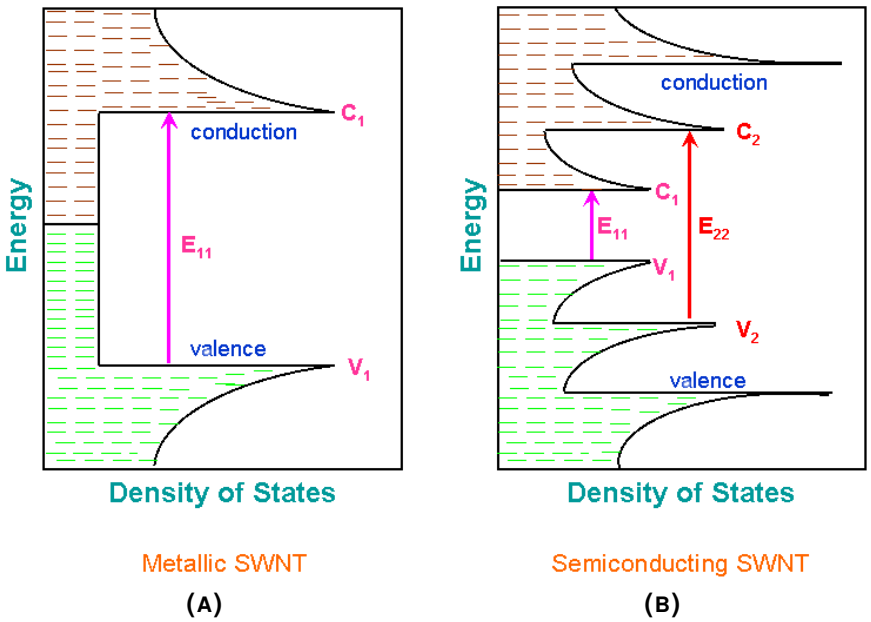


**FIGURE 2.11** Schematic density of states as a function of energy for a typical (a) metallic and (b) semiconducting carbon nanotube. Some of the possible electronic transitions $E_{ii}$ between the Van Hove singularities are indicated. In (b), the transition $E_{11}$ is simply the semiconducting band gap. © Materialscientist, Wikimedia Commons / CC-BY-SA-3.0 (modified by the author).

In case of multi-walled nanotubes, the large number of concentric shells means that the resonance condition is more likely satisfied for at least some of them, and MWNTs can thus be resolved more easily. But as a consequence, interpretation of the spectra becomes more complicated because it is generally not possible to tell which shells contribute to the Raman response. However, the energy separation of the Van Hove singularities in CNT density of states decreases as the number of energy bands increases [102], and thus they tend to become increasingly frequent for thick tubes. Consequently, the outer shells of MWNTs are more Raman-active than the inner shells for any given excitation wavelength.

### 2.3.1 Raman modes of CNTs

Generally, three main Raman modes can be identified in the spectra single-walled carbon nanotubes: the G-band, the D-band, and the radial breathing mode (Fig. 2.12).

#### G-band

The G-band ("graphitic" band) is an intrinsic feature of $\mathrm{sp}^2$ -hybridized carbon materials, and appears in $1500 - 1605\,\mathrm{cm}^{-1}$ range in CNTs [31]. It corresponds to planar vibrations in graphitic materials, and stems from a doubly-degenerate, Raman-active optical mode $E_{2g}$ of the graphene $\Gamma$ point. Roughly speaking, this results in the G-band splitting into two subbands, $G^+$ and $G^-$, in CNTs. The splitting occurs due to decoupling of the mode into longitudinal (LO) and transverse phonon modes (TO), where the former is polarized along the axis of the tube, and the latter one along its circumference.

The shape and position of these peaks are sensitive to the electrical properties of the tube. For a semiconducting tube, both subbands reflect a symmetric, Lorentzian line shape, but in a metallic tube, the width of the $G^-$ band is increased, and the peak is shifted to lower frequency. This is due to so-called Kohn anomalies [92], which only appear in metallic tubes. The shape of the G-band can therefore be used to assign CNTs as metallic or semiconducting. Strong G-band is overall interpreted as a trait of a more ordered carbon structure [31], and together with a weak D-band it indicates a high degree of crystalline integrity.

The clear splitting of the G-band seen in single-walled carbon nanotubes is generally far less evident in multi-walled tubes, and interpretation of the band becomes more difficult. In a handful of works, a degree of splitting has been observed, but rather than a clearly separated pair of peaks, a broadened feature is usually seen that can be fitted with several Lorenzians [15, 71, 86, 97, 131].

#### D-band

Similar to the G-band, the D-band is also intrinsic to all $\mathrm{sp}^2$ -hybridized carbons, and it is commonly observed in the $1300 - 1400\,\mathrm{cm}^{-1}$ wavenumber range [31]. The

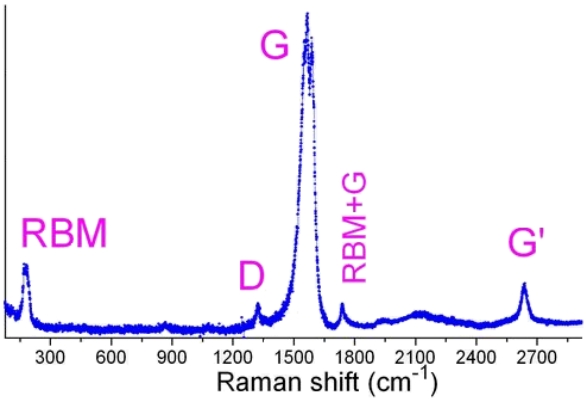


**FIGURE 2.12** Raman spectrum typical to a single-walled carbon nanotube, with the response (y-axis) in arbitrary units. Aside the main peaks (G, D & RBM), some of their overtones are also seen. © Materialscientist, Wikimedia Commons / CC-BY-SA-3.0 (modified by the author).

D-band is related to the extent of disorder in the nanocarbon material. It arises from a Raman process where phonons deeper inside the Brillouin zone, i.e. not just those that are in the vicinity of the $\Gamma$ point, become active due to a double resonance process that is increasingly likely as the number of defects increases. These defects may be impurities, crystalline defects, adsorbed molecules or finite-size effects associated with the nanotube. Contrary to the G-band, the D-band is highly dispersive, i.e. its frequency is strongly dependent to the energy of the excitation laser [31].

The weakening of the D-band in response to improved crystalline integrity of a nanotube sample has been observed in a practical experiment with high-temperature treatment and TEM imaging [16]. It follows that the fraction of the G-band intensity to that of the D-band, $G/D$, is a direct measure for the concentration of defects in carbon nanotubes. Based on the previous discussion about the defectiveness of CVD-grown CNTs in comparison with arc-discharge synthesized ones, it is then not surprising that the $G/D$ ratio may become very large in arc-discharge grown tubes [49, 53, 86].

### Radial breathing mode

Radial breathing mode (RBM) lies considerably lower in the frequency compared to the $\mathrm{sp}^2$-carbon bands, around $100 - 400\,\mathrm{cm}^{-1}$. In this phonon mode, the carbon atoms along the circumference of the tube move radially in coordinated fashion, which results into systematic fluctuation of the tube diameter. This mode is also exhibited by fullerenes [30]. There exists a dependence between the frequency of the mode, and the diameter of the CNT as of

$$\omega_{\mathrm{RBM}} = \frac{\alpha}{d} + B\,, \tag{2.17}$$

where $\alpha$ and $B$ are constants that vary significantly from study to study.

Aside from using eq. 2.17 directly, Chiral indices, and with them, the tube diameter, can also be estimated using so-called Kataura plots [67], where the energies of different optical transitions are plotted as a function of $\omega_{\mathrm{RBM}}$ for several tubes. This experimental plot ($\omega_{\mathrm{RBM}}, E_{\mathrm{exp}}$) can then be compared against a similar graph from a theoretical calculation ($d, E_{\mathrm{theo}}$).

In practical experiments, the RBM signal is easily obscured by characteristic features of the substrate unless the sample is suspended. In multi-walled carbon nanotubes, instead of an individual mode, a set of RBM-like modes has been observed, where the individual subbands are associated with the innermost tube layers. When correlated with TEM measurements of the layer diameters, these bands are observed to have shifted towards higher wave numbers with respect to the RBM frequency of a SWNT of similar diameter which highlights the role of the intershell effects in MWNTs [17, 110].

# Chapter 3

# Surface chemistry & wetting phenomena

Wetting phenomena are prominently portrayed in the background of the experimental results considered in this thesis. Particularly central to us are the wetting properties of silicon surfaces, which are generally dictated by chemical factors on smooth surfaces. These topics are briefly discussed in the starting section of this chapter.

In the following section, central concepts of the classical wetting theory will be introduced, placing emphasis on the traditional sessile droplet geometry. This is done particularly with our first paper in mind, where a similar scenario is considered; while our results can arguably be understood outside such stringent theoretical network, it is useful to understand the origin of the quantities we deal with. Furthermore, these theoretical considerations also touch the content of our subsequent works, where systematic on-chip cleaning of carbon nanotubes is achieved in a forced wetting scenario.

## 3.1 Chemistry of silicon surfaces

Like carbon, silicon is part of the IV-group elements in the periodic table, and as such they share much of their chemical properties. Silicon in its bulk crystalline form exhibits the $\mathrm{sp}^3$-hybridized diamond structure where each Si atom is covalently bonded to four other atoms with tetrahedral coordination. As a result of cutting or cleavage, a surface is formed where the number of nearest neighbor atoms is decreased, and vacant, dangling bonds exist instead. Such a structure is energetically unfavorable compared to a fully saturated bulk system, and therefore the system seeks to reduce the number of the dangling bonds. This can be either via restructuring the pure silicon surface, or by incorporation of foreign atoms or molecules onto the surface via chemisorption [44]. The surface-chemical properties of silicon-based surfaces are therefore largely defined by the desire to saturate the dangling bonds.

The structure of the silicon surface also depends on the direction of the crystalline planes. The (100)-oriented silicon is most common in applications, and will also be the subject of our interest. In this orientation, each surface atom is connected to two bulk atoms, and accordingly, two dangling bonds are left over (Fig. 3.1a). It is generally agreed that this structures reconstructs according to the so-called dimer model, where the number of dangling bond is halved by additional bonding of two surface atoms with one another as presented in Fig. 3.1b. The atomic dimer arrangement can accomplished in different ways, resulting in a variety of possible structures for the surface at large [44].

The surface of pure silicon is highly reactive due to the dangling bonds, and is therefore never observed in ambient conditions. Instead, the bonds are terminated by foreign molecules. One of the simplest ways to passivate the surface is brought about by termination with hydrogen. Trivially, one would then expect a single hydrogen atom per silicon atom (Fig. 3.2a). In practice, the bonding may be far more complicated than this, because the Si–H bonds ($\sim 366\ \frac{\mathrm{kJ}}{\mathrm{mol}}$) are stronger than the bulk Si–Si bonds ($\sim 226\ \frac{\mathrm{kJ}}{\mathrm{mol}}$), and therefore energetically favored. Hydrogen exposure thus results into a more comprehensive restructuring of the silicon surface where breakage of Si–Si may also take place. Several different structures have been suggested, and experiments show that the result depend on the experimental parameters in highly non-trivial way [44].

From a practical viewpoint, by far the most important stabilizing group on silicon is oxygen, in the form of silicon oxide i.e. silica, $SiO_2$. Silicon oxide films can be grown by a variety of methods, but thermal growth at elevated temperatures under exposure of oxygen or water is the method typically used in industrial processes to grow amorphous insulating layers on plain silicon wafers. The silica layer can be used e.g. as a dielectric, insulating the devices fabricated on the surface from the conductive bulk silicon that can then be used as a gating electrode. Aside from deliberately grown films, thermal oxidation also takes place spontaneously in ambient environment, forming thin native oxide in the order of a few angstroms [79].

It has been established that room-temperature adsorption of oxygen on silicon surfaces is predominantly via a dissociative mechanism where $O_2$ molecules divide into atomic oxygen radicals that then bond to the surface. Considering the dimer structure of (100)-oriented silicon surface, there are several possible bonding sites. Interestingly, the preferred site of the oxygen is not directly at the dangling bond pointing, but rather a bridging position in between the dimeric Si atoms (Fig. 3.2b) [44]. This structural motif (Fig. 3.3) can be found in almost all forms of bulk silica, where the spatial arrangement of these units gives rise a variety of crystalline structures (polymorphs) that can be met in different environments.

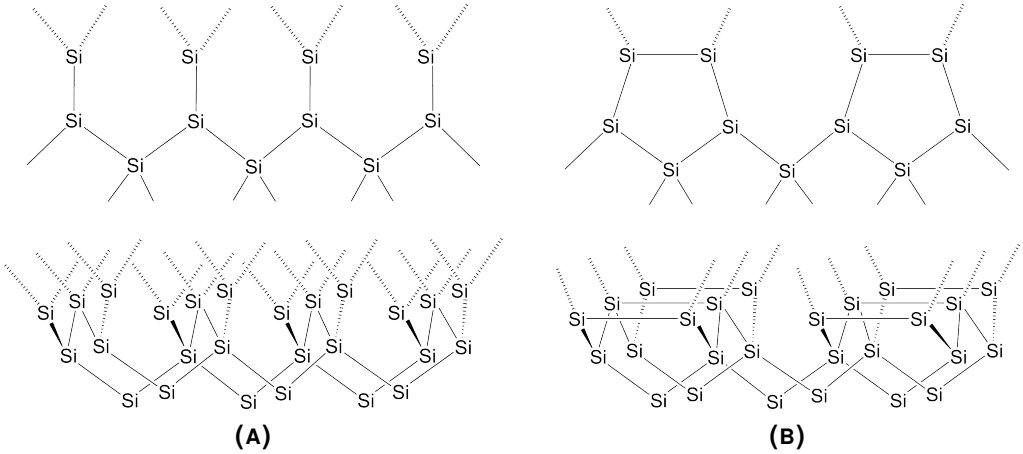


**FIGURE 3.1** Schematic structures of (a) native, crystalline silicon surface with two dangling bonds, and (b) the reconstructed dimer arrangement where only one dangling bond is left over. The upper diagrams show individual structural segments projected onto a plane, while bottom depicts a three-dimension perspective of the surface.

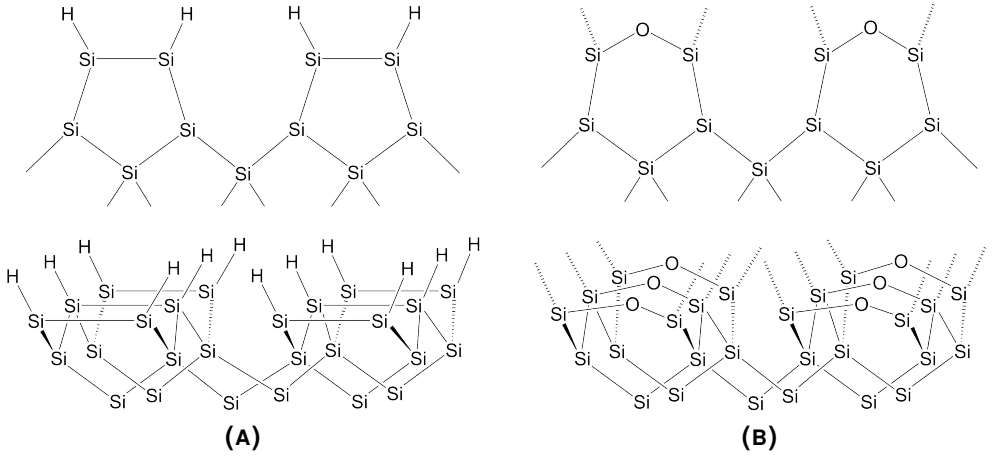


**FIGURE 3.2** Simple view of the silicon surface passivation by two common passivating groups: (a) termination of the dangling bonds by hydrogen; (b) oxygen adsorption, where the oxygen atoms bond at bridging positions between Si dimers.

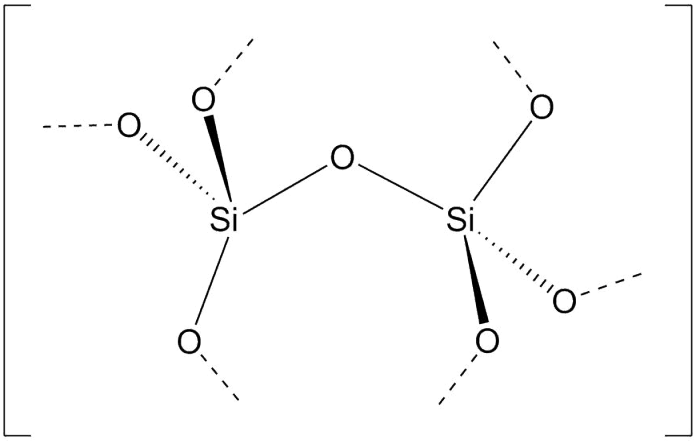


**FIGURE 3.3** The structural motif commonly found in crystalline $SiO_2$ polymorphs, where each silicon atom is neighbored by four oxygen atoms.

### 3.1.1 Wetting properties

The reactivity of molecular $H_2$ on silicon surfaces is low, and practical saturation of Si surfaces must thus take place in the presence of atomic hydrogen. The standard laboratory-scale method for this is through the use of HF solutions that both etch away the native oxide layer and terminate the plain silicon surface. In addition to hydrogen capping, some coverage of Si by fluorine may also take place. Energetically favorable compared to plain silicon surface, the hydrogen-terminated silicon behaves as a "low energy" surface in terms of wetting. As a result, it reflects a fairly hydrophobic character when exposed to water: the liquid does not spread, but forms a droplet instead; treatment of silicon wafers in concentrated HF is thus also useful as a hydrophobic treatment [13].

The drawback of this method is that the hydrophobic surface is still not entirely stable, and the hydrogen-capped structure will gradually dissociate in ambient environment. This has been attributed to re-formation of the native oxide that displaces the passivating hydrogen layer in a complicated process via consecutive chemical reaction steps. How quickly this happens probably depends on the quality of the initial passivating layer, and the environmental conditions; studies suggest that the timescale of the growth is in the order of hours [66], although it can be slowed down somewhat by storing the wafers in water [13].

For silicon oxide, the wetting properties are even more complicated. Silica is also intrinsically hydrophobic in nature, however this only applies to dehydrated $SiO_2$. In ambient environment, a typical silica surface contains some polar hydroxyl (OH) groups, enough to make the surface predominantly hydrophilic [24]. It is possible to increase the density of the OH groups on the surface by chemical methods, which should also result to more systematic surfaces. The most well-established of these include piranha solution (mixture of concentrated sulfuric acid $H_2SO_4$ with hydrogen peroxide $H_2O_2$) and RCA cleaning ($NH_3$ with $H_2O_2$, also referred as "base piranha")

treatments that are both carried out in elevated temperatures.

Given the high reactivity of these solutions, dry techniques such as UV/ozone or oxygen plasma are often preferred as substitutes at small-scale laboratory production [13,22]. All these hydroxylating treatments give rise to hydrophilic surface character where liquid spreads out on a freshly treated surface with very small contact angles, and they also work to eliminate organic contamination on the surface.

Like hydrogen-passivated, hydrophobic silicon, the hydrophilically treated Si surfaces are also not stable, and tend to adsorb contaminants when exposed to environment, such as airborne hydrocarbons and organic molecules originating from the storage boxes [22]. This can be observed as gradual increase of the water contact angle in experiments towards that of a native wafer. This aging effect has also been studied, and its timescale varies from a few hours up to several days [105]. The process can be slowed down by storing the wafers in dry inert gas [13]. Upon coming to contact with liquid water, the hydroxylated silica surface is passivated by a few-monolayer thick, ice-like coverage of hydrogen-bonded $H_2O$ [24].

Practical contact angle measurements of silicon surfaces are subject to large variations where the angles depend on surface preparation, environmental factors and experimental details such as the time delay from the surface treatment. The reported values for HF-etched Si reach up to $90^\circ$ [47,78]. For Si wafers in their native state, the experimental values range from $20^\circ$ to $40^\circ$ [90], and similar values are expected for thermally grown $Si/SiO_2$ surfaces as well given that native oxide is present on "plain" Si wafers in ambient conditions. For hydroxylated, silicon-based surfaces, contact angles well under $20^\circ$ are typical [37,47,68] for wafers freshly treated in piranha solution or oxygen plasma.

## 3.2 Capillarity and wetting phenomena in droplets

Wetting plays pivotal role in numerous fields of science, such as contact mechanics, adhesion, tribology and soil science. Some of the most important real-world applications include self-cleaning surfaces, adhesion of paints and locomotion of insects on water surfaces. In particular, the methods and goals of modern nanotechnology have brought with them new impetus for the research of wetting phenomena. The science of capillary and wetting falls close to the domain of surface and interface science, while hydrodynamical concepts also play a key background role in understanding the rich field of phenomena.

Among the most intriguing examples of the recent discoveries associated with liquid droplets deal with the famous "coffee-ring effect", i.e. ring-like stain that results of a drying colloidal liquid, characteristic to spills of coffee, wine, etc... The generally accepted explanation was given by Deegan *et. al* in 1997, who established that the pattern formation is due to the liquid evaporating faster at the edges of a droplet with a pinned contact line, giving rise to an evaporative flow within that

results to gathering of dispersed material close to the contact line [25].

Another key research subject as of late has been the so-called precursor layer, a nanometer-thick molecular film that extends ahead of the contact line of a non-volatile liquid droplet. First detected as early as 1919 by Hardy [45], it conceptually resolves a dilemma associated with the spreading of completely wetting droplets in accordance to the well-known Tanner's law: the insensitivity of the dynamics to the spreading coefficient $S$ of the system [112].

Wetting is generally driven by persistence towards minimal system surface energy, which one can understand as application of the most general physical principles to interfaces, i.e. discontinuities in materials. This is well-illustrated in the following treatment of droplets. Sessile droplet is the fundamental test geometry of capillary science, and remains an active field of study up to this date. The discussion below follows de Gennes, Brochard-Wyart and Quere (2004) [28].

### 3.2.1 Static contact angles

When a volume of liquid is deposited on a surface, it either forms a distinctly wet, localized spot, or spreads out fully, forming an uniform film. The latter possibility is not experienced in everyday life, given that it requires a surface that is not only wetting for the liquid in question, but also completely clean and uniform. The non-wetting case is defined as a separation of the surface into macroscopically wet and dry regions by a distinct boundary layer, i.e. the contact line. In case the volume of the liquid is small (i.e. it is not sufficiently large to be flattened under gravity), it forms a spherical cap, e.g. a droplet, that is characterized by its contact angle $\alpha$. The spherical shape of the droplet is maintained by capillary effects, i.e. the capillary or Laplace pressure. The spherical shape minimizes the free surface area for the given liquid volume, which in turn minimizes the total surface energy.

The periphery of the droplet, i.e. the three-phase contact line, is defined through Young's equation (Fig. 3.4). First derived in 1805 [126], it ties the interface energies[1] associated with the solid-air, solid-liquid and liquid-air interfaces together with the resulting contact angle of the liquid droplet on an ideal planar surface, i.e. one that is considered perfectly clean, rigid, smooth, flat and chemically homogenous. In any practical system, relaxation of these constraints quickly leads to non-systematic behavior.

The contact angle $\alpha$ directly tells us about the ability of the liquid to wet the surface. Theoretically, the contact angle can be defined simply by considering the force balance of the interfacial tensions at the liquid contact line. This is expressed in Young's equation:

$$\gamma \cos \alpha = \gamma_{\mathrm{SO}} - \gamma_{\mathrm{SL}} \tag{3.1}$$

[1]Note that "interface tension" and "interface energy" refer to the exact same physical quantity, expressed in different units: the former in $\mathrm{N/m}$, and the latter in $\mathrm{J/m^2}$. These terms are therefore often used interchangeably.

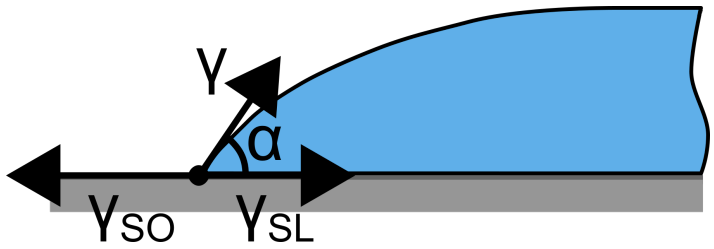


**FIGURE 3.4** Schematic of the contact line of a liquid droplet. The interfacial tensions affecting the contact line as well as the contact angle $\alpha$ are shown.

where $\gamma_{SO}$, $\gamma_{SL}$ and $\gamma$ are the surface-air, surface-liquid and liquid-air interface tensions of the system, with the latter $\gamma$ generally referred simply as the surface tension of the liquid. In the force balance, $\gamma_{SO}$ and $\gamma_{SL}$ oppose each other, reflecting the competition between solid-air (non-wetting) and solid-liquid surface (wetting) phases. The equilibrium contact angle $\alpha$ is dictated by the relative magnitudes of all three interface tensions so that a balance is reached, defining a stable contact line.

### 3.2.2 Wetting criteria: the spreading constant

Ideal surfaces can be broadly divided into two categories based on the magnitude of the surface-air interface tension $\gamma_{SO}$. First, there are "high-energy" surfaces, for which $\gamma_{SO}$ is in the order of a few $^{N}/_{m}$. This group includes surfaces of solid materials that generally exhibit strong chemical bonding, e.g. ionic compounds, metals and other covalent solids. Second, "low-energy" surfaces have $\gamma_{SO}$ up to a few tens of $^{mN}/_{m}$, and include weakly bonded materials such as polymer surfaces.

Considering the requirement of surface energy minimization, it is no coincidence that high-energy surfaces tend to provide much better wetting for liquids than low-energy ones, since introduction of a liquid layer is likely to reduce the total interface energy if $\gamma_{SO}$ is high. However, $\gamma_{SO}$ alone is not enough to predict the wettability of a given liquid. For that, we need the spreading constant $S$, which is defined as the relative difference of the total interface energies for dry and wet surfaces. In terms of interface tensions, this can be expressed as

$$S \equiv \gamma_{SO} - (\gamma_{SL} + \gamma) \tag{3.2}$$

Now, for $S > 0$, the total surface energy of the compound surface $(\gamma_{SL} + \gamma)$ is lower than that of the dry surface $\gamma_{SO}$, i.e. it is advantageous for the system to form two interfaces instead of one. The net surface energy is thus minimized for $\alpha = 0$, and we have total wetting. For $S < 0$, $\gamma_{SL} + \gamma$ is greater than $\gamma_{SO}$, so in order to minimize the net surface energy the wetting remains incomplete. The liquid is localized into a spherical drop with a finite contact angle $\alpha$ that is defined as a result of the interface tensions at the contact line, in accordance to eq. (3.1).

It is useful to note that the spreading parameter $S$ is linked to the material

properties of the solid and the liquid through the concept of interface energies. Let us consider a simple thought experiment where ideal solid and liquid media with only van der Waals -type bonding are first kept separate and then brought together. For a system of two semi-infinite solids (two surfaces), the total surface energy is first $2\gamma_{\mathrm{SO}}$. When the surfaces are merged together, the energy gain is equal to the so-called van der Waals energy $V_{\mathrm{SS}}$ which can be related to the polarizability $\sigma_{\mathrm{S}}$ of the solid $V_{\mathrm{SS}}$: $V_{\mathrm{SS}} = k\sigma_{\mathrm{S}}^2$, where $k$ is a constant. The resulting object has no interfaces, so these contributions must cancel each other out, e.g. $2\gamma_{\mathrm{SO}} - V_{\mathrm{SS}} = 0$.

Similarly, for a solid-liquid pair, the total surface energy is initially $\gamma + \gamma_{\mathrm{SO}}$, and the energy gain is equal to $V_{\mathrm{SL}} = k\sigma_{\mathrm{S}}\sigma_{\mathrm{L}}$, where $\sigma_{\mathrm{L}}$ is the polarizability of the liquid. The compound object has one solid-liquid interface, so the sum of the contributions must equal the appropriate interface energy: $\gamma + \gamma_{\mathrm{SO}} - V_{\mathrm{SL}} = \gamma_{\mathrm{SL}}$. And finally, for two liquid media, we get similarly $2\gamma - V_{\mathrm{LL}} = 0$, for the energy gain $V_{\mathrm{LL}} = k\sigma_{\mathrm{L}}^2$. We have thus estimated the interface energies $\gamma_{\mathrm{SO}}$, $\gamma_{\mathrm{SL}}$ and $\gamma$ in terms of the van der Waals energies $V_{\mathrm{SS}}$, $V_{\mathrm{SL}}$ and $V_{\mathrm{LL}}$, respectively. Using the definition of S, eq. (3.2), we may now relate it to the polarizabilities $\sigma_{\mathrm{S}}$ and $\sigma_{\mathrm{L}}$:

$$S = \gamma_{\mathrm{SO}} - (\gamma_{\mathrm{SL}} + \gamma) = V_{\mathrm{SL}} - V_{\mathrm{LL}} = k(\sigma_{\mathrm{S}} - \sigma_{\mathrm{L}})\sigma_{\mathrm{L}} \tag{3.3}$$

As it turns out in this simplified scenario, the sign of $S$ is solely determined by the relative magnitudes of the polarizabilities. As a general rule, the liquid spreads completely in case it is less polarizable than the solid.

Our materials of interest, silicon, falls well into the category of high-energy surfaces, and should be wetting for all liquids, including water. In practice however, the spreading of liquids on wetting surfaces is greatly constrained by practical inhomogeneity of the surface, result in incomplete wetting. As mentioned before, the surface chemistry of silicon/silica surfaces can be complicated. Water, due to its high surface tension, poses an additional complication since its surface, too, is particularly easily contaminated.

### 3.2.3 Contact line dynamics in partial wetting

On a practical surface, this simple picture of an individual value of the contact angle is convoluted by the presence of imperfections such as surface irregularities and contamination. One finds that the observed contact angle depends on the experimental details; in a practical experiment, a range of possible values is possible. This is referred as contact angle hysteresis, and the extreme angles $\alpha_{\mathrm{r}} < \alpha < \alpha_{\mathrm{a}}$ as the advancing and receding contact angles, respectively. The advancing angle $\alpha_{\mathrm{a}}$ designates the maximum angle the stable drop can attain without spreading laterally as the liquid volume is increased, and the receding angle $\alpha_{\mathrm{r}}$ designates the minimum angle prior to lateral shrinkage if part of the liquid was to be suddenly drained away.

The microscopic origin of contact angle hysteresis lies in the tendency of the

contact line to locally pin onto surface defects that may be either chemical or physical in nature. Hysteresis of the contact angle for sessile droplet is then observed as a consequence of multiple such events perturbing the ideal behavior [64]. In the event of forced wetting, such an event gives rise an elastic effect where the pinned contact line acts in the manner of a loaded spring, and this will be discussed in the theory section as it is also of possible relevance for colloid detachment from surfaces. Given that the magnitude of the hysteresis ties to the density of surface defects, its extent $\alpha_\mathrm{a} - \alpha_\mathrm{r}$ can be used as a quantitative measure of the surface quality.

Dynamic contact angles $\alpha_\mathrm{d}$ are also observed in the event of forced wetting, e.g. applying an external force to shift the contact line. These are of interest in the context of our immersion experiments that will be discussed in chapter 4. The forcing mechanism invokes a force of traction $F$ that induces the contact line to move. Incorporating this into Young's equation (3.1), we can instantly see that the contact angle can no longer maintain its static value:

$$F = \gamma_\mathrm{SO} - \gamma_\mathrm{SL} - \gamma \cos \alpha_\mathrm{d} \,. \tag{3.4}$$

The dynamic contact angle $\alpha_\mathrm{d}$ will now depend on the velocity of the motion. The derivation of quantitative expression for this dependence can be based on the viscous dissipation at a wedge-shape three-phase contact [28], and will be omitted here; for small contact angles ($\alpha \ll 1$), it can be written

$$V = \frac{V^*}{6l} \alpha_\mathrm{d} \cdot (\alpha_\mathrm{d}^2 - \alpha_\mathrm{e}^2) \,. \tag{3.5}$$

where $V$ is the velocity of the propagating contact line, $V^* \equiv \gamma/\mu$ is a characteristic velocity related to the capillary number $\mathrm{Ca}$, and $l$ is a dimensionless coefficient. For water, $V^* = 70\,\mathrm{m/s}$, and $l$ typically ranges from 15 to 20. This relation was derived to describe a scenario where a sample surface is being extracted from a liquid, i.e. $V < 0$ and $\alpha_\mathrm{d} < \alpha_\mathrm{e}$. It applies at moderate interface velocities $V$; at high velocities, the contact line is disrupted, and a macroscopic residual meniscus forms instead. The threshold velocity for this can be found via differentiation of eq. (3.5); for water and moderate $\alpha_\mathrm{e} = 0.1$, it corresponds to about $0.2\,\mathrm{mm/s}$.

We may try to apply eq. 3.5 to estimate how much the dynamic contact angle varies from its static value in the circumstances of our immersion cleaning experiments for carbon nanotube samples. The geometry is now inverted, so we must take $V > 0$ and $\alpha_\mathrm{d} > \alpha_\mathrm{e}$ since the contact angle grows from its static value as the sample is pushed into the liquid. At the limit of a wetting surface ($\alpha_\mathrm{e} \to 0$, such as our plasma-treated silica substrates) one first finds that $\alpha_\mathrm{d} \propto V^{1/3}$. For $V = 0.1\,\mathrm{mm/s}$, $\alpha_\mathrm{d} = (6l \cdot V/V^*)^{1/3} \approx 3.2°$, and only $6.9°$ for $V = 1\,\mathrm{mm/s}$. It is thus implied that the dynamic contact angle $\alpha_\mathrm{d}$ is only slightly disturbed from its static value $\alpha_\mathrm{e}$ due to the contact line motion at velocities relevant to our experiments.

### 3.2.4 Total wetting: Tanner's law and the precursor film

In case the wetting is total, droplets tend to spread out fully on the surface. This process is subject to dynamics of its own. The time-evolution of the droplet contact angle (and by extension, its radius) is given by a simple relationship:

$$\alpha(t) \approx \left(\frac{L}{V^* t}\right)^{3/10}, \tag{3.6}$$

where $L$ relates to the volume of the droplet, $L \approx \Omega^{1/3}$. This $\alpha \propto t^{-3/10}$ dependence applies remarkably universally for non-volatile liquids on smooth, clean surfaces. The law however argues that spreading should be independent of the value of spreading constant $S$ (as long as it is positive). Considering that the force experienced by the contact line (eqs. (3.2) & (3.4), at $\alpha \to 0$) essentially equals to $S$ on a wetting surface,

$$F = \gamma_{\mathrm{SO}} - \gamma_{\mathrm{SL}} - \gamma \cos \alpha_{\mathrm{d}} \approx \gamma_{\mathrm{SO}} - \gamma_{\mathrm{SL}} - \gamma = S,$$

this comes off as surprising. The solution for this dilemma is the precursor film, a nanometer-scale meniscus that precedes the macroscopic contact line ahead of it (Fig. 3.5). The excess force brought about by the spreading constant is balanced by the tensions of the film, which reduces the net force experienced by the contact line:

$$F_{\mathrm{net}} = F_{\mathrm{drop}} + F_{\mathrm{film}} = (-\gamma_{\mathrm{SL}} - \gamma \cos \alpha_{\mathrm{d}}) + (\gamma_{\mathrm{SL}} + \gamma) = \gamma - \gamma \cos \alpha_{\mathrm{d}}.$$

Equation (3.6), originally discovered in 1979 by L. Tanner, is referred as Tanner's law, and states that part of the energy nominally associated with the spreading process is dissipated in the precursor film instead. Given the law for the contact angle $\alpha$, time-evolution of the droplet radius $r$ can also be expressed similarly:

$$r(t) \propto L \left(\frac{V^* t}{L}\right)^{1/10}. \tag{3.7}$$

This follows from the conservation of liquid volume in the droplet: $\Omega = \pi/4 \cdot r^3 \alpha_{\mathrm{d}}$.

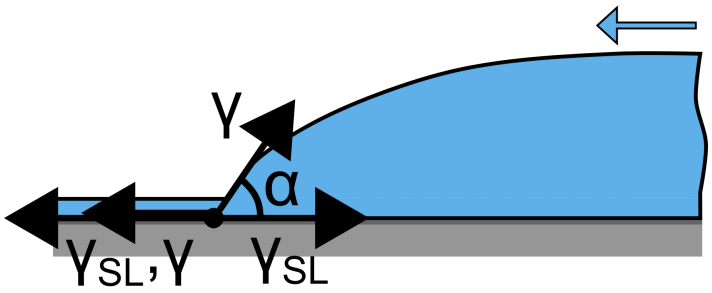


**FIGURE 3.5** Contact line of a spreading liquid droplet in the presence of a precursor film. The force balance is altered by the tensions of the precursor.

# Chapter 4

# Experimental work

This chapter discusses the experimental investigations published in the papers accompanying this thesis [49–51]. Each article will be discussed in its own section, placing emphasis on the experimental methodologies and the key results. The chapter starts with an overview of the sample preparation process that is largely common to all the experimental works.

## 4.1 Preparation of carbon nanotube samples

The approach for preparing carbon nanotube samples starting from CNT powder and silicon wafers is similar in all the works presented in this thesis, and will therefore be introduced at this point.

In the studies discussed in this thesis, commercial carbon nanotube materials were used. The material, delivered in powderous form, is used as-received, dissolved into 1,2-dichloroethane (DCE). CNTs are generally poorly soluble in most liquids, and surfactants need to be used with mild solvents e.g. water. CNTs readily dissolve into DCE, and MWNTs in particular form a stable suspension where ultrasonic treatment is sufficient to prevent aggregation and bundling of the species.

A weighed amount of carbon nanotube powder is washed into a storage bottle with a measured volume of DCE to make a quantitative solution, followed by mixing via manual agitation and ultrasonication. This gives rise to a uniform mixture with individual, non-bundled CNTs accompanied by inherent carbon-based debris. In most experiments, the initial dispersion is used as a stock solution for further dilutions utilized in the experiments.

The solutions remain usable for a period of a few months. An additional sonication treatment is carried out to ensure their stability prior to each deposition. After several months, the quality of the depositions begins to suffer as the solutions starts to aggregate, and in extreme cases visible inhomogeneity can be seen in the liquid.

Silicon wafers with (100) crystal orientation are utilized as the substrate material, either as plain wafers, or with a thermally-grown silicon oxide layer. In these works,

$8\,\mathrm{mm} \times 8\,\mathrm{mm}$ sample chips have been used. The sample preparation is of great importance in our studies, and the following process (Fig. 4.1) has been utilized in all the works:

- 10-minute ultrasonic treatment in warm acetone ($\sim 30\,^{\circ}\mathrm{C}$) using a bath-type sonicator.
- Gentle scrubbing with cotton sticks in similar bath.
- Rinsed in isopropyl alcohol and dried under nitrogen flow.
- Exposed to jets of cold $CO_2$ gas at approx. $45^{\circ}$ angle of attack relative to the surface[1].
- Surface treatment:
  - For hydrophilic surface, oxygen plasma treatment in Reactive Ion Etching (RIE) apparatus (2 min, ambient temperature with $200\,\mathrm{W}$ forward power). This also provides effective removal of all organic residues.
  - For hydrophobic surface, brief (1 min.) immersion in dilute (2-4 %) hydrofluoric acid (HF) solution.

[1]Cleaning by $CO_2$ dry ice is among the most effective laboratory-scale cleaning methods for removal of adhered species from the surfaces [120]

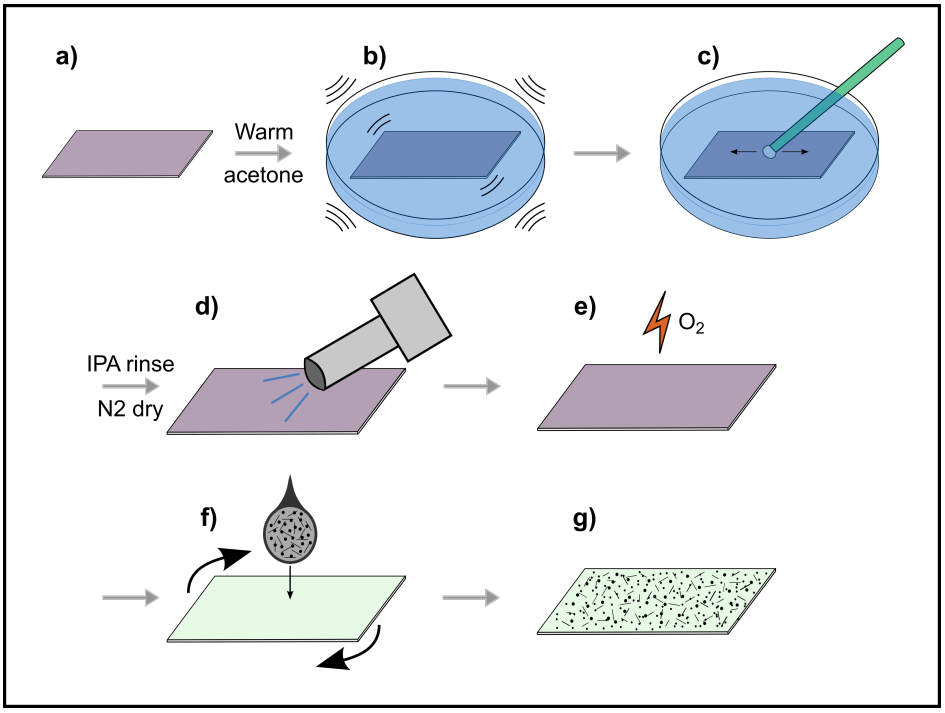


**FIGURE 4.1** Preparation of carbon nanotube samples in the experiments described in this thesis: (a) (100)-oriented $Si/SiO_2$ prime wafer; (b) ultrasonic treatment in acetone bath; (c) cleaning with cotton sticks followed by rinsing in isopropyl alcohol, and subsequent drying; (d) cleaning by $CO_2$ dry ice jet; (e) surface treatment (oxygen plasma / HF immersion); (f) carbon nanotube deposition via spin coating; g) finished sample with uniform CNT deposition.

We note that aside from the prerequisite surface treatment, we wish to avoid the use of strong chemical processes, such as the well-known RCA clean, in the pre-cleaning of the wafers to maintain a clear picture of their surface-chemical state.

Following the preparation of the substrate, the deposition of CNTs is carried out from the existing solutions via spin coating that has the benefit of providing a macroscopically uniform deposition. A few, individual droplets of the solution are deposited using a disposable glass pipette as the sample is rotating. Generally, the spinning speed is $3000\,\mathrm{rpm}$, and the total spinning time is selected in such a way that all the droplets have time to fully spread out and dry. This process generally gives rise a highly uniform deposition as seen under dark-field optical microscope, aside from minor aggregation or sparseness often witnessed near the sample edges.

## 4.2 Sessile droplets on MWNT samples

The first section deals with the content of our first published research article [51]. In this paper, our original intent to measure spreading dynamics of liquid drops deposited on carbon nanotube samples was largely overshadowed by the annular depletion of matter that formed in response to the spreading. Given that the diameters of these annuli roughly coincided with those of the droplets at the end of the spreading process, we ultimately concluded that the depletion is strictly due to the interaction of the particulate deposition with the mobile contact line. In the subsequent analysis, the structure of the annuli was analyzed in detail.

### 4.2.1 Experimental methods

The experimental process is schematically described in Fig. 4.2. The preparation of CNT solutions and the samples took place as described earlier in section 4.1. In this work, arc-discharge synthesized, multi-walled nanotube powder from Mer corporation was utilized[2]. The powder was dissolved as-received into dichloroethane (DCE) in varying concentrations from $0.2$ to $0.5\,{}^{\mathrm{mg}}/_{\mathrm{ml}}$.

Si prime wafers (100 crystal orientation) were used as substrates. The silicon surfaces are covered by a thin native oxide in ambient environment, which was hydroxylated in oxygen plasma for uniformly hydrophilic surface character. Following the process, the water contact angle of such plain Si samples is close to 0, however the effect of the treatment decays gradually as samples remain exposed to ambient atmosphere [13]. In order to account for this factor, we made a separate series of experiments where the time elapsed from the RIE treatment to the experiment was varied in a deliberate manner. For control experiments, the substrate was rendered

[2]To characterize the MWNT material of choice, the ratios of tubes and particles (20 % & 80 %, respectively) were later estimated using AFM on a typical sample. Their diameters were typically from $10$ to $20\,\mathrm{nm}$, and lengths up to $2-4\,\mu\mathrm{m}$.

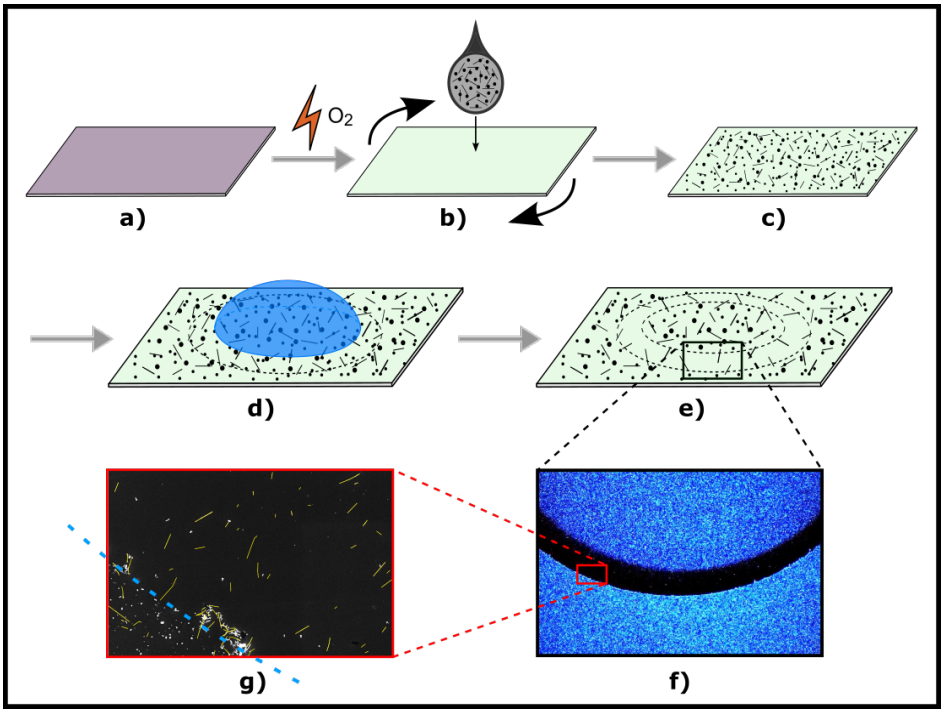


**FIGURE 4.2** Step-by-step schematic of the sample preparation and the droplet experiment. (a) The substrates are thoroughly cleaned Si wafers that undergo oxygen plasma treatment prior to (b) spin-coating of the CNT deposition (c). In the experiment, a sessile droplet (d) is placed on the sample and allowed to spread spontaneously for a given period of time. The emerging annular imprint (e) is investigated via optical (f) and electron microscopy, where dramatic reduction of synthesis-borne debris is seen within, while CNTs are retained in significant numbers (g, manual emphasis added on the CNTs for clarity).

hydrophobic by brief (about 1 min) immersion in a dilute (2-4 %) hydrofluoric acid (HF), or through evaporation of a thin film of gold on the surface.

To accommodate the demanding constraints set by the decaying surface chemistry, sessile droplet experiments were performed immediately after the sample preparation. We used a micropipette to inject a droplet of liquid on the CNT-deposited sample, and then flushed it away with pressurized air after a given period of time. Liquids used in the experiments included water (millipore ultra pure) and dilute (less than 20 % by volume) water-solutions of isopropyl alcohol (IPA). The droplet volume was typically from 1.5 to 3.0 µL, and its contact time prior to being flushed away approximately 20 seconds. Spreading of the droplets was recorded through the means of a high-speed camera with magnifying objective, mounted into side-view perspective. A separate ImageJ plug-in (DropSnake, [34]) was used to quantify the evolution of droplet contact angles and diameters from the side-view camera images.

The sample surfaces were characterized under dark-field optical microscope before and after the droplet experiment (Fig. 4.3). ImageJ image analysis software was utilized to determine the approximate thicknesses and diameters of the depletion

rings that emerged. Select samples were further imaged with scanning electron microscope (SEM) and atomic force microscope (AFM) to observe the cleaning imprints in greater detail.

A curvelet-based approach was utilized to study the orientation of any nanotubes remaining in the deposition. The details of this algorithm have been published in ref. [103]. Such SEM-based investigations are complicated by the tendency of the SEM electron beam to locally modify the surface conditions; this well-known effect is probably caused by deposition of a thin layer of amorphous carbon onto the beam spot from residual gases in the imperfect vacuum of the chamber [129]. In a separate trial, we concluded that high-magnitude imaging makes the deposition locally immune to the effects of the mobile contact line. For this reason, an indirect analysis was carried out, where the affected region of the sample was compared against neighboring, unaffected bulk deposition.

To determine whether the microscopic flow phenomena within the droplets had any role in our experiment, we used a spectral-domain optical-coherence tomography (OCT) instrument to visualize them on model samples.

### 4.2.2 Results

The static contact angles of sessile water droplets on the different surfaces were estimated with the side-view camera, and on plain, hydroxylated Si surfaces they were very close to 0°. On bare HF-treated samples, the angles were strongly dependent on the decay of the surface treatment with time: the contact angles measured close to 50° about 30 minutes after the HF treatment, but in 2.5 hours' time the angles were already closer to 30°. Incorporation of a spin-coated MWNT deposition generally resulted into intermediate contact angles (10°–50°) on both substrate types. On a silicon substrate covered by evaporated Au film and MWNT deposition, the contact angles were much higher, reaching closer to 90°.

Strong sample-to-sample variation was witnessed in all the contact angle values, which is hardly surprising considering the non-exact nature of the spin coating process. There was no evident difference in the quality of the carbon nanotube deposition with respect to the sample surface chemistry, i.e. depositions on hydrophobic substrates were as dense and as uniform as on hydrophilic sample when viewed under optical microscope.

Following the spontaneous spreading of sessile drops on the samples, annular features could be discerned in depositions prepared on hydrophilically prepared Si substrates via dark-field optical microscopy (Fig. 4.3b). The circular imprints, typically in the order of a few mm in diameter, could also be vaguely seen under a bright light with naked eye. In contrast, no changes could be observed on depositions prepared on hydrophobic surfaces.

In the center of the annuli, there is a large region where the deposition resembles that of the bulk outside, aside from thin secondary ring-shapes that are frequently

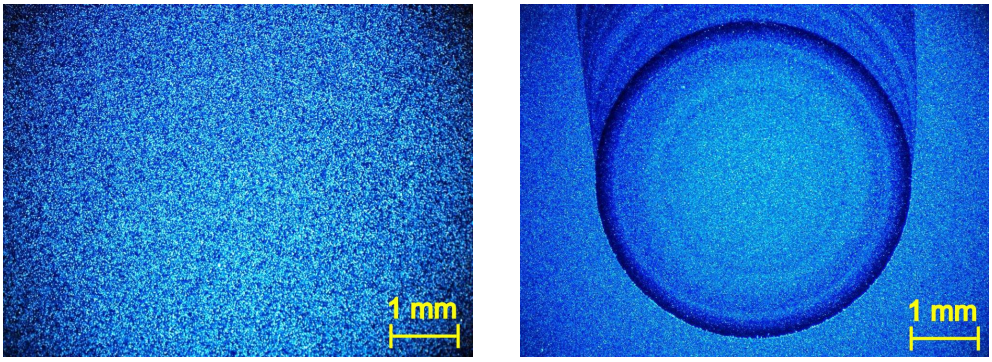


**FIGURE 4.3** Dark-field optical micrographs of MWNT depositions: (a) Pristine, freshly spin-coated deposition; (b) annular imprint formed by spreading of a water droplet on a similar deposition.

present. These subtle features were likely related to the quick initial phase of the spreading as the drop oscillates before acquiring its semi-static (cap of a sphere) shape. The transient phenomena associated with this highly dynamic settling-in phase that compasses perhaps the first $10 - 100\,\mathrm{ms}$ of the process were not discussed further in this work.

The dynamic spreading curves (diameter vs. time) of water drops of different volumes are shown in Fig. 4.4. It is clear that the outer diameter of the imprint approximated from the dark-field micrographs, $D_{\mathrm{ro}}$, generally agrees with the value of $D_{\mathrm{SV}}$, the dynamic diameter of the droplet as measured via side-view video microscopy at the end of the experiment; the slight differences in these two diameters may be due to limited lateral resolution of the side-view imaging configuration, and the shape of the annuli that was often not fully circular.

At the inner boundary of the annuli, one can see smooth transition from the interior towards the outer perimeter, with the depletion of particles increasing radially. The inner annular diameter, $D_{\mathrm{ri}}$, is not readily assignable to any fixed point of the spreading curve, and coincides with relatively early phase of the spreading process (less than $0.1\,\mathrm{s}$). Given that there exists a seemingly unaffected central region suggests that the spreading (i.e. the progression of the droplet contact line) must be sufficiently slow before the depletion of particles from the surface becomes possible. Contrary to the inner boundary, the outer annular interface is abrupt, and often shows excess particle accumulation, probably due to delivery of matter detached from the annular region by the progressing contact line.

Imaging (Figs. 4.5 & 4.6) demonstrates that the apparent annular imprint is brought about by efficient removal of irregular carbonaceous debris from the affected region. Carbon nanotubes, on the other hand, show remarkable resilience against removal. Most complete depletion of particles appears to take place near the perimeter of the annulus, with the effect weakening radially towards the center.

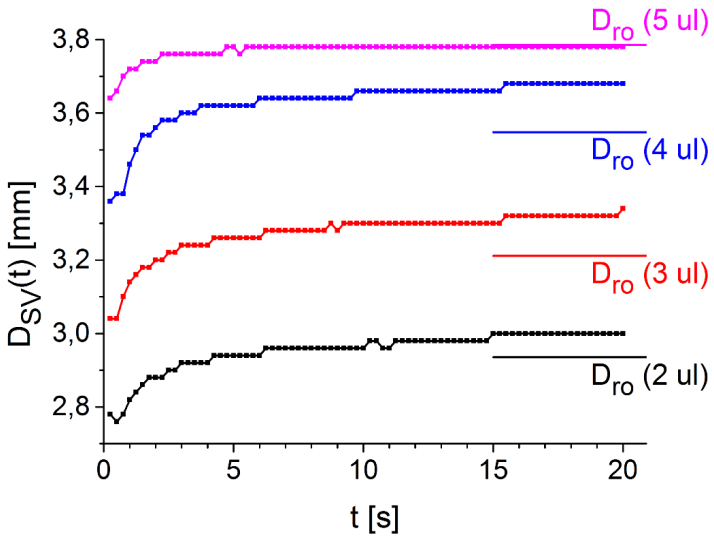


**FIGURE 4.4** The progression of the droplet diameter measured from the side view data ($D_{\mathrm{SV}}$) during the spreading process for different droplet volumes. The spreading starts with a highly dynamic initial phase that is too rapid to be quantified here. Eventually, the diameter reaches a semi-stable end value that corresponds the outer diameter of the imprint $D_{\mathrm{ro}}$.

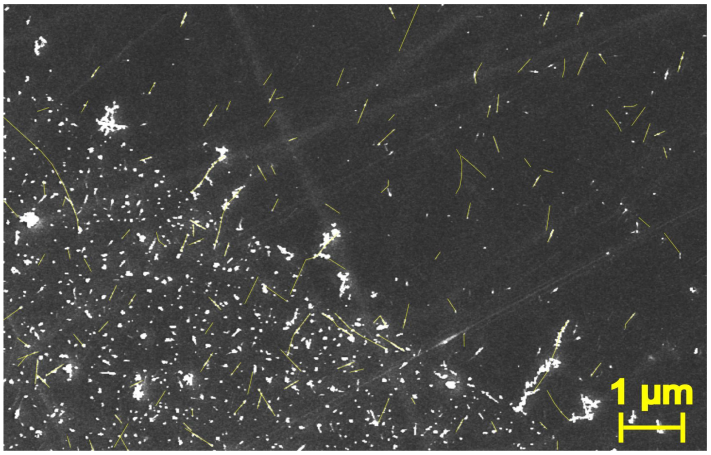


**FIGURE 4.5** SEM image depicting the outer interface of a depletion annulus. Radical decrease in the amount of debris over the interface can be seen, while the annular region is still densely populated by MWNTs. The CNTs were manually emphasized for clarity.

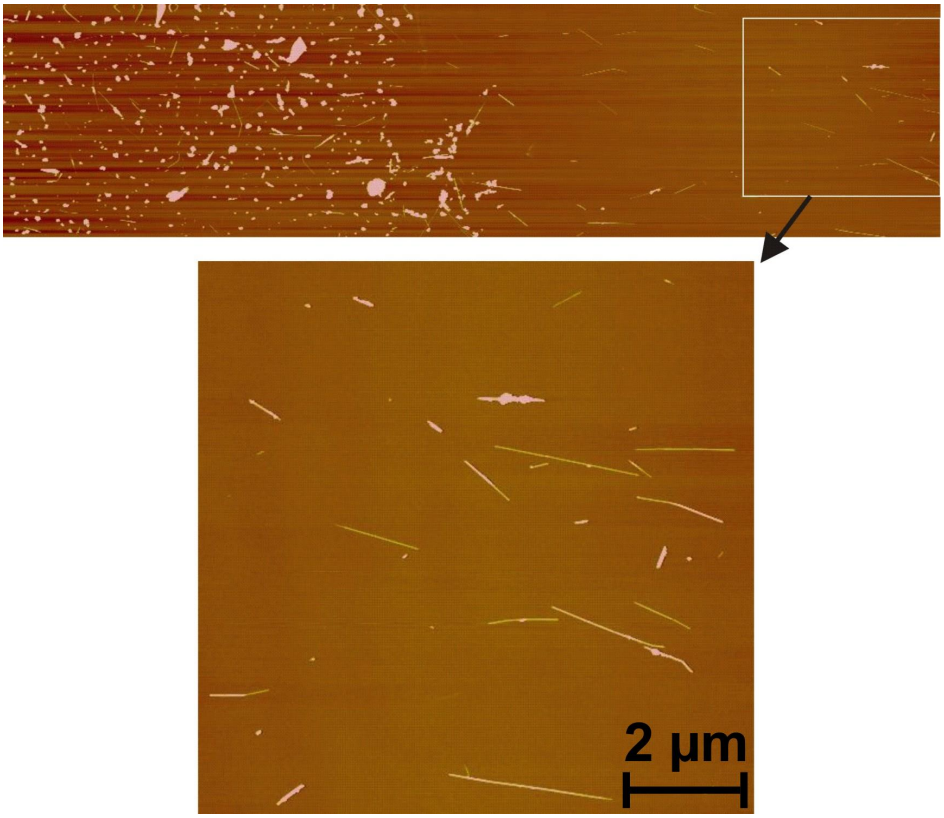


**FIGURE 4.6** The outer interface as imaged in AFM: $40\ \mu\mathrm{m} \times 10\ \mu\mathrm{m}$ image, with $10\ \mu\mathrm{m} \times 10\ \mu\mathrm{m}$ blow-up. A rich CNT deposition is retained within the annular region. Gathering of excess debris can be seen at the perimeter.

AFM images (Fig. 4.6) were taken on both sides of the perimeter interface on selected samples to quantify the degree of the cleaning. Within the annular region, the fraction of CNTs of all particles varied from 40 % up to 75 % on different samples, a significant increase from approx. 20 % in the bulk deposition. The gathering of excess debris particles at the outer perimeter is also evident in Fig. 4.6.

Some of the SEM images indicated apparent reorientation of carbon nanotubes located within the depletion annulus compared to those in the neighboring bulk deposition, implying that the orientation of the MWNTs could have been altered by the mobile contact line of the spreading droplet. We investigated this by determining the orientation spectra of the SEM images captured of the deposition on both sides of the imprint perimeter at select sites.

The results of the orientation measurements are summarized in Fig. 4.7. Orientation spectra from SEM images taken within the annulus (red and blue curves) show a peak corresponding to the vertical orientation direction, while the curve of the bulk deposition immediately outside the annular perimeter lacks such an apparent feature. It is thus implied that the propagating contact line of the expanding droplet is able to significantly alter the orientation state of the MWNT deposition.

In an attempt to account for the possible residual orientation effects caused by

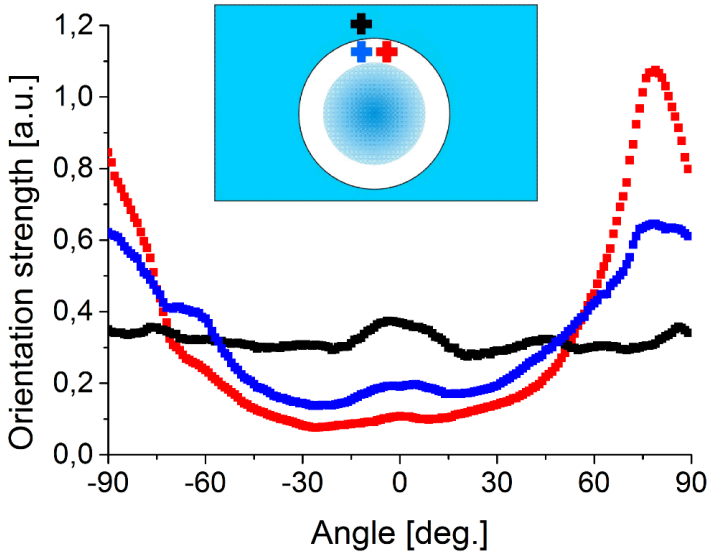


**FIGURE 4.7** Schematic of the orientation measurements, and the associated orientation spectra. Dominant vertical orientation is indicated within the annulus.

the spin coating [75], we had also imaged several sites around the same sample prior to the drop experiment. Similar to the black curve in Fig. 4.7, orientation spectra of the pristine deposition generally lacked dominant features.

Experiments were also performed with water/IPA mixtures up to an alcohol concentration of 10 %. In order to account for the dynamic nature of the sample surface state in ambient air, we separately took into account the processing delay from sample preparation to the execution of the experiment (measured in hours). As it turned out, both the spreading of the drops and the morphology of the annular imprints were influenced by these variables. Figure 4.8 shows the results of these trials, with the the diameter of the annular imprint, $D_{\mathrm{ro}}$, compared against the final diameter of the droplet, $D_{\mathrm{SV}}$. It can be seen that increasing the time delay decreases the dynamic diameter of the drop, which translates to higher contact angle. Addition of IPA to the mixture appears to have the same effect, although there is no discernible difference between $2\,\%$ and $10\,\%$ solutions. In visual comparison of micrographs captured from the annuli (Fig. 4.9), imprints of the composite drops feature a blurred interior, and accumulation of excess matter at the perimeter is pronounced.

Implications of convective flows within the drops were also considered for our study. Spontaneous evaporation of the liquid is fastest at the perimeter of the drop. This causes direct convective flows within, which for example explains the formation of "coffee ring" depositions inherent to colloidal solutions [25]. Furthermore, other forms of microconvection, such as recirculating Marangoni flows, may also compete with the radial flow [26, 54].

The dynamics of spontaneously spreading droplets have been a widely investigated subject in literature, but direct experimental methods to study their internal convection have been lacking. With the introduction of optical-coherence tomogra-

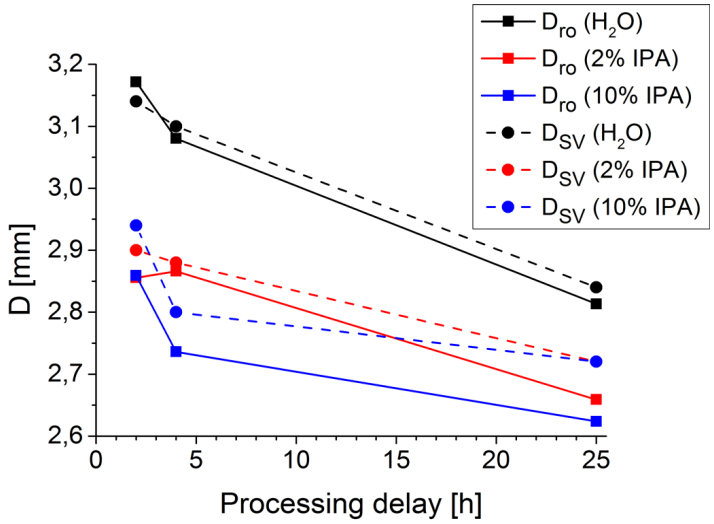


**FIGURE 4.8** Comparison of the end-state diameter of the drop as measured from the side-view, $D_{\mathrm{SV}}$, to the annular diameter based on the optical micrographs $D_{\mathrm{ro}}$, for 2 µL pure water droplets and water/IPA solutions as a function of the processing delay.

phy (OCT), it has now become possible to carry out such imaging 'in situ' [35]. Our imaging efforts suggested that the organized flow patterns, such as those reported in [77], only became visible from 40-60 seconds from the onset of water droplets on model samples, i.e. well after the typical spreading time (about 20 seconds) in the experiments. In water/IPA composite drops, the flows were generally more erratic and disorderly, only settling down gradually.

It thus seems that microconvective flows only become relevant in water droplets once their dynamic spreading phase has already ceased. Considering that the onset of evaporative flow in particular has been known to depend on pinning of the contact line [25,26], it is hardly surprising that they are unlikely to contribute to the depletion imprint formation clearly associated with the spreading of the drop. In case of IPA-water mixtures, the erratic flow behavior might however contribute to the redeposition of debris at the interface of the imprint, if the smeared interior of the annulus is associated with a degree particle detachment in bulk liquid.

### 4.2.3 Discussion

The outcome of these experiments is that circular annuli were formed on depositions of carbon nanotubes synthesized via the arc-discharge method by spreading of sessile drops of water and IPA, and that the depletion of matter is probably due to the propagating contact line of the spreading droplet that largely vacates the annular region from debris originating from the synthesis, while CNTs are retained in large numbers. This only takes place on hydrophilic silicon substrates, while no apparent annuli are observed on hydrophobic surfaces. Lack of specific surface treatment of the underlying substrate was found to result in unsystematic behavior regarding to

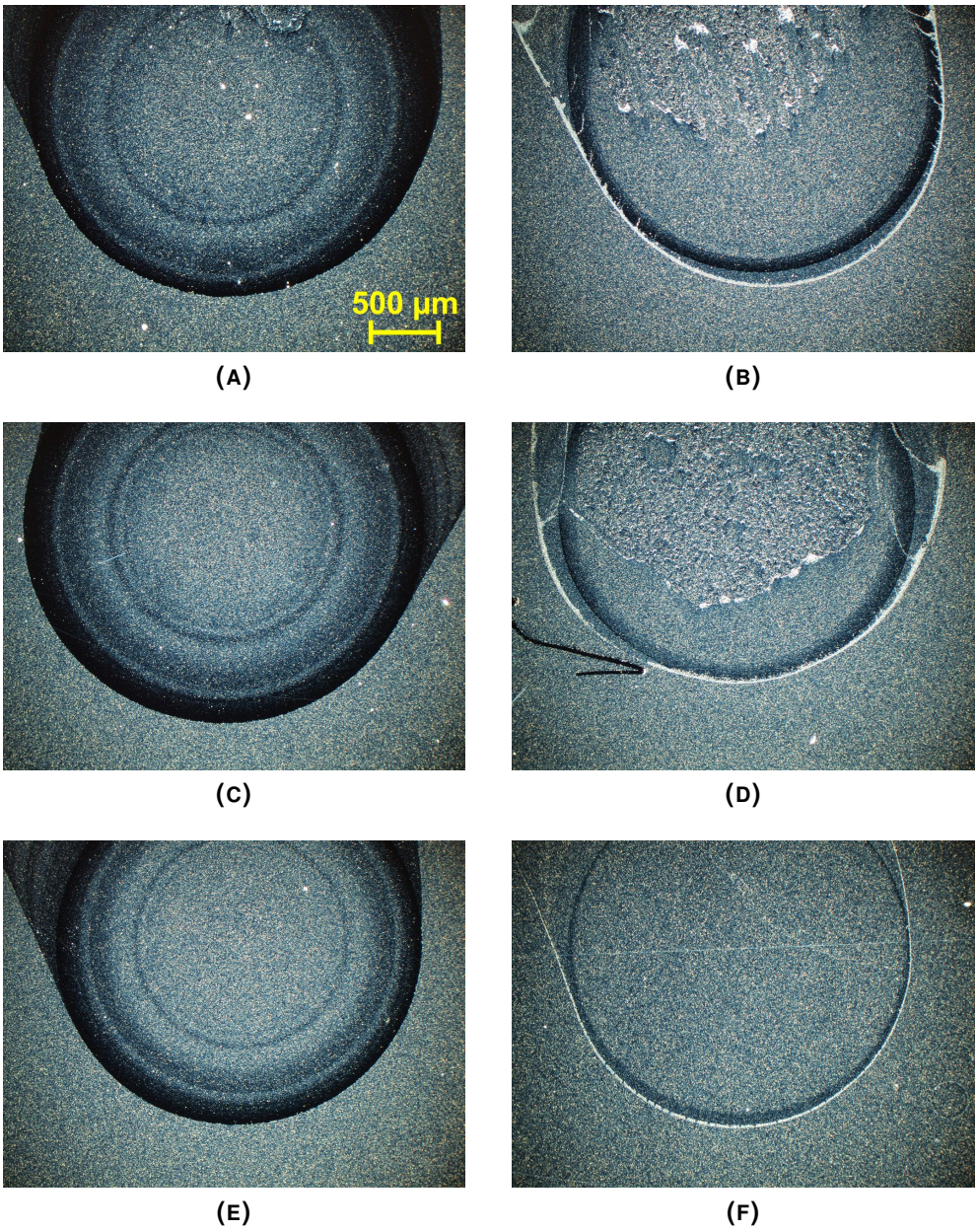


**FIGURE 4.9** Evolution of the imprint with increased processing delay and added isopropyl alcohol content: (a, c, e) annuli formed in response to DI water droplets at 2, 4 and 25-hour time delays, respectively; (b, d, f) similar data for 10 % IPA-water mixture. The annuli are about 3 mm in width, and each micrograph is in the same scale. The data for 2 % mixture is omitted for brevity.

the formation of the annuli.

The structure of the annuli formed by water droplets (interior where no particle detachment is observed; gradual onset and radially increasing detachment in the direction of the drop spreading; abrupt outer perimeter where some excess matter may gather) suggests that the detachment process takes place strictly at the contact line of the spreading droplet, and that it can only take place once the velocity of the contact line is sufficiently slow. OCT measurements show that hydrodynamic flow phenomena play no central role in the formation of the annuli.

The contact angles of water/IPA composite droplets were found higher than those of pure water drops. Considering the lower surface tension of the solution [117], this is surprising; in many circumstances[3], lower contact angles are expected instead [65,116]. The observation coincides with the trends in the imprint morphology in Fig. 4.9, where both increased IPA content and time delay implicates narrower droplets and annuli. In reference to Fig. 4.8, one can see that this further correlates with the reduction of the imprint diameter as well. Given this unexpected result, we tentatively conclude that stronger pinning of the contact line must take place in IPA-containing drops, which causes the spreading to be brought to halt sooner. Such pinning could be brought about by the debris particles accumulating at the air-liquid interface during the spreading process.

We link this hypothesis to the other exclusive features witnessed in the morphology of the narrower annuli formed by the compound droplets: both the blurred interior of the annulus and the excess matter gathered at the perimeter suggest greater overall detachment of particles from the surface, even though the depletion rings are thinner compared to pure water droplets. While the addition of IPA to the mixture decreases its surface tension, the chemical detergency is improved, and as such it is possible that for the compound droplets a degree of particle detachment took place in the bulk liquid as well. If microconvection is then sufficiently strong to transport this matter to the interface, stronger pinning might result due to the contact line getting more crowded by particles. This would in turn cause the spreading dynamics to slow down sooner, leading to thinner depletion rings with excess debris deposited at the perimeter.

Similar to adding IPA to the drops, increased processing time delay from the surface plasma treatment to the experiment appears to result in narrower droplets and imprints. This is in agreement with the surface chemistry of the native silicon oxide layer decaying from hydroxylated towards a more heterogenous state in the ambient environment, which results into larger dynamic contact angles, and, in our case, thinning of the depletion ring.

In Fig. 4.8, one can see that the effect of the surface chemistry decay on the

[3]In general terms, there is no conceivable reason why incorporating a more wetting liquid should result to higher contact angle for the binary solution on a clean surface. This can also be qualitatively seen from eq. 3.1 for $0° < \alpha < 90°$ if one assumes that $\gamma_{\mathrm{SL}}$ does not change much. Hence, the effect must be related to the presence of the CNT deposition instead.

spreading can be rather substantial within time scale of one day. Control of the silicon surface chemistry was one of the main challenges in this study; first attempts where the samples were only cleaned in surface-neutral manner prior to the CNT deposition suffered from very poor repeatability. Introducing the oxygen plasma RIE treatment improved the qualitative repeatability of the imprint formation, but given the lack of controlled environment there is no guarantee that the samples associated with different experimental series evolve in equal manner. As a result, quantitative comparisons can only be made within each experimental series.

We found that maximum width of the imprint generally agrees with the diameter of the drop at the end of the spreading process, while the inner diameter at the onset of the annulus corresponds to timescales less than 0.1 s after the spreading had started. It is however difficult to make definitive statements about the factors influencing the spreading process, and whether the thickness of the depletion ring has any independent meaning. It would be interesting to carry out a detailed measurement of the spreading dynamics to assign the onset of the imprint more accurately in the spreading curve. In principle, it should be possible to associate the velocity of the decelerating contact line with the radial extent of particle detachment, and evaluate its velocity-dependence in continual manner. This would however set demanding constraints on the high-speed video microscopy of the drop spreading, and require radial evaluation of the particle density within the annulus. Such systematic, quantitative analysis was deemed outside the scope of this work.

Although MWNTs were generally retained within the affected annular region, we could still see that the contact line of a spreading drop may have a significant effect on the local orientation of the remaining tubes: clear changes were witnessed in both the orientation strength and the dominant orientation direction at the annular perimeter. This effect overlaps with the inherent radial orientation caused by the spin coating of the deposition, which however appears rather weak in our samples. The interpretation of this orientation measurement is also complicated by the fact that the MWNTs were not segmented from debris particles in the SEM images; the orientation of the entire deposition, as a whole, was analyzed in each SEM image, and as such the density of the debris particles likely had a disrupting effect on the orientation witnessed at the bulk deposition.

The details of the orientation process are left unclear in this study; the number of sites that could be investigated was limited, and some of them show appreciably weaker results. Even if the effect is systematic, we do not know whether it is due to individual MWNTs becoming genuinely reoriented in response to the mobile contact line, or if certain orientation predisposes the tubes for detachment, leading to an apparent effect with respect to the unaffected bulk deposition.

Overall, this work implies that mobile liquid interfaces may be of use in improving the quality of CNT samples deposited on hydrophilic substrates in terms of purity. The practical application of this approach will be the topic of the next paper.

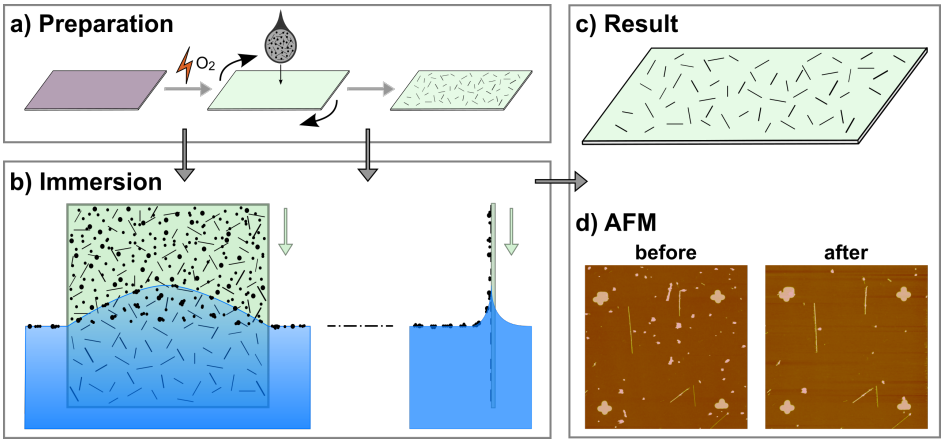


**FIGURE 4.10** Step-by-step schematic of the immersion process. a) The Si/SiOx substrates are prepared via pre-cleaning, oxygen plasma treatment and spincoating of the MWNT deposition; (b) immersion takes place vertically into ultraclean water, causing selective detachment of irregular debris particles from the surface, while (c) MWNTs are still retained on the surface in large numbers; (d) the extent of cleaning can be evaluated quantitatively through the means of comparative AFM imaging.

## 4.3 On-chip purification of arc-discharge MWNTs

In the second paper, we shift our focus to purification of practical carbon nanotube samples [49] by mobile liquid interfaces, based on the discovery of the cleaning effect in the previous work. I will review the methodology and protocols we utilized in our experiments, and follow up with the central results of our paper. Discussion primarily focuses on interpretation of main features of the purification effect; more thorough theoretical analysis of the particle-scale detachment process will be presented later in the theory chapter.

### 4.3.1 Experimental methods

Figure 4.10 present sample preparation and the experiment. Contrary to the previous article, the MWNTs utilized in this work were obtained from Sigma-Aldrich. According to the manufacturer, the material contains $20 - 30\,\%$ of MWNTs, with diameter and length ranges of $7 - 12\,\mathrm{nm}$ and $0.5 - 10\,\mu\mathrm{m}$, respectively; in practice, the diameter distribution is broader than this according to the AFM, and the MWNTs are limited to lengths of a few micron. This is probably due to shortening by repeated ultrasonic treatments. The powder was first dispersed in 1,2-dichloroethane in $0.50\,{}^{\mathrm{mg}}/_{\mathrm{ml}}$ concentration as-received to create a stock solution that was then diluted down to $0.25\,{}^{\mathrm{mg}}/_{\mathrm{ml}}$ for practical dispersion. Otherwise, the preparation of the MWNT dispersions, and their deposition onto the samples matched the process already described in the introductory chapter 1.

Two types of patterned substrates were utilized in these experiments. To allow for atomic force microscopy (AFM) imaging of the same site prior to and following the

immersion process, reference marks were fabricated with electron beam lithography and vacuum evaporation. We used commercial $(100)$-oriented silicon, highly-doped ($\rho = 0.005 - 0.020\,\Omega\mathrm{cm}$) silicon substrates with thermally grown oxide layer ($\sim 300\,\mathrm{nm}$) pre-cut to 6 mm x 6 mm size. The substrates were first thoroughly cleaned as described in the introductory section, save for the oxygen plasma treatment. Bilayer photoresist was then spin coated on the surface (9% MMA (8.5) MAA copolymer layer in ethyl lactate spun at 3000 rpm for 60 s, followed by 4% PMMA in anisole at 6000 rpm for 60 s). The marker pattern was then drawn via electron beam exposure. Following the development of the exposed region (treatment in Isopropanol/MIBK 2:1 followed by Methanol/Methoxyethanol 2:1), a metal layer was deposited using vacuum evaporator, consisting of approx. 20 nm of Au over 5 nm Ti adhesion layer. The structure was finalized with lift-off of the excess metal in acetone.

Another type of substrates patterned with grooves were fabricated with etching instead of evaporation on similar $Si/SiO_2$ chips. The patterning of 10 $\mu\mathrm{m}$ long and 300 nm wide trenches was done via e-beam lithography, using PMMA as a protective resist layer. A well-known reactive ion etching process ($CHF_3$ / Ar plasma, 200 W forward power) was then utilized to etch troughs on the oxide layer for 2 minutes, corresponding to approximate groove depth of approximately 100 nm (etch rate 55 nm / minute). Finally, the excess resist was dissolved in acetone. Prior to the CNT deposition, preparation of the structured samples was similar to the regular ones except that no cotton sticks were used in pre-cleaning of the markered substrates to ensure their preservation.

In order to minimize the dynamic effects of the surface chemistry, the experiments were done within 6 hours from sample preparation [13]. The sample was attached onto an aluminum shaft connected to a motorized triaxial sample stage that was controlled via a computer interface. The immersion took place vertically into a container of ultrapure water with a constant immersion velocity $v_{\mathrm{im}}$, varied from 0.01 to 1 $^{\mathrm{mm}}/_{\mathrm{s}}$. The shaft was lowered until the entire sample was submerged, the three-phase air-water-substrate contact line thus sweeping over the entire surface. The process was monitored with a side-view CCD camera equipped with a magnifying objective.

Once the sample was fully submerged, it was rapidly retracted ($v_{\mathrm{re}} \sim 1\,^{\mathrm{mm}}/_{\mathrm{s}}$), and subsequently dried under nitrogen flow. Based on preliminary experiments, it was found essential to evacuate several ml of water from the surface layers with a pipette prior to the sample recovery, as the detached particulate matter residing on the water surface tended to re-deposit onto the sample, presumably when the sample was being retracted. Pipetting did not fully suppress the formation of re-deposits, with small, isolated features still occasionally appearing on the surfaces.

The cleaning effect was characterized by a combination of dark-field optical microscopy, atomic force microscopy and scanning electron microscopy. Given that each technique has its own strengths and weaknesses, the use of combined, mutually

supplementing approaches is necessary. Optical microscopy is limited to visualizing the deposition at micrometer scale. Scanning electron microscope allows for quick imaging of individual NTs, but suffers from lack of contrast due to uneven charging effects, and is known to modify the local surface conditions [129]. AFM avoids these issues while providing the best vertical resolution, but is too time-consuming to be used as the primary screening method.

The surfaces of all samples were inspected both prior to and following the immersion process with dark-field optical microscopy. For quantitative evaluation of particle detachment, comparative AFM imaging was carried out both before and after the immersion at the same location on each sample with the help of the microfabricated references. We also developed an ImageJ script for batch analysis of the AFM data, to identify the tubular species in the images and tabulation of the detachment fractions of debris particles and carbon nanotubes. Selected samples were further inspected with scanning electron microscope (SEM).

Preliminary Raman characterization of the individual tubes was also performed on these same samples, with a small number of clean, unobstructed MWNTs selected for analysis based on the AFM images. These measurements were made with a self-assembled, backscattering-type Raman setup using $532\,\mathrm{nm}$ excitation wavelength with about $1\,\mu\mathrm{m}$ beam spot, sufficient to focusing on individual MWNTs.

### 4.3.2 Results

**General features of the purification effect**

Based on our experiments described above, following general remarks can be made:

- The immersion process gives rise to significant reduction in the particle density. This contrast is well-illustrated in Fig. 4.11b, an optical micrograph of a sample where the immersion was halted before the entire surface was wetted.
- The resulting sample surfaces are generally uniform. Given that no excess debris can be seen at the interface shown in Fig. 4.11b, it is suggested that the affected particles do not translocate along the surface, but are rather fully detached from it.
- Based on SEM imaging (Fig. 4.12), clean MWNTs are retained throughout on the cleaned surface, along with some small contaminant particles. A strongly selective and systematic detachment of irregular debris in favor of carbon nanotubes has thus been established.
- The hydrophilic pre-treatment of the silicon substrate is a requisite for the cleaning effect to take place. Related experiments verified that there is no apparent effect on the MWNT deposition in case hydrophobic surface treatment (brief immersion in dilute HF) is carried out instead, as is expected based on our previous work.

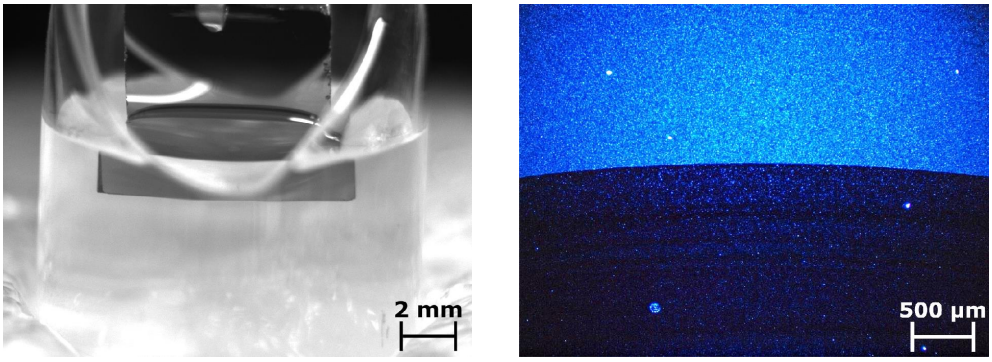


**FIGURE 4.11** (a) Side-view of the immersion process on a typical sample. (b) Sharp interface separating the cleaned surface from the bulk deposition on a partially immersed sample, as seen in dark-field optical microscope.

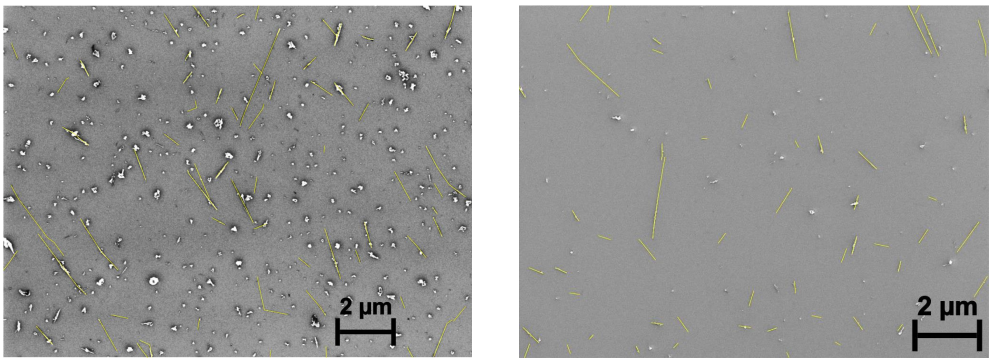


**FIGURE 4.12** (a) Scanning electron microscope image of a pristine, non-purified arc-discharge MWNT deposition obtained by spin coating. (b) View of a similar deposition following the immersion treatment. CNTs have been manually emphasized for clarity.

- Repetitions of the immersion process on an individual sample yielded no further improvement of the cleaning effect as observed via dark-field optical microscopy.
- Pipetting of the water surface is a requisite for neat, uniform cleaning effect. In the absence of this, coordinated redeposition of rafts of entangled MWNTs and debris particles may take place during the retraction of the sample. Pipetting does not completely eliminate such recontamination, but mitigates its effects.
- This suggests that the detached debris must reside on the liquid surface following the immersion. Such presence implies that the advancing contact (during the immersion step) line must be largely responsible for the purification process, rather than the receding line at the retraction phase.

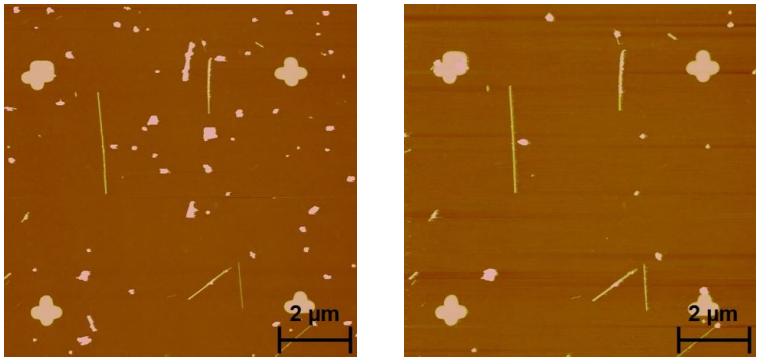


**FIGURE 4.13** $10\,\mu\mathrm{m} \times 10\,\mu\mathrm{m}$ AFM images captured at the same location, prior to (a) and (b) following the purification process.

### Quantification the particle detachment

Comparative AFM imaging before and after the immersion process (Fig. 4.13) provides a detailed view of the cleaning effect. The AFM images were analyzed in a quantitative manner with a batch analysis script that segmented them and then separated the CNTs from spherical particles. Figure 4.14a shows analysis results for the detachment fractions of debris particles and nanotubes for a set of six samples and three different immersion velocities. Mean values for the detachment of irregular debris and MWNTs were $47\,\%$ and $10\,\%$, respectively. The framewise standard deviation values, shown for each samples for the debris data in Fig. 4.14a, quantify the extent of regional variation in the detachment; for carbon nanotubes, the number of detached species was insufficient for similar estimate to be relevant.

Although the size distribution of the particles was not analyzed in this study, it is still qualitatively clear based on AFM images (Fig. 4.13) that smaller particles, particularly those under $\sim 100\,\mathrm{nm}$ in diameter, tend to be retained more often than larger ones. This interpretation agrees with Figs. 4.11b and 4.12, where few micron-scale particles can be seen in the optical micrograph, but in the SEM image small debris can be seen among the CNTs. In comparison of the different immersion velocities, no apparent dependence was noted with respect to particle detachment on this velocity range in Fig. 4.14a.

The analysis shows that while the detachment process is highly selective in the favor of irregular debris, a significant portion of carbon nanotubes were also detached in the process. This estimate is subject to the limitations of our analysis, that may somewhat exaggerate their detachment. The classification of particles as debris or tubes in our segmentation routine depends on their shape, quantified in terms of aspect ratio, length of the long axis, surface area and orientation angle in this work. The two first ones are the key parameters in identifying CNTs. In particular, the long axis threshold value defined the minimum length of a carbon nanotube.

Here, our selected value for the long axis minimum threshold, which corresponds to a length of about $120\,\mathrm{nm}$; a very inclusive definition from application viewpoint where the interest generally lies on tubes with lengths in the micron scale. Given that such small tube fragments are far more frequent in the deposition than significant tubes, it is easy to see that they largely dominate the detachment statistics. Aside from them, a portion of detached CNTs consists of tubes accompanied by overlapping debris particles, or tubes entangled with one another. On the other hand, detachment of individual, neat CNTs appears to be rare.

We also considered the effect of the angular orientation of carbon nanotubes to their detachment from the surface. In this analysis, any MWNTs detached from the surface as a result of the immersion treatment were first manually identified, and their orientation angles then acquired from the AFM image depicting the initial deposition. Figure 4.14b shows the outcome of this analysis, with the fraction of horizontal carbon nanotubes, oriented parallel to the contact line, clearly elevated among all detached MWNTs.

The details of AFM imaging and the quantitative image analysis process will be the subject of chapter 6 in the thesis. Raman measurements, as well as results of the experiments on grooved substrates will be discussed later in the context of applications (chapter 7).

### 4.3.3 Discussion

The experiments and analysis reported in this paper demonstrate the application of mobile liquid interfaces as a practical method for improving the quality of spin coated, arc-discharge grown MWNT depositions in a simple, easily scalable arrangement. In general, up to half of all debris particles could be detached from the silicon surface with this method, while carbon nanotubes tend to be retained. The collateral damage suffered by MWNT appears to be largely limited to tubes that are either very short, contaminated by particulate debris, or entangled together with other tubes.

The orientation analysis of detached species is subject to the irregularity of the detached MWNTs, however a distinct orientational effect is still implied. Such selective detachment could give rise to the apparent re-orientation of species in statistical before / after analysis as implied in our previous work. Efforts to verify orientation-dependent effects on spin-coated CNT depositions are hampered by pre-existing radial orientation that results as a consequence of the spin coating process [75]. However, in our case this effect can be ruled out because the initial orientation distribution showed an abundance of vertical species instead (Fig. 4.14b, inset). This is in accordance with radial spincoat-induced orientation, because the experimental sites were located along the vertical mid-axis of the samples. Considering that the horizontal tubes were still clearly favored in the detachment, this makes for a rather robust result.

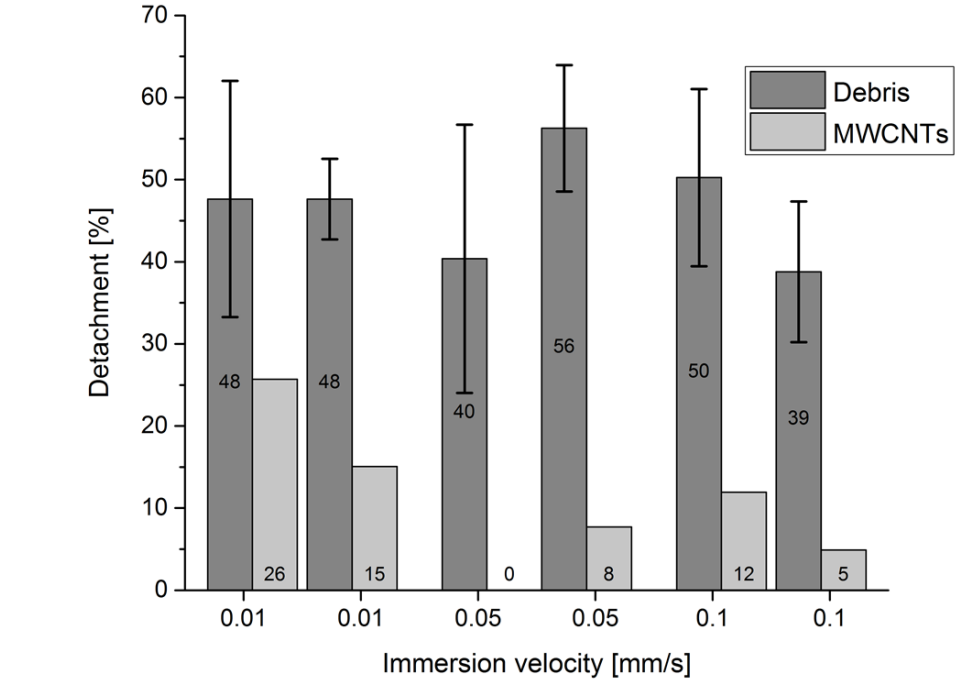


(A)

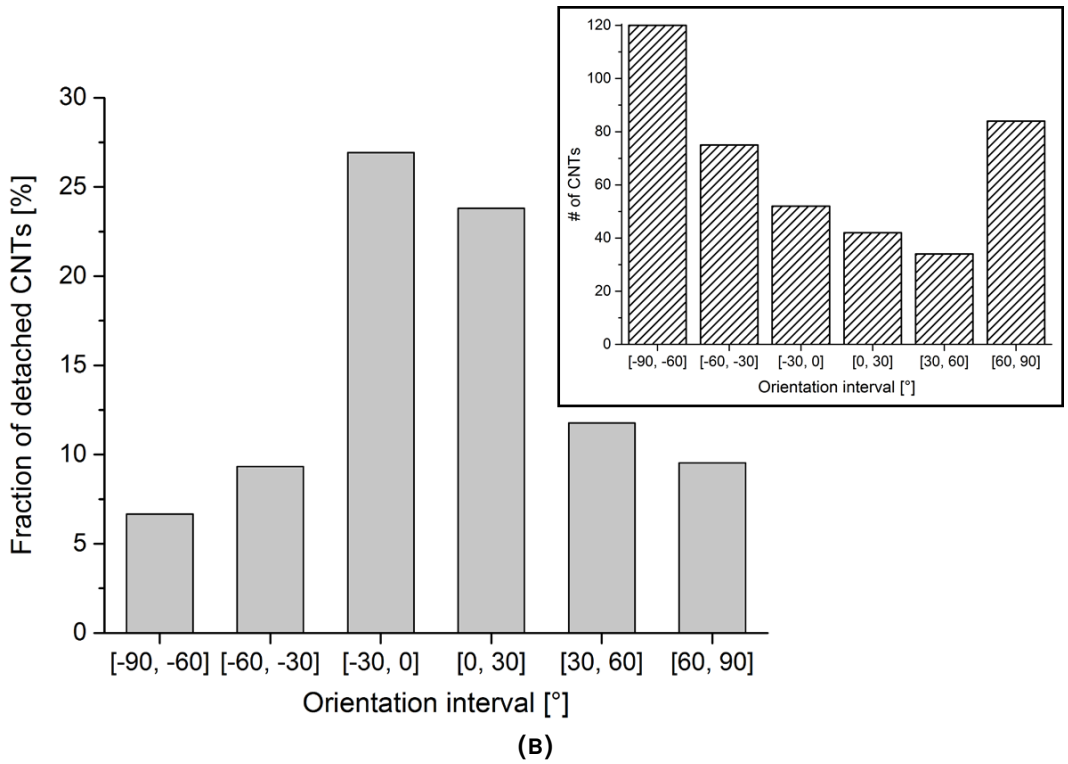


(B)

**FIGURE 4.14** (a) Graph showing the fraction of detachment vs. the immersion velocity for amorphous debris particles and MWNTs; the error bars indicate standard deviations computed framewise for debris. (b) Distribution of detached MWNTs with respect to their initial angular orientation. Inset shows a histogram for all tubes in the deposition.

Hydrophilic pre-treatment of the underlying substrate is of great importance for the efficiency and uniformity of the process, implying that the liquid-surface contact angle is of importance in its theoretical treatment. We were not able to find any clear dependence between the rate of particle detachment and the immersion velocity. This implies that the dynamic aspects of the process are unlikely to be important for our scenario, however this analysis is cursory given the limited number of samples.

We conclude that our technique provides a good alternative for improving the quality of MWNT depositions in a gentle manner that does not require nor induce modification of their chemical properties. Its main drawback is that it is naturally limited to the cleaning of on-chip depositions, and as such it is primarily useful for the end-user as *in-situ* cleaning method. Another shortcoming is that the cleaning effect is dependent on the interaction of the contact line with the hydrophilic sample surface; as such, we do not expect it to work in the context of CNT thin films where the entire substrate is covered by CNT material. It is however, in principle, very well scalable to large samples and surface areas for sufficiently "sparse" depositions.

## 4.4 Physico-chemical aspects of the cleaning process

In the third work [50], we present a more detailed investigation of the purification process in the context of our immersion cleaning technique, focusing particularly on the role of the chemical aspects in the process. For this purpose, a refined experimental protocol is introduced, where the overall cleaning effect is improved, and the quantitative results become more systematic than before. Additionally, results of purification experiments carried out on CVD-grown double-walled carbon nanotube (DWNT) material are also presented.

### 4.4.1 Evolution of the methodology

Since the publication of our original paper on the immersion cleaning of arc-discharge grown carbon nanotube depositions [49], we have significantly improved the experimental arrangement we have at hand. One of the dissatisfying features of the old approach was that it was necessary to pipette away the surface layers of the immersion liquid, which was non-systematic and could still result in imperfect removal of the suspended debris and subsequent redeposition. Also, any attempts to experiment on more complicated immersion fluids, such as ionic solutions, resulted in massive crystallization of chemical residuals onto the sample surfaces.

According to our interpretation of the immersion process, this type of redeposition takes place in the retraction phase as the sample is lifted from the container. Given the hydrophilic nature of the silicon substrate, a film of liquid generally adheres to the surface at this point. This layer also contains some of the debris that remained suspended on the liquid surface, and thus the redeposition probably takes

place as the film evaporates during and following the retraction. If the residual meniscus is weak, this happens rather quickly, and it will be hard to avoid the formation of the redeposit by e.g. flushing the meniscus with inert gas.

In order to fully avoid the formation of redeposits, it is necessary to ensure that no debris matter persists in the adhered layer of liquid at the retraction phase. This can be achieved if the container can be rinsed with clean liquid once the immersion has been completed. Figure 4.15a shows an illustration of such an arrangement we have realized, and Fig. 4.15b depicts the experimental protocol.

We now utilize a tubular immersion chamber which acts as a rinsing cell. There are two reservoirs, one for the immersion solution and another one containing containing pure water for the rinsing, both connected to a common inlet via branch tubing and control valves. Prior to the immersion, the outlet at the opposing end of the chamber is closed, and it is filled with the immersion liquid. The sample is then immersed into the liquid via a slot on top of the tube. Once the immersion has been completed, the sample is further lowered to the bottom of the chamber, and the inlet is opened to the rinsing reservoir simultaneously with the outlet. The chamber is then rinsed until all particulate matter is vacated from the chamber. The sample can then be retracted safely, without risking redeposition from the air-water interface.

Two diffusers (perforated plastic cylinders) were inserted near the ends of the tube to avoid disturbance from the inlets and outlets from affecting the central part of the chamber. In principle, this would allow us to carry out the immersion with a persistent flow established, but experience has shown that it is difficult to obtain a stable flow this way. However, even with immersion into stationary liquid with subsequent rinsing prior to sample recovery, we have been able to improve the extent of cleaning by a significant margin relative to our previously published experiments. Furthermore, this arrangement allows us to utilize chemically modified immersion fluids, and as such the effects of ionic strength and pH on the particle detachment can now be investigated.

There are also some drawbacks to the refined approach. Once the sample first touches the liquid during the immersion step, a momentary instability occurs at the interface due to appreciably greater volume of the liquid compared to the previous arrangement; in order to keep this from affecting the cleaning process, the vertical movement is halted for one minute, and then resumed at constant immersion velocity $v_{\mathrm{im}}$, to allow the disturbance to die out. Furthermore, while the viscous drag force has generally been negligible in our experiments, it may turn out rather powerful during the rinsing phase given the macroscopic dimensions of the flow tube. To this end, it is possible that also the drag force contributes to the cleaning effect. To minimize the effects of the flowing liquid, we carry out the experiments with the backside of the sample against the flow, as illustrated in Fig. 4.15b, to provide a degree of protection for the CNT deposition on the leeward face. Based on trials experiments, this also accommodates for the most systematic cleaning between individual samples.

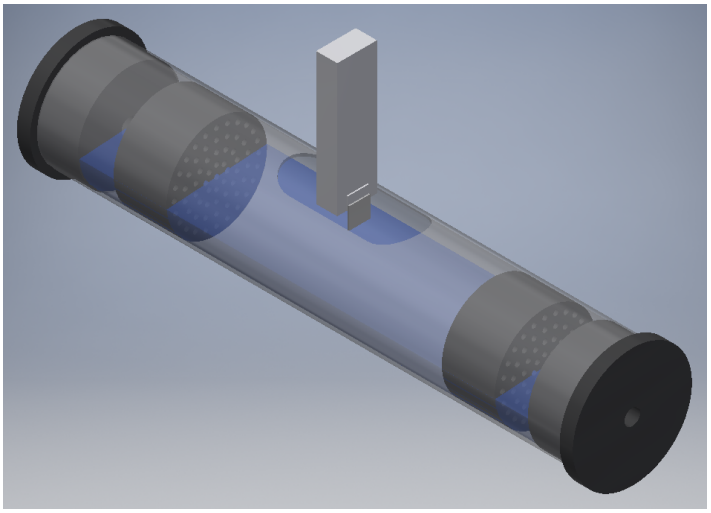

(A)

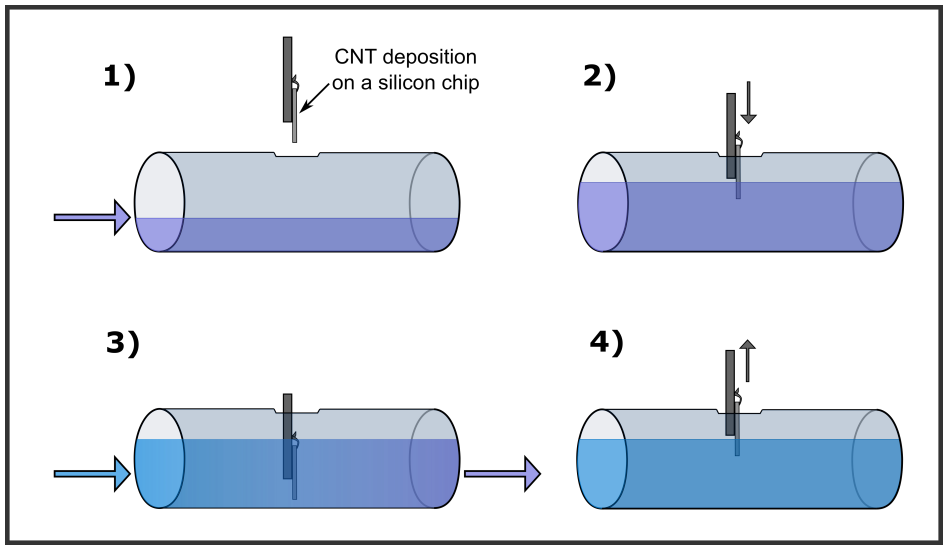


(B)

**FIGURE 4.15** (a) CAD-drawing of the immersion flow chamber. (b) Schematic of the refined experimental protocol: 1) the flow tube is filled with the immersion liquid; 2) the sample is first lowered until a contact is established with the liquid, and then immersed further into liquid after a stabilization period of one minute; 3) once the sample is completely submerged, the chamber is rinsed with clean water for a period of four minutes; 4) the sample is finally retracted and subsequently dried.

### 4.4.2 Experimental methods

Aside from the immersion arrangement, the experimental details are largely reminiscent of the previous work. The biggest difference is that microfabricated AFM reference marks are no longer utilized, due to the appreciably higher number of samples investigated in this study; the region to be imaged is merely marked with a diamond pen during the sample preparation. In addition, the AFM facilities available to us were upgraded, and we now utilize a Dimension Icon AFM system that allows us to record larger image frames with better image quality. In this work, $17\,\mu\mathrm{m} \times 17\,\mu\mathrm{m}$ image size was used, with only an individual frame recorded on each sample prior to and following the immersion treatment. This makes the analysis simpler, with no need to combine overlapping frames.

Three different immersion solutions were compared in our assay: millipore ultrapure water, $0.01\,\mathrm{M}$ hydrocloric acid (HCl) solution (pH = 2), and $1\,\mathrm{M}$ KCl solution. Experiments were done with three immersion velocities ($1$, $0.1$ and $0.01\,{}^{\mathrm{mm}}/_{\mathrm{s}}$). For every liquid, four samples were investigated per each immersion velocity. The elapsed time between the surface treatment and the immersion process varied from roughly two to six hours for different samples. This did not give rise any systematic difference in the particle detachment with other variables kept constant, indicating that the extent of surface chemistry decay is limited within this time frame.

In addition to the commercial, arc-discharge grown MWNTs, we also tested CVD-grown double-walled carbon nanotube (DWNT) material provided by Prof. Emmanuel Flahaut from CNRS Toulouse, France. The DWNT material had been washed in concentrated HCl solution after the synthesis in order to remove the metallic catalyst particles, but no further chemical purification was done; the powder was utilized as-received, with sample preparation similar to the AD-MWNT material. Given the considerably poorer dispersibility of the DWNT-material to 1,2-dicholoroethane, the stock solution however needed to be diluted several times, down to approx. $2\,{}^{\mu\mathrm{g}}/_{\mathrm{ml}}$, before acceptably uniform dispersion was attained.

### 4.4.3 Results

The effect of the refined immersion process is seen in Fig. 4.16, which shows a pair of AFM images recorded on a typical sample before and after the immersion to ultrapure water. We may note that compared to our previous work, the original deposition appears to be somewhat more densely populated, however particle detachment still remains highly efficient. Detachment of some CNTs can also be noted.

These observations are also supported by quantitative analysis results that are summarized in Fig. 4.17. Here, each bar corresponds to analysis results averaged over the set of four samples[4], while the error bars represent statistical standard deviations

[4]with the exception of the KCl series, where salt contamination was suspected as the cause of excessively low detachment fractions on two samples that were disregarded in the analysis.

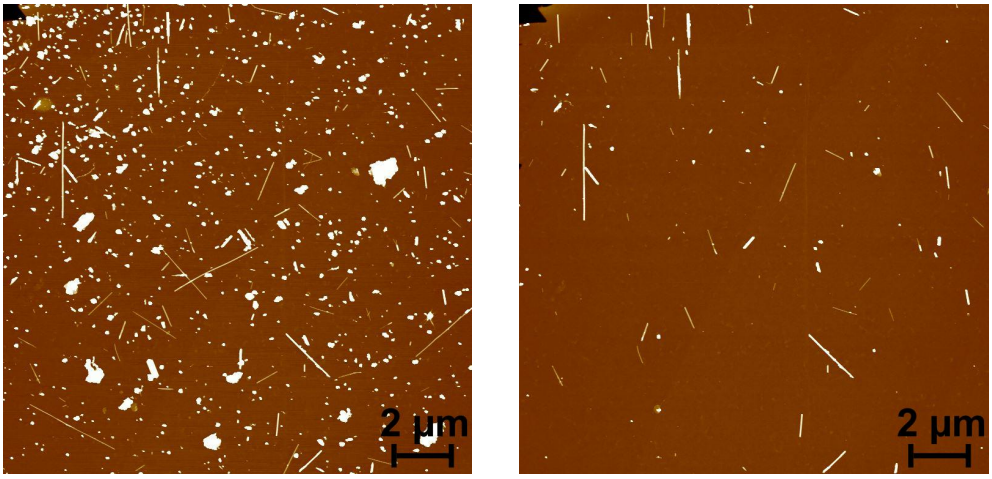


**FIGURE 4.16** (a) AFM image ($17 \times 17\ \mu m$) of a typical AD-MWNT deposition. (b) Same sample imaged following immersion in water.

for debris particles. We can see that regardless of the immersion liquid that was used, the detachment of ACP (amorphous carbon particle) debris has increased substantially, with peak values up to $90\,\%$ reached here compared to about $60\,\%$ in the previous work. In the meantime, the detachment of carbon nanotubes generally correlates with that of the debris particles, but remains well smaller, although it has, unfortunately, also increased. The standard deviations for CNT detachment grow generally larger than those of the debris particles.

Figure 4.17 also shows a comparison between the different immersion solutions and velocities. It is clearly demonstrated that the overall detachment fractions improve with reducing velocity of the interface regardless of the liquid. Comparing the different solutions, it is suggested that the best detachment is typically seen with the acidic immersion solution ($0.01\,\mathrm{M}$ HCl solution), while there is no apparent difference between the water and the $1\,\mathrm{M}$ KCl solution.

A before / after comparison of the experiment carried out on CVD-grown DWNT-material is presented in Fig. 4.18. As expected, the initial deposition is much cleaner in terms of irregular debris, compared to the AD-MWNT samples: only a few individual debris particles can be seen in Fig. 4.18a. Given their longer and more flexible nature, DWNTs also show a tendency to interconnect, even at low concentrations of the dispersion. Some bundles of DWNTs can also be seen, most likely due to limited dispersibility of the material without the use of surfactants or chemical functionalization.

In comparison, the behavior of the DWNT deposition in response to the immersion process (Fig. 4.18b) is qualitatively rather similar to the MWNT samples: the irregular debris particles are efficiently vacated from the surface, while a number of DWNTs are also lost. Although the extent of DWNT detachment is pronounced, it is

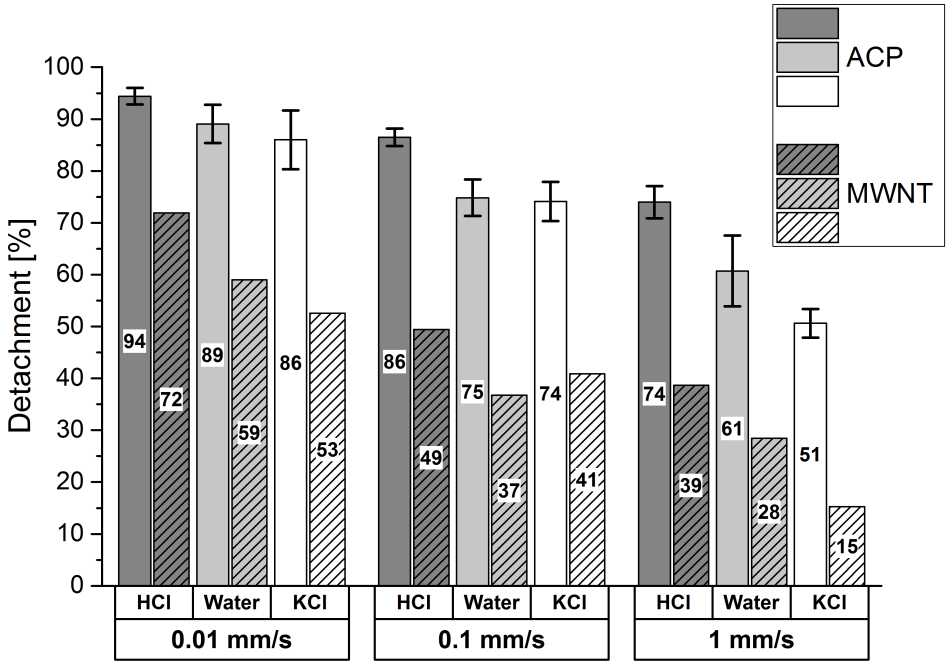


**FIGURE 4.17** Results of the refined immersion purification experiment summarized as a bar chart for ultrapure water, 1 M KCl solution and 0.01 M HCl solution (pH = 2) for three different immersion velocities. The detachment fractions for amorphous carbon particle (ACP) debris is reflected in the non-shaded bars, while shaded bars show the detachment of MWNTs.

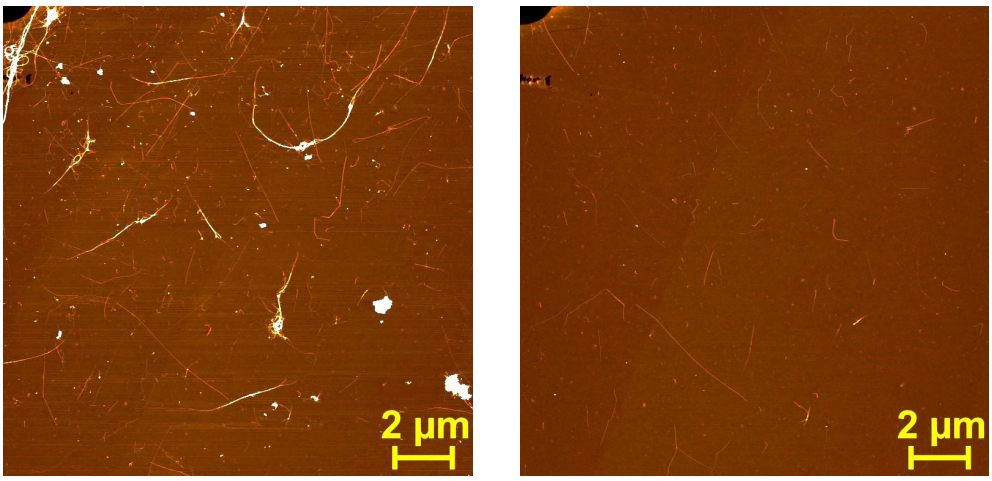


**FIGURE 4.18** (a) AFM image (17 × 17 µm) of a CVD-DWNT deposition. (b) Same sample imaged following immersion in water.

clear that some individual tubes are still retained. Additionally, DWNT-bundles have been also detached as well.

### 4.4.4 Discussion

Figure 4.19 shows dark-field optical micrographs of typical AD-MWNT samples before and following immersion in the different solutions. There are no signs of widespread redeposition nor apparent chemical residuals that plagued our previous trials with modified immersion liquids. The validity of the new immersion chamber concept has thus been confirmed. In order to avoid chemical residues or debris redeposition during the sample retraction, it must be ensured that no such contamination is present in the liquid meniscus that adheres to the hydrophilic surface during the recovery of the samples, and this is best achieved by copious rinsing of the flow chamber with clean water before the sample is retracted.

Some crystallization of salt could nevertheless still be witnessed on some of the post-immersion AFM images taken on the KCl samples, however these instances appear non-systematic in nature, and may have been due to precipitation during the immersion step in such a concentrated solution. As a general consequence of the salt contamination, the particle detachment may have been slightly underestimated in the KCl solution in Fig 4.17, although given the small size of these crystallites, they generally fall below the particle size cut-off in the analysis.

On two such samples, their presence was more dominant, and suspecting that the detachment fractions were artificially underestimated on these samples, they needed to be disregarded in the final analysis. If incorporated, the average detachment of debris particles falls somewhat with the $0.1\,{}^{\mathrm{mm}}/_{\mathrm{s}}$ and $1\,{}^{\mathrm{mm}}/_{\mathrm{s}}$ immersion velocities, but in the meantime the standard deviations also grow in proportion.

According to the statistics of Fig. 4.17, it is clear that the overall extent of detachment has improved significantly compared to our previous experiment. This can be attributed to various aspects of the refined experimental methodology. For one, the avoidance of redeposition in the flow chamber scheme allows for a cleaner result, but this is unlikely to explain the entire discrepancy. Another, more subtle difference is that in these experiments, no microfabricated reference marks were prepared on the substrates. Given the tendency of contact lines to pin onto fixed surface defects, the evaporated gold references may have had a strong local effect on the motion of the contact line in the vicinity of the experimental region in our previous work. The quality of the AFM images was now greatly enhanced compared to the existing work, which translates to a more deterministic analysis process.

The results presented in Fig. 4.17 highlight an interdependence between the immersion velocity and the detachment efficiency: the detachment of both particles and CNTs seems to improve as a function of decreasing velocity for each immersion liquid. Compared to our earlier work where no clear dependence could be seen, this result is more in line with studies on the detachment of spherical colloids, where a similar monotonic relationship has been frequently observed. The interpretation of the velocity dependence will be discussed in chapter 5, along with a review of the existing studies.

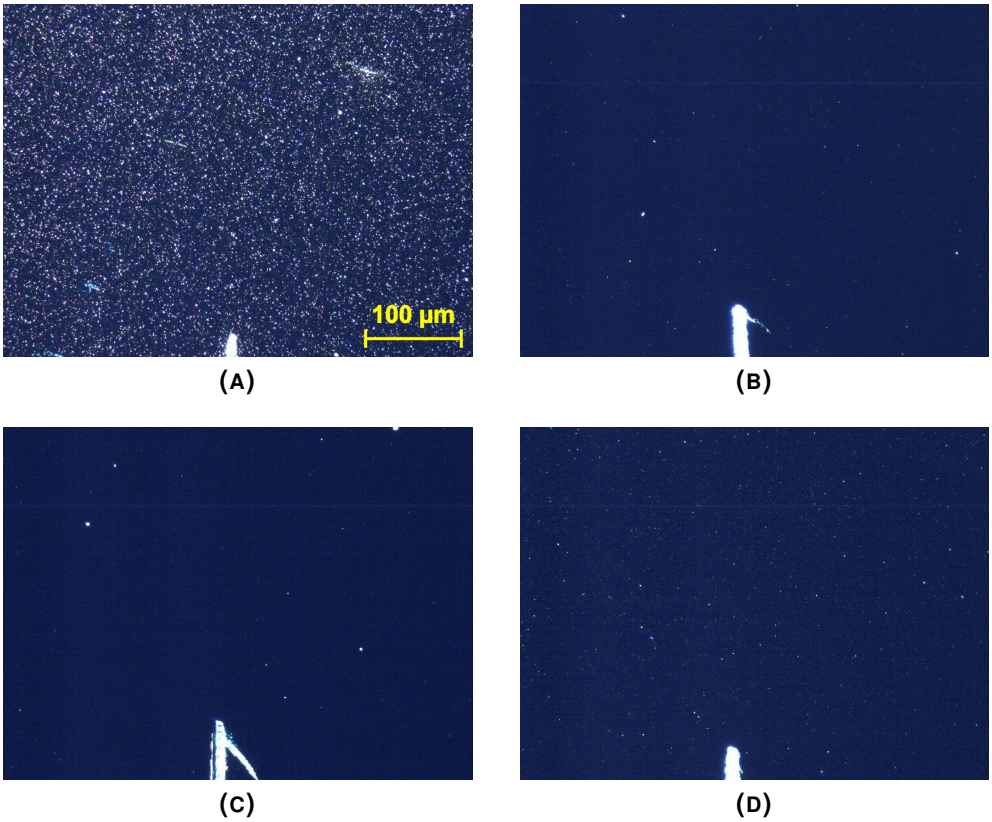


**FIGURE 4.19** Optical micrographs of the MWNT samples: (a) a typical freshly-prepared sample; (b) following immersion to plain water; (c) following immersion to 0.01 M HCl solution; (d) following immersion to 1 M KCl solution.

The emergence of the dependence in this experiment can also be credited to the refined experimental methodology, quite possibly to the lack of a reference structure. In the previous work, these structures pre-fabricated from Au may have affected the motion of the contact line. If any interaction exists between the references and the contact line, their role on its progression easily becomes dominant in the immediate vicinity (e.g. repeated pinning and subsequent snapping-off at each row of the reference marks), and the velocity of the macroscopic interface is thus obscured. The same factor may also explain the quantitative differences in the results of this work and our previous study: the detachment statistics shown in Fig. 4.17 are far more systematic now, and particularly the standard deviation values for particle detachment are remarkably small.

The standard deviation values of CNT detachment are on the other hand much larger, similar to the framewise statistics in the previous study. It appears the the detachment of CNTs is far less systematic than that of the irregular debris, and given that their fraction is far from insignificant in this study, this observation requires some further thought. The main reason is likely that the number of CNTs on the surface remains much lower than that of the debris particle, so the total number of

the detachment events is still very limited on a given sample. As a result, relatively small differences in the absolute number of detached tubes may give rise to large standard deviation in the detachment statistics.

In the trials with CVD-DWNT nanotubes, we were able to achieve a qualitatively normal cleaning effect, verifying that the process is not critically dependent on the type of the CNT material. However, the extent of DWNT detachment was unexpected, given their thin profile that should result in appreciably weaker interaction with the liquid interface compared to the AD-MWNTs. Furthermore, the specific surface adhesion of the DWNTs should also benefit from their length. In the post-immersion AFM frame, Fig. 4.18b, some individual DWNTs are however retained, and in the pre-immersion data they can be identified as ones that do not overlap or interconnect with other tubes.

It is therefore suggested that the detachment of DWNTs depends strongly on their interconnectedness; individual tubes that have a lot of contact area directly with the substrate have a better chance to be retained, while DWNTs that belong to strongly connected networks are frequently detached. Compared to MWNTs, double-walled tubes form more densely connected depositions, and hence it can be understood that they tend detach collectively. This is also demonstrated by the efficient removal of DWNT bundles on our samples: whenever deposited in interconnected way, either as bundled ropes due to limited dispersiblity, or individual tubes overlapping by chance, the detachment of the CNTs is enhanced by mutual cohesive interactions, and any individual CNT that releases has a chance to detach a substantial portion of the entire network. Given the shorter average length and weaker mutual interactions inherent to multi-walled tubes, the same effect is less pronounced on our AD-MWNT samples.

One could envision utilizing this effect as means of thinning out dense, overlapping CNT depositions in a controlled way, at least for single and few-walled tubes. It can be postulated that the efficacy of the technique depends on the degree of surface coverage: at the limit of a bulk CNT thin film, where the entire surface is covered and the liquid interface may no longer interact with the underlying hydrophilic substrate, the interface forces will change radically and the process is expected to become ineffective.

The interpretation of the results acquired by varying the composition of the immersion liquid will be discussed as a part of the nanoparticle adhesion in the following chapter.

# Chapter 5

# Particle-level picture of the detachment process

In this chapter, we shall focus on the theoretical treatment of the purification process of CNT depositions as demonstrated in our experiments. We adopt the approach from existing experimental works for spherical micron-scale particles, where an established model has been developed; some of these works will be reviewed in the process.

Colloid detachment from smooth, particularly silicon, substrates emerged as an independent research topic during the 1980s with the continuing development of the semiconductor industry. Given the rapid advance of the lithographic patterning techniques, the quality and cleanliness of the source material became a prime concern. In particular, detachment of submicron particles could not be carried out in a systematic manner [74], and even contemporary techniques have their limitations and challenges [120]. The root of the problem lies in the fact that in most methods of detachment, the detachment force depends on the volume or cross-section of the particle, giving rise to second or third-order dependence on particle radius while the adhesive van der Waals force is directly proportional to the radius of a spherical particle. Hence, such cleaning techniques tend to become inefficient as the particle dimensions are scaled below submicron threshold.

As we will see in the following, the surface tension force exerted onto a colloidal particle by mobile liquid interface also scales linearly with the particle dimensions, similar to the van der Waals force. The detachment efficiency is then expected to be independent of the particle size, which should be appreciated as a major advantage of the process as a cleansing technique.

With only these two forces opposing one another in static manner, the release of colloids from the substrate can be understood in simple terms. But as we find out, this might not be the whole story because particularly strong viscous forces may arise to further hinder the detachment process. Exact theoretical treatment of the process is challenging, owing mainly to the ambiguity related to the contact angles and the

general difficulty of exact mathematical description of mobile liquid contact lines. Even in the simplest geometries, further approximations are required. In addition, we will find that besides the surface tension force, an additional force contribution appears due to the local pinning of the contact line when the macroscopic interface advances beyond a stationary particle.

## 5.1 Static view of the purification process

The original, and as far as I can tell, the most complete description of a mobile liquid interface interacting with colloidal particles up to date, was given by A.F.M. Leenaars and S.B.G. O'Brien in their pioneering work reported in 1989. They were motivated by an observation made earlier by Visser [118], who in his 1973 Thesis work commented on the enhanced detachment of submicron carbon particles from substrate disks rotating in water in case they made contact with air bubbles. This was initially discussed in terms of the surface tension forces at the contact line by Leenaars in 1988, supported by experiments that demonstrated practical cleaning of various non-wetting particulate contaminants from silicon surfaces [73].

These experiments also implied that the detachment ceased when the liquid interface passed over the substrate at sufficiently high velocity. Furthermore, when completely wetting hydroxylated silica particles were introduced on the surface, no particles were removed. However, when the substrates deposited with these particles were treated under the vapor of a silane compound to increase their contact angle up to 76°, the detachment was partially restored.

To explain these findings, both static and dynamic pictures of the process were discussed. The simple static model, which is the starting point for analysis in virtually every paper dealing with retention and detachment of colloids from surfaces in response to mobile liquid interfaces, was found to be insufficient in explaining all the experimental results, namely the lack of detachment at sufficiently high boundary velocities. In this respect, only the complex dynamical derivation brought about a satisfactory outcome.

In the following, I introduce Leenaars' "static" model of the liquid-particle interfacial interaction as it has been established in the subsequent works for spherical colloids. Aside the surface tension force that is attributed as the primary cause of particle detachment in most of these works, the elastic shear force due to local pinning of the contact line is considered. This is followed by brief discussion on the adhesion of nanoparticles, and then the hydrophobic interactions, which do not appear to have been previously discussed in this context, but may play a crucial role in our experiments. I will then provide qualitative estimates of the magnitudes of these forces for carbon nanotubes and debris particles, and discuss the implications of these estimates on the key results of our experiments.

Following the theoretical treatment, I review a number of other works dealing

with the detachment and retention of colloidal particles from surfaces, and evaluate our results against them. I will then address the shortcomings of the simple model as pointed out by Leenaars & O'Brien, and review their suggested solution to the problem. Finally, the discussion will be summarized in evaluation of our work against the existing studies. The limitations of these considerations in our experimental context will also be discussed.

### 5.1.1 Interfacial forces: surface tension

Our immediate goal is to interpret the key results of our investigations [49–51] in terms of the simple framework originally presented in the works by Leenaars & O'Brien [73,74]. This static approach to the colloid-level picture of the detachment has since been adopted by virtually all subsequent works. It is generally found sufficient in explaining the detachment of colloidal particles from smooth surfaces due to their interaction with passing liquid interfaces so as long the velocity of the liquid interface is not too high.

Leenaars' original derivation starts from a simplified view of the interface-colloid interaction, fig. 5.1a: a spherical colloid with radius $R$ is surrounded by liquid whose level rises axisymmetrically around the particle. In this case, the effect of the substrate on the interface is practically eliminated; the picture equals that of particle floating at a liquid-gas interface, save for the adhesive force that anchors the particle onto the surface.

The fill angle $\phi$ characterizes the angular extent of the wetting as measured from the center of the particle. The length of the liquid-gas interface is $l_\mathrm{i} = 2\pi R \sin\phi$, and multiplied by $\gamma$ this gives the total surface tension force. The liquid-colloid contact angle $\theta$ determines the direction of the surface tension force. In order to work out the vertical component of the force, we note that the angle $\beta = 270^\circ - (180^\circ - \phi) - \theta = 90^\circ - (\theta - \phi)$. Then the expression for the fraction of the surface tension force that is effective in detaching particles from surfaces is

$$F_\gamma^z = -2\pi R\gamma \sin\phi \cos(90^\circ - (\theta - \phi)) = 2\pi R\gamma \sin\phi \sin(\theta - \phi), \tag{5.1}$$

where the identity $\cos(90^\circ - x) = \sin x$ was used [104]. The relevant value for colloid removal is the maximum of $F_\gamma$, which we can find by differentiation with respect to the free parameter $\phi$. One finds that the peak value is reached with $\phi = \theta/2$:

$$F_{\gamma,\,\mathrm{max}}^z = 2\pi R\gamma \sin(\theta/2)^2, \tag{5.2}$$

It is useful to note the role of the geometric factor in $F_\gamma^z$, $l_\mathrm{i} = 2\pi R \sin\phi$, associated with the length of the liquid-colloid contact interface. It must thus be modified for non-spherical shapes.

To describe a more realistic case with the liquid interface propagating along a

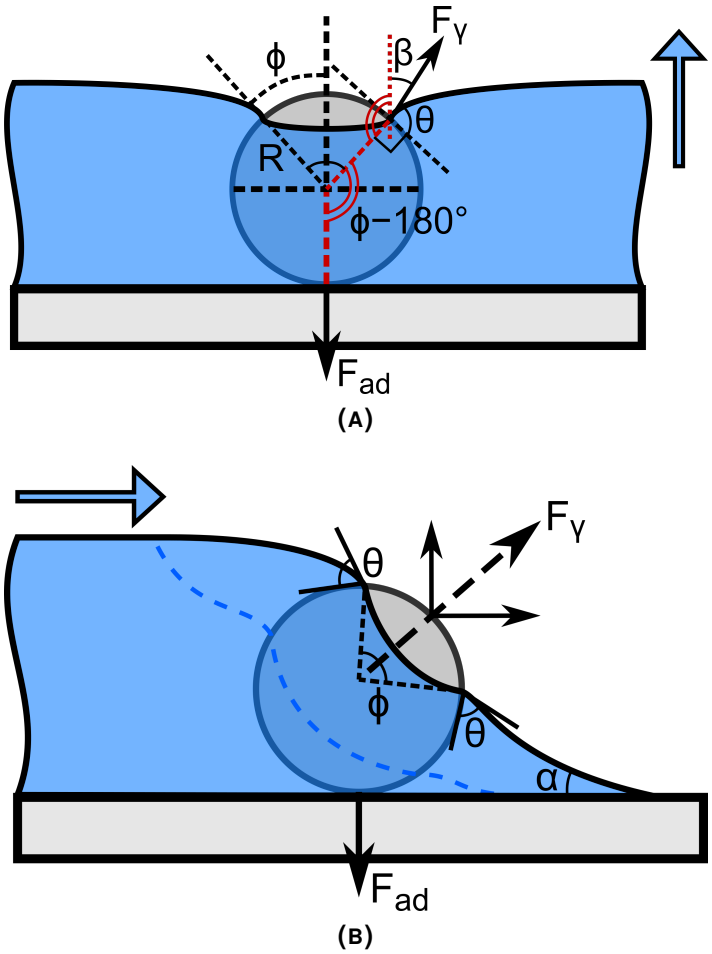


**FIGURE 5.1** (a) The geometrical construction utilized by Leenaars in the derivation of expression for the surface tension force; a vertically rising, axisymmetric interface interacting with a spherical colloid. The angles indicated in red are equal. (b) A more realistic scenario, with a laterally propagating meniscus interacting with a colloidal particle in the presence of a substrate. The dashed blue line depicts the shape of the meniscus at an earlier moment.

sample surface (Fig. 5.1b), it is argued that one merely needs to take into account that the liquid contact line must bind to the substrate at the non-wetted side of the interface with substrate-liquid contact angle $\alpha$. In the context of our experiments, $\alpha$ signifies the advancing contact angle as imbibition (immersion phase) is likely the dominant process over drainage (retraction phase) as discussed previously. Finite $\alpha$ does not have an effect on the magnitude of the $F_\gamma$, but instead tilts it further. Therefore, the maximum vertical component of the surface tension force becomes [4,73]

$$F^z_{\gamma,\,\max} = 2\pi R\gamma \sin^2\left(\frac{\theta}{2}\right)\cos\alpha \tag{5.3}$$

This applies for $\alpha < 90°$. A given colloid is thought to detach from the surface if the maximum detachment force $F^z_{\gamma,\,\max}$ overcomes its adhesion; otherwise, the colloid

is retained[1]. In this static picture, the velocity of liquid contact line relative to the stationary particle plays no direct role in the force balance.

### 5.1.2 Interfacial forces: elastic shear

The previous description of the imbibition process does not take into account the fact that the presence of the colloidal particle also locally inhibits the free motion of the liquid interface, causing a deformation in its profile. If the colloid is strongly adhered to the surface, the interface is held back in its immediate locale (Fig. 5.2). This tension gives rise an additional elastic shear contribution to the vertical interfacial force experienced by the colloid. It was first described by Joanny & de Gennes in 1984 in their work regarding to contact angle hysteresis [64], and depends strongly on the substrate-liquid contact angle $\alpha$:

$$F_{\mathrm{e}} = k \cdot x \approx \frac{\pi\gamma\alpha^2}{\log {}^{L}\!/_{a}} \cdot x \tag{5.4}$$

Here, $x$ is the extent of contact line deformation, and $a$ the characteristic size of the defect, i.e. $2R$ for spherical particles. The parameter $L$ is a macroscopic cut-off distance; the equation is in fact strictly correct for a single-defect case only. For a many-defect problem, it was pointed out by Joanny & de Gennes that $L$ should be replaced by the average distance between the defects $b$ [64].

The role of this elastic contribution has oftentimes been ignored in the context of colloid detachment from smooth surfaces due to a mobile three-phase contact line. In practice, it may enhance the detachment to the surface tension in cases where the liquid interface is locally pinned by the colloid. However, given that the shear force only acts along the direction of the substrate, it is unlikely to give rise to significant depopulation of the surface particles in itself.

As the macroscopic contact line progresses beyond a fixed particle, the elastic force $F_{\mathrm{e}}$ grows until either the particle is detached or the pinning film ruptures, snapping the interface back to its native, undisturbed profile while leaving the particle behind. The peak force prior to film rupture critically depends on the shape of the particle. Particles with surface roughness or jagged edges and beveled shapes allow for most prolonged pinning, as demonstrated by Chatterjee & Flury [20]. Theoretically, the pinning process manifests as continuous increase of the local colloid-liquid contact angle, with a maximum value which is expressed by the Gibbs' inequality condition:

$$\theta_0 < \theta < 180^\circ - \Theta + \theta_0 \tag{5.5}$$

The dynamic equilibrium contact angle $\theta$ may thus grow up to a maximum value

[1] It should be noted that a lateral component $F_{\gamma}^{xy}$, speculated to contribute to translocation of particles along the sample surface, also exists to the surface tension force, but its maximum is logically dependent on $\sin\alpha$ instead, and should thus disappear on a hydrophilic surface relevant to our case.

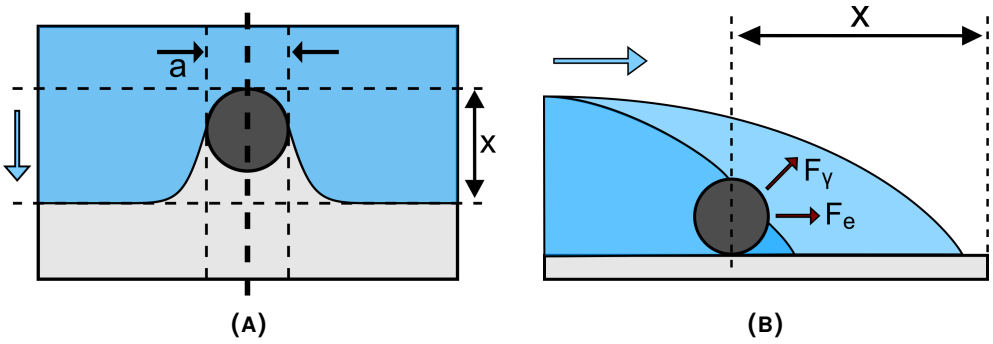


**FIGURE 5.2** (a) Top-view of an advancing contact line pinning onto a single defect with characteristic size $a$. The deformation of the contact line by $x$ gives rise an elastic shear force $F_\gamma$. (b) Side-view intersection along the bold dashed line in Fig. (a); the relative directions of $F_e$ and the surface tension force $F_\gamma$ are indicated. The light-blue color indicates the undisturbed profile of the meniscus behind the particle. The blue arrows show the direction of contact line progression.

defined by the native equilibrium colloid-liquid contact angle $\theta_0$ and the geometric wedge angle $\Theta$, which characterizes the pinning geometry [108].

The elastic contribution to the detachment force may be of importance in our case, as the irregular carbon debris particles are likely to exhibit severely textured surfaces that allow strong pinning of the passing interface. Flat, thin carbon nanotubes, on the other hand, are far less likely to serve as strong pinning sites.

### 5.1.3 Adhesion forces

Despite thorough investigative efforts, adhesion of fine particles onto planar substrates remains an active field of contemporary science, driven by the commercial interests associated with various industrial processes where it plays a fundamental role.

In electrically and chemically inert environments relevant to our case, Coulombic and chemical (acid-base) interactions can be mostly disregarded. The remaining adhesion mechanisms involve van der Waals molecular interactions and capillary adhesion. For a sphere (radius $R$) and a cylinder (length $L$, thickness $D$) on smooth, planar surface, the van der Waals attraction (Fig. 5.3), as per Ranade [96], can be written as

$$F_{\mathrm{ad}} = \frac{A_{132} R}{6H^2} \tag{5.6}$$

$$\frac{F_{\mathrm{ad}}}{L} = \frac{A_{132} D^{1/2}}{16H^{5/2}} \tag{5.7}$$

where $A_{132}$ is the composite Hamaker constant of the system, and $H$ is the equilibrium separation between the body and the surface that in the traditional picture of adhesion

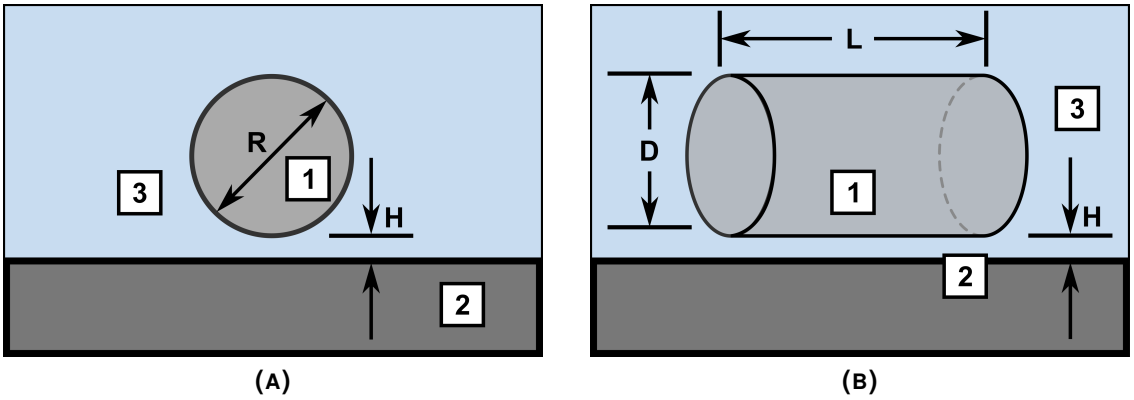


**FIGURE 5.3** Van der Waals molecular adhesion for (a) a sphere, radius $R$ and (b) a solid cylinder (diameter $d$, length $L$) in the vicinity of a substrate surface. $H$ indicates the separation distance from the substrate surface. Numbers '1', '2' and '3' indicate the material of the particle, the substrate and the medium, respectively.

theory is always finite. While the composite Hamaker constant can be tabulated, the separation distance cannot be determined exactly for a practical system due to the atomic discretenesss, and estimates of $H$ used in models thus vary in the scale of angstroms depending on the context.

This makes the equations rather impractical for precise numerical estimates, however qualitative remarks can still be made. For a sphere, $F_{\mathrm{ad}}$ is proportional to the its diameter, whereas for a cylinder, it is proportional to its length, but only to the square-root of its diameter. It follows that on a smooth substrate, the high aspect ratio intrinsic to carbon nanotubes guarantees their better adhesion to the surface surface relative to a spherical particle of equal diameter.

In case a liquid film is applied over the sample surface, one expects to see adhesion of the nanoparticles to weaken. For van der Waals attraction, the effect of the environment factors in via the Hamaker constant $A_{132}$, which is built up from the constants of three involved materials $A_1$ (the solid body), $A_2$ (the substrate) and $A_3$ (the surrounding medium): $A_{132} = A_{12} + A_3 - A_{13} - A_{23}$, where the composite constants are represented as $A_{\mathrm{ij}} = \sqrt{A_{\mathrm{i}} \cdot A_{\mathrm{j}}}$.

The material-specific Hamaker constants are related to the imaginary parts of their dielectric constants $\epsilon_{\mathrm{i}}$, and the relationship is such that $\epsilon_3 > 1$ will significantly weaken the interaction [58]. As a result, introducing a liquid medium, instead of vacuum or air, reduces the value of the composite constant $A_{132}$. Qualitatively, the interaction is weakened in liquid medium because the molecular electric fields that give rise to the vdW interaction induce reactionary fields in the surrounding medium that tend to screen the primary field. The net interaction then depends on the relative polarizabilities of the materials in question.

In practice, the magnitude of the van der Waals interaction is retarded due to finite time of electrostatic propagation between the solid bodies. The extent of this

retardation depends on the separation distance $H$, and it can be taken into account through the means of a correction factor that limits eq. 5.6. In works dealing with detachment and retention of spherical microcolloids [106], the following expression has been utilized for the van der Waals interaction energy $\Delta G_{\mathrm{vdw}}$:

$$\Delta G_{\mathrm{vdw}} = -\frac{AR}{6H}\left[1 - \frac{bH}{\lambda_0}\ln\left(1 + \frac{\lambda_0}{bH}\right)\right], \tag{5.8}$$

where $\lambda_0 \sim 100\,\mathrm{nm}$ is a characteristic length and $b \approx 5.32$ a dimensionless constant as introduced by Gregory [42]. It was argued that the expression is most precise for $H \ll R$, however in the opposite case the vdW-interaction quickly becomes insignificant for most purposes.

In a liquid electrolyte medium, van der Waals adhesion is furthermore weakened due to the presence of the ionic double layer that builds up around the colloid from the counterions residing in the liquid, and screens the native interaction. This can be accounted for by a separate energy term $\Delta G_{\mathrm{el}}$. For an electrolyte that only contains one species of ions with valance $z$, it can be formulated

$$\Delta G_{\mathrm{el}} = 64\pi\epsilon R\left(\frac{kT}{ze}\right)^2 \times \left[\tanh\left(\frac{ze\psi_{\mathrm{col}}}{4kT}\right)\right]\left[\tanh\left(\frac{ze\psi_{\mathrm{sub}}}{4kT}\right)\right]\exp(-\kappa H), \tag{5.9}$$

where $\epsilon$ is the dialectric permittivity of the medium, $k$ the Boltzmann constant, $T$ the absolute temperature and $e$ the elementary charge [106]. $\psi_{\mathrm{col}}$ and $\psi_{\mathrm{sub}}$ represent the surface potentials for the colloid and the substrate, respectively; these are generally unknown, and must be taken as their $\zeta$-potentials instead, that can calculated via e.g. electrophoretic mobility measurements. This is, however, inaccurate, with the true surface potentials generally higher than the respective $\zeta$-potentials. Finally, $\kappa$ is the inverse of the Debye-Hückel length,

$$\kappa = ze\sqrt{\frac{n}{\epsilon kT}},$$

where $n$ designates the number concentration of the ions in the electrolyte solution. Here, $I = \frac{1}{2}nz^2$ can be termed the ionic strength of the species.

From the previous equations, the total adhesion force can then be computed:

$$F_{\mathrm{DLVO}} = \frac{d}{dH}(\Delta G_{\mathrm{vdw}} + \Delta G_{\mathrm{el}}) \tag{5.10}$$

This is regarded as the so-called DLVO-theory, after Boris Derjaguin and Lev Landau, Evert Verwey and Theodoor Overbeek, applied to colloid adhesion on surfaces.

Given that the DLVO-theory is directly concerned with effects of the chemical composition to colloid adhesion in liquid medium, let us now discuss the experiments of our last paper [50] in this context. From eq. 5.9, we can directly see how the ionic

strength of the liquid factors into the adhesion: the greater the salt concentration $n$, the shorter the Debye length $\kappa^{-1}$, and weaker the double layer becomes. This results to weakening of the electrostatic screening repulsion, while attraction in accordance to eq. 5.8 begins to dominate. Hence, the particles are expected to adhere more strongly in a highly ionic environment.

In our experiment with $1\,\mathrm{M}$ KCl solution, the ionic strength of the liquid is so high that the screening repulsion should become entirely suppressed, eliminating the energy barrier between the primary and secondary minima in the DLVO adhesion curve (eq. 5.10 computed as a function of $H$) [11]. In the studies of CNTs in bulk liquid environments, a radical increase is seen in the retention of tubes on the sample surface relative to pure water, already with much weaker ionic strengths [123,124]. Our experiment displays virtually no effect in a highly ionic conditions, although the quantitative analysis is complicated by the tendency of the salt to precipitate on the samples despite the precautions. This implies that the double-layer screening effect in accordance to the DLVO theory is not very central to our scenario of nanoparticles being abducted to the liquid interface.

It should be pointed out that there are also differences in the physical composition of the immersion liquid relative to pure water: For $1\,\mathrm{M}$ KCl, the surface tension $\gamma$ increases by about $3\,\%$ [3], while the viscosity $\mu$ decreases by roughly $11\,\%$ [130]. The latter difference is significant only for the upcoming dynamic model of the particle detachment. The modest increase of $\gamma$ is on the other hand probably negligible, given that the exact surface tension in our experiment is likely determined by local environmental factors (e.g. spontaneous contamination of the solution under ambient air) that may induce far greater discrepancy, showing as sample-to-sample variations in our results. In either case, both of these factors are expected to improve particle detachment, and may hence somewhat downplay the chemical effects promoting retention.

The effect of acidity on the DLVO adhesion is more subtle. Changing the pH of the liquid primarily affects its ability to dissociate chemical groups and molecules bound on the surface of the substrate and the colloidal particle, which changes the electrostatic term $\Delta G_{\mathrm{el}}$ via the surface potentials $\psi_{\mathrm{col}}$ and $\psi_{\mathrm{sub}}$. The effect of pH on the retention of CNTs was also studied experimentally in one of the previous works, with systematic reduction of detachment in acidic environment [123]. In our case, opposing behavior is witnessed: detachment due to the mobile liquid interface is enhanced slightly, even though the pH of our solution was even lower. This may relate to the chemically native state of our CNT material, which is in contrast with the existing bulk liquid studies where oxidized, water-soluble CNTs needed to be utilized [123,124]. Furthermore, the surface chemistry of the substrate is also different in our works. These factors also affect the $\psi_{\mathrm{col}}$ and $\psi_{\mathrm{sub}}$, and may thus help to explain the discrepancies with our results.

### 5.1.4 Hydration forces

Surface chemical effects may also be a source of direct interactions between solid bodies in aqueous environments. When two bodies of hydrophobic surface character are in close proximity, it is energetically favorable for them to come together, in order to eliminate the unfavorable liquid-solid contact. In this case, a remote attractive interaction is mediated by the bulk liquid.

This is a simple picture of the so-called hydrophobic interaction, an ubiquitous concept that has been subject to increased experimental curiosity starting from the 80s through the use of AFM-based techniques and surface-force apparatus. Theoretical formulations of the interactions are still very novel and unestablished, and the fundamental, physical interaction mechanism remains far from settled; entropic effects may be the most likely candidate. Hydrogen bonding of water molecules plays a key role in the process.

What makes the previous, simplified picture interesting is that it is easily complemented by the opposite scenario. Hydrophilic surfaces conversely prefer to remain separated in water, and thus a repulsive interaction is realized. Experimental evidence suggests that both interactions exhibit similar character: exponential decay in magnitude with increasing separation, effective range of less than $20\,\mathrm{nm}$, and a similar characteristic decay length. It is then natural to argue that these phenomena should have an unified description. Such a general interaction potential was achieved in a recent, joint article [29]:

$$W_{\mathrm{H}} = 2\gamma_{\mathrm{i}} H_{\mathrm{y}} \exp\left({}^{-H}/_{H_0}\right) \tag{5.11}$$

In this expression, $H$ stands for the separation distance between two flat plates, and $H_0 \sim 1\,\mathrm{nm}$ is the decay length. The interfacial tension, $\gamma_{\mathrm{i}}$, is generally not the surface tension of the bulk liquid. The generic value of $\sim 50\,{}^{\mathrm{mJ}}/_{\mathrm{m}^2}$ was suggested in [29] for the hydrophobic case. $H_{\mathrm{y}}$ is so-called Hydra parameter, which quantifies the effective fraction of hydrophobic area at the interface. For a fully hydrophobic case, $H_{\mathrm{y}} = 1$, but for a hydrophilic surface, $H_{\mathrm{y}}$ becomes negative.

Equation 5.11 gives the interaction potential per unit area. It was shown in the work that this expression can be utilized to describe both hydrophilic and hydrophobic interaction, which can thus be commonly termed as hydration forces.

For the hydrophobic case, the attraction can be particularly strong, beating DLVO adhesion both in terms of magnitude and range. The repulsive, hydrophilic interaction is, on the other hand, somewhat weaker, and decays faster with $H$, although it still remains significant.

### 5.1.5 Force estimates for carbon nanoparticles

Let us now estimate the magnitude of the detachment forces for carbon-based debris particles and carbon nanotubes on our depositions. All figures presented here are order-of-magnitude estimates only; for this purpose, debris particles are treated as spheres, with radii commonly ranging from $10\,\mathrm{nm}$ to $1\,\mu\mathrm{m}$. The contact angle $\theta$ between water and the nanoparticle is not accessible; here, we estimate it as $\theta \approx 90°$, i.e. that of sessile droplet on graphite [95,107].

Inserting $\gamma \approx 72.86\,{}^{\mathrm{mN}}/_{\mathrm{m}}$ for water at room temperature and $\alpha \approx 0°$ for hydrophilic Si, we acquire from eq. 5.3 that $F^{z}_{\gamma,\,\mathrm{max}} \approx 0.23\,{}^{\mathrm{N}}/_{\mathrm{m}} \cdot R$, whereas $F^{x,\,y}_{\gamma,\,\mathrm{max}}$ vanishes. We can thus see that the magnitude of the surface tension detachment force is in the order of a few nN for a $10\,\mathrm{nm}$ particle, and grows linearly with $R$. Furthermore, the force acts almost purely in the vertical direction.

For carbon nanotubes, we may attempt to adapt the eqs. 5.3 & 5.4 by replacing the appropriate geometric factors describing spherical geometry with those that establish a tubular case. Given the difficulty of stringent theoretical treatment of the particle/interface interaction even in the ideal, spherical case, simple geometric arguments have been used in the previous works dealing with the effects of colloid shape on their retention and detachment [4]. CNTs however arguably constitute an extreme case due to their small dimensions and high aspect ratio. Particularly when it comes to $F^{z}_{\gamma}$, it is difficult to affirm that the geometric construction behind eq. 5.3 remains valid.

In eq. 5.3, $l_{\mathrm{i}} = 2\pi R \sin({}^{\theta}/_{2})$ represents the length of the interface line for the surface tension force maximum $\phi = {}^{\theta}/_{2}$, and it remains valid for a CNT that is oriented perpendicular to the liquid interface. But for a CNT that is oriented parallel, the length of the interface line becomes $l_{\mathrm{i}} \sim L$ the length of the tube. For a typical multi-walled CNT with diameter of $10\,\mathrm{nm}$ and length of $1\,\mu\mathrm{m}$, $l_{\mathrm{i}}$ could thus be up to 100 times longer for parallel case compared the perpendicular one. Therefore, $F^{z}_{\gamma}$ ought to be strongly dependent on the orientation of the CNT, with much stronger detachment force for the parallel orientation.

In addition to the surface tension, there is the elastic shear contribution in accordance to eq. 5.4. On hydrophilic surface, we expect it to small, but finite. Furthermore, considering that $a$ characterizes the lateral extent of the defect with respect to the interface, and it is affected by the orientation of the tube. $F_{\mathrm{e}}$ would thus also be greater for the parallel orientation given the same extension $x$.

Given the linear dependence of eq. 5.3, we can easily see that larger particles are subject to larger detachment forces during the initial wetting. Considering that the debris particles are likely highly irregular, the geometric factor $l_{\mathrm{i}}$ that describes the overall circumference of the liquid/colloid contact may be much higher than the effective $R$ (as in $2\pi R$) would suggest.

The elastic force force (eq. 5.4) itself only grows slowly with $R$ due to the logarithmic dependence, however as stronger defects the larger particles should also

be able to support greater tension, accommodating for larger maximum extension $x$ prior to film rupture. As such, the elastic contribution may also remain relevant for larger particles, even in the case of a moderate surface-liquid contact angle.

Estimating the van der Waals adhesion force for carbon-based debris and CNTs via eqs. 5.6 & 5.7 is subject to great uncertainty due to the Hamaker constant $A$ and the separation distance $H$. For simplicity, let us consider CNT as a solid cylinder, and take $H = 1\,\mathrm{nm}$ for both debris particle and the CNTs[2]. Then, comparing a $10\,\mathrm{nm}$ diameter nanoparticle to a CNT of $10\,\mathrm{nm}$ diameter and length $L$, we get $F_{\mathrm{ad}} \approx 0.83 \cdot A_{\mathrm{debris}} \cdot 10^9\,\mathrm{nm}^{-1}$ for the spherical debris particle and $^{F_{\mathrm{ad}}}/_{L} \approx 0.20 \cdot A_{\mathrm{CNT}} \cdot 10^9\,\mathrm{nm}^{-2}$ for the carbon nanotube.

The composite Hamaker constant $A_{132}$ is subject to the individual constants for the silicon substrate, the solid body and water as the intermediate medium. However, these constants are typically in the range from $10^{-19}$ to $10^{-21}\,\mathrm{J}$ [58, 96] for solids interacting in water environment. Let us here take $A_{132} \approx 2.59 \cdot 10^{-21}\,\mathrm{J}$, from calculation of a $C_{60}$ Buckminsterfullerene on quartz surface in an aqueous environment [76]. We can thus approximate that $F_{\mathrm{ad}}$ is in the order of $0.002\,\mathrm{nN}$ for the debris particle, while the force can be up to 1000 times larger for a $1\,\mu\mathrm{m}$ CNT of equal diameter.

Comparing these very rough estimates to the maximum of the vertical detachment force $F^z_{\gamma,\,\mathrm{max}}$, it is suggested that the debris particles should generally be removed from the surface independent of their radius $R$, given the linear scaling of both the vdW adhesion force and the detachment force. For carbon nanotubes, the orientation is expected to be of great importance when it comes the the magnitude of the detachment force. Tubes with parallel orientation to the interface are generally expected to be detached ($F^z_{\gamma,\,\mathrm{max}} \gg F_{\mathrm{ad}}$), while in the case of perpendicular orientation the forces are of roughly similar in magnitude and the behavior is thus expected to be unsystematic.

We may also try to estimate the relevance of the DLVO effects on the non-retarded van der Waals adhesion based on the interaction energies. In eq. 5.8 for the van der Waals interaction energy $\Delta G_{\mathrm{vdw}}$, the correction factor for retardation with $R = 5\,\mathrm{nm}$ and $H = 1\,\mathrm{nm}$ is about $0.16$ and $\Delta G_{\mathrm{vdw}} \sim \cdot 10^{-21}\,\mathrm{J}$. In order to compute the electrostatic term $\Delta G_{\mathrm{el}}$ (eq. 5.9), the surface potentials $\psi_{\mathrm{col}}$ and $\psi_{\mathrm{sub}}$ need to be approximated by their $\zeta$-potentials[3]. For the KCl solution, the term is in the order of $10^{-22}\,\mathrm{J}$, i.e. smaller than the adhesion term. HCl solution however, it is of higher magnitude, $\Delta G_{\mathrm{el}} \sim 10^{-20}\,\mathrm{J}$, indicating a DLVO energy barrier. Given that not all source values are readily available, this is however a very rough estimate.

Finally, let us try to get a feeling of the hydration interaction, and its magni-

[2] A rather large estimate for a CNT on smooth silicon surface, but I am keeping to values used in the seminal work by Leenaars [73].

[3] $\psi_{\mathrm{col}} \approx -10\,\mathrm{mV}$, $\psi_{\mathrm{sub}} \approx -10\,\mathrm{mV}$ for the $1\,\mathrm{M}$ KCl solution and $\psi_{\mathrm{col}} \approx -18\,\mathrm{mV}$, $\psi_{\mathrm{sub}} \approx -10\,\mathrm{mV}$ for the HCl solution were based on existing works on C60 fullerenes [21] and silica surfaces [119] as minimum values.

tude on our samples. Equation 5.11 is also problematic for our experiment, since accurate values of the parameters $H_0$, $\gamma_\mathrm{i}$ and $H_\mathrm{y}$ cannot be established, and existing experiments cover a very limited set of materials. In particular, $H_\mathrm{y}$ likely has an intermediate value that could be either positive or negative, and we do not have means to relate it with the selected surface treatment on our hydrophilic and hydrophobic substrates. The best we can do is to estimate the maximal hydrophobic attraction, which we take to represent the hydrophobic case of in our trials.

For this, we take $H_0 \sim 1\,\mathrm{nm}$ and $\gamma_\mathrm{i} \sim 50\,\mathrm{mJ/m^2}$, as suggested in [29], and $H_\mathrm{y} = 1$. This gives $W_\mathrm{H} \sim 40\,\mathrm{mJ/m^2}$ at separation distance $H = 1\,\mathrm{nm}$. Projecting a 10-nanometer $C_{60}$ buckyball onto a surface gives an approximate circular contact geometry with radius $r = 5\,\mathrm{nm}$, and with that we find an attractive potential in the order of $10^{-18}$ J, i.e. much higher than the DLVO attraction. This suggests that the hydration forces likely dominate in highly hydrophobic circumstances, but it is hard to say whether this extends to the moderately wetting surface of our control experiments.

## 5.2 Review of existing studies

The theoretical picture of colloid detachment that we have so far discussed has been utilized in several experimental works. It is therefore of interest to review some of these studies, and consider their implications to our work. However, it needs to be pointed out that these studies deal predominantly with spherical, micron-scale colloidal particles, where the theory is subsequently well-established. The few instances where more complex geometries have been considered are highlighted in the following. The size scale in these works almost never extends down to the nanometer scale, and it is therefore hard to draw direct parallels between them and our studies.

The most comprehensive series of experimental works on retention and detachment of colloidal particles from smooth surfaces have probably been carried out by Flury and his coworkers. In a 2008 paper by Sharma *et al.* [106], the detachment of chemically modified spherical colloids from glass slides was investigated in an arrangement resembling our immersion cleaning experiments.

The colloidal particles, approximately $1\,\mu\mathrm{m}$ in diameter, were obtained in four different chemical pre-treatments to provide different wetting and surface charge properties. The deposition onto glass slides took place in a flow chamber followed by rinsing in colloid-free solution (clean water pH-adjusted with $CaCl_2$). To prevent exposure to liquid interfaces at this point, the chamber was allowed to gradually evaporate before the sample was recovered. The samples were then mounted vertically within a beaker where clean solution was pumped at a specific flow rate, causing the interface to gradually rise and pass over the sample surface. Once full, the container was allowed to overflow to evacuate any detached particles. Then, the direction of the pumping was reversed, and the receding interface was allowed to

interact with the sample.

The authors used confocal microscope before and after the interface process to investigate particle detachment from the surfaces. Repeat experiments were carried out to investigate their effect on colloid detachment. Theoretical modeling of the particle adhesion was through the means of the DLVO theory that combines van der Waals adhesion to the screening due to the ionic double layer, which results into a more realistic interaction in an electrolyte solution than pure non-retarded vdW-adhesion. In addition, the surface charge of the colloidal particles was taken into account. The static model in eq. 5.1 was utilized for the surface tension force.

The key results of this work relevant to our studies were that colloid detachment mainly took place following the first two passes (back-and-forth) of the liquid interface over the sample; due to the nature of the experiment, the advancing and receding interfaces could not be told apart in this respect. While both hydrophilic and hydrophobic colloids were found to detach from the surface, the colloids with hydrophobic surface treatment detached in larger numbers. The hydrophobic colloids detached almost completely regardless of their surface charge, while the detachment of hydrophilic ones was found somewhat sensitive to their charge state.

The higher end of the immersion velocity range used in this study (approximately from $10$ to $100\,{}^{\mathrm{cm}}/_{\mathrm{h}}$) was also comparable to lower end of the scale ($0.01$ to $0.1\,{}^{\mathrm{mm}}/_{\mathrm{s}}$) utilized in our works. The experiments suggested weakly decreasing particle detachment with increasing immersion velocity, which was supported by a probabilistic view of the process: the slower the velocity, the greater the probability the mobile interface interacts with the particle in a meaningful manner, i.e. forms a three-phase contact line which takes some finite period of time. This way, the velocity of the interface may still have a statistical effect on detachment even though it does not have a direct effect on the detachment condition in the static view of the process on single-particle level (eq. 5.3).

Another paper published in 2011 (Aramrak *et al.*) expanded upon the topic of velocity dependence [4]. This work is probably the most central with respect to our studies since it dealt exclusively with hydrophobic microcolloids. The method of particle detachment was by successive exposure to air bubbles injected into a liquid-filled glass channel that was utilized as the substrate. Quantitative estimates were now done *in-situ* by a confocal microscope assembled above the channel, and the velocity of the air bubbles was determined by altering the flow rate of the liquid with a syringe pump. Theoretical treatment was similar to the previous paper, although the maxima of the vertical and horizontal surface tension force components were explicitly now considered.

The refined experimental arrangement allowed for decoupling of the advancing and receding interfaces, when both could be individually visualized for each injected bubble. The experiments clearly demonstrated that the advancing interface of the first passing bubble caused a greater degree of detachment (up to $80 - 88\,\%$ of all

detached particles) than its receding interface ($5 - 10\,\%$), and that subsequent bubbles did not cause much additional detachment. This result supports our interpretation of the immersion cleaning of CNT-samples, where the advancing interface of the initial immersion appears to be responsible of the cleaning effect. Aramrak *et al.* argued that the asymmetry was due to different advancing and receding contact angles of their colloids that were measured to differ from one another by about $20°$.

The range of interface velocities in this work was much broader than in the previous paper. The authors found lack of significant velocity dependence on slow to medium flow rates that was contrasted by rapid fall with faster interface velocities beyond $1000\,{}^{\mathrm{cm}}/_{\mathrm{h}}$, which roughly corresponds to the high end of velocities in our investigations ($\sim 1\,{}^{\mathrm{mm}}/_{\mathrm{s}}$).

The authors attributed this to the thickening of the thin liquid film that separates the air bubble from the channel wall in their arrangement. The thickness of the film depends on the flow rate, and it was found to correspond to the diameter of the colloids at the onset of the rapid fall. As such, the bubbles no longer made contact with the colloids at this high interface velocities, and the interaction was lost. This is a non-factor in our experiments with a macroscopic liquid surface, rather than an air bubble, interacting with the particles.

Aramrak *et al.* expanded on their previous work in a 2013 study that focused on whether the shape of the colloids, and their orientation relative to the interface made difference in the detachment [5]. They utilized polystyrene-based spherical modified to three different shapes (rods, barrels and oblong disks), with unmodified spheres used as the control shape. The deposition and the detachment experiments were done similar to the previous work in a flow chamber with injected air bubbles interacting with the surface. The flow rate was kept constant throughout the experiments, and *in-situ* confocal microscopy was again used for characterization.

The authors suspected that the colloids with non-symmetric shapes would tend to align their main axis along the flow direction during the deposition step. This was verified with SEM that showed that colloids with higher aspect ratio were aligned most consistently, however there was significant deviation from unified orientation for each colloid type: the oblong disks oriented more perpendicular to the interface than the rods, while the barrels tended to orient slightly parallel on average. In the practical experiment, the barrels were subject to the greatest degree of detachment, while the rods detached least. The detachment of oblong disks lied between these extrema, close to the detachment of the spherical controls.

In the theoretical analysis, the colloid shape was considered through two different methods that both involved the modification of the geometric factor $l_{\mathrm{i}}$ in the expression of the surface tension detachment force, eq. 5.3. It was found that isotropy-related orientation of the particles could not fully explain the differences in the detachment of the different shapes, particularly that of the oblong disks whose highly anisotropic shape combined with relatively strong orientation along the flow

direction ought to have minimized the detachment force.

The authors concluded that the presence of sharp, pronounced edges must have enhanced the detachment of the oblong disk shape by allowing for pinning of the liquid interface, as illustrated in our preceeding discussion of the elastic shear force (Eq. 5.4). The same effect also increased the detachment of barrel-shaped species with respect to the spherical control particles, while the rods that had a smooth, spherical cross-section were unaffected. This result is of importance for our studies, because it shows that the pinning effects may relevant in the interfacial detachment processes, even though the elastic force that rises should trivially be constrained onto the plane of the surface.

Aside from experiments on microcolloids suspended on samples, Flury *et al.* have also reported on several works that utilize force tensiometry to directly measure the capillary forces that mobile liquid interfaces subject to particles as a function of their vertical position as they pass through a liquid surface. The capillary force is then a sum of the surface tension force and Laplace capillary pressure. In addition, buoyancy leads to an additional contribution that is dependent on the volume of the submerged portion of the particle.

A separate tensiometer study of 3D-printed model particles (Chatterjee & Flury, 2013 [20]) deals with considerably larger size scale than our measurements, but also underlines the relevance of the pinning effect to the particle-liquid interaction, particularly in cases where the particles have beveled shapes, or are subject to surface roughness. Particle shapes with fixed cross-section (cubic or cylindrical particles) gave rise to the clearest indication of this effect when immersed along their major axis, with pinning taking place both in the beginning and in the end of the wetting process. Tapered cross-sections (e.g. conical or square pyramid shapes) lead to a large pinning at the base of the shape, but no pinning at the top where the contact line vanished gradually. Particles with round cross-section (sphere & ellipsoid) did not show any pinning at the initial contact, but at the top a slight pinning event was witnessed, probably due to the surface roughness.

Aside from the studies published by Flury *et al.*, comprehensive works on colloid retention and detachment under similar circumstances have also been published by Lazouskaya *et al.*. The one most relevant to our interests is the study from 2013 [72], which utilized experimental methodology largely similar to Flury's flow channel experiments [4,5]. Here, various previously ignored aspects of the colloid-interface interaction were however brought up in the analysis.

These authors provided a more detailed analysis of the difference between advancing (imbibition) and receding (drainage) contact lines in the colloid-level picture of the detachment process. They pointed out that given the entire range of the filling angle $0 < \phi < 180$, two extrema are in fact expected in eq. 5.3, a negative and a positive one. For both imbibition and drainage, both of them are met, but in different order, and which one is the maximum and which one the minimum depends on the

substrate contact angle $\alpha$.

Different modes of particle detachment (lifting, sliding & rolling) were also considered thoroughly, and criteria developed for each case to make up a complete theoretical model to predict colloid mobilization. Characterizing particle adhesion through the established DLVO theory, they plotted the criteria for lifting and sliding as $\theta$ verse $\alpha$ for $1\,\mu\mathrm{m}$ spherical colloids. This plot predicts that save for cases where where both angles are very high ($> 140°$), or very low ($< 15°$), at least one of these mechanisms should always be effective in colloid detachment for either imbibition or drainage. The surface contact angle $\alpha$ is generally predicted to be the dominant angle that determines whether the colloids become mobile; their own contact angle $\theta$ only appears relevant in the aforementioned extreme cases. This can be regarded to complement the analysis in Leenaars' original work [73], where it was shown that the vertical surface tension force tends to becomes large whenever $\alpha$ and $\theta$ are close to the opposite extrema $[0°, 180°]$.

The regime for mobilization by sliding lies within a relatively narrow range of $\alpha$ between the lifting and no-mobilization regimes. Relevant to our case for low $\alpha$ with moderate $\theta$, only lifting is expected to be effective. In accordance to eq. 5.3, the maximum detachment force is reached at $\phi = {}^{\theta_0}/_2$, while the other extremum, $\phi = 90° + {}^{\theta_0}/_2$, is negative and thus inefficient at colloid detachment. However, the criteria might naturally be wildly different for our carbon nanotube depositions.

According to this analysis, rolling of the particles due to torque brought about mainly by the horizontal component of the surface tension force ought to be a relevant mode of colloid mobilization for broad $\alpha$ and $\theta$ ranges that also overlaps our range of interest. I am however skeptical whether this is relevant to our case where the low surface contact angle $\alpha$ and small particle dimensions lead to a small lever arm of torque for the surface tension force ($I_\gamma = R\sin\alpha$) with respect to that of the adhesion force ($I_\mathrm{A} = ({}^{4F_\mathrm{A}R}/_A)^{1/3}$) resisting the rotation.

The experiments presented in the paper generally supported the theoretical predictions. The most evident deviation was the lack of colloid detachment in the event of drainage (receding contact line) on hydrophilic substrates, which was witnessed similar to the experiments by Flury *et al.* Given the aforementioned analysis, some of the mechanisms for particle detachment should have been effective for this case as well, and yet it could not be observed experimentally. Lazouskaya *et al.* speculated this was due to the effects of residual "trailing films" left behind following the macroscopic drainage fronts. Similar to pre-wetting precursor films that may precede the macroscopic front in the case of imbibition, they greatly complicate the molecular-level picture of the detachment process.

Apart from these authors, there are a few independent works that stand out in the literature. The papers by Gomez-Suarez *et al.* are of great relevance, because they predate the former works and consist an earlier independent examination for the concepts initially introduced by Leenaars & O'Brien. In a work from 1999

[111], the experimental layout was similar to the previously discussed flow cell experiments, with air droplets giving rise the colloid detachment. The samples consisted of spherical polystyrene particles of about $800\,\mathrm{nm}$ in diameter deposited on quartz surfaces. The detachment of these particles was investigated as the function of interface velocity, the number of interface passages and the surface tension of the liquid, with up to 60 % of 1-propanol added to the $10\,\mathrm{mM}$ $KNO_3$ solution to lower its surface tension.

Experiments showed clear dependence of the colloid detachment to each of these variables: the particle removal weakened linearly with increasing liquid-air interface velocity. The gradient of the dependency was however greatly pronounced compared to the studies by Flury *et al.* [4, 106], which in the light of those works can be understood as a result of the high range of velocities probed here (from $2$ up to $15\,{}^{\mathrm{mm}}/_{\mathrm{s}}$). This leads to strengthening of the liquid film separating the air bubbles; the film thickness was found to rival, or even exceed, the particle dimensions at the highest velocities.

This paper is also a rare example of an experiment where the overall detachment could be improved by repeating the interface process: the relationship between the detachment and the number of consecutive air bubbles passed through the channel is remarkably linear, albeit this was reported exclusively for the highest interface velocity. The authors interpreted that at sufficiently high velocities, the capacity of an individual bubble interface to capture particles may be limited. This interpretation was later agreed by Sharma *et al.*, given that aside from being much slower, their bubbles had much more surface area [106]. This effect should not factor in in our experiments with virtually unlimited space at a macroscopic interface.

With respect to the surface tension, the relationship is also linear, with the optimal detachment achieved for unmodified solution with the highest surface tension. The relationship also remained linear for different interface velocities; given that altering the IPA content of the solution also changed its dynamic viscosity, it was then argued that the viscous effects (to be discussed in the following) did not play a role in the process; hence, even at this relatively high range of interface velocities, this study supports the static view of the process where the colloid detachment is fully determined by the force balance of the adhesion and the surface tension detachment force (eq. 5.3).

The static picture of the particle detachment can also explain the self-cleaning property of various superhydrophobic surfaces (contact angle $\alpha > 150°$) as a consequence of the colloid mobilization. In the recent work by Yu *et al.*, 2014 [127], spontaneous detachment of colloids from lotus-like surfaces by their interaction with the contact lines of sliding droplets was correctly predicted based on the well-established model even though only the drainage phase (retracting contact line) was considered. The authors argued that the critical conditions necessary for self-cleaning property to be established are generally fulfilled on most superhydrophobic surfaces

for the common dust particles ($R$ from a few up to a few hundreds microns), with a critical radius calculated in the millimeter scale. Beyond this, the particles become so heavy that they can no longer be mobilized by the surface tension force.

### 5.2.1 Dynamic effects

The previous static model of the particle-interface interaction does not provide a direct velocity dependence of the colloid detachment; yet, in most of the existing works, slowly moving interfaces are more efficient in the detachment than fast-moving ones, and above certain critical velocity virtually no detachment takes place. In order to account for such possible effects, the dynamics of the fluid-particle interaction can be considered. This was done in Leenaars' and O'Brien's 1989 article [74]. Despite various simplifying assumptions, the stringent mathematical solution is complicated, and will only be discussed here in qualitative manner.

Given the small dimensions involved in the process of microcolloid wetting by passing fluid meniscus, the relevant hydrodynamic equation of motion would be the so-called Stokes' creeping flow equation, however a complete solution of such problem in three dimensions would be very difficult. This highlights the fact that hydrodynamic forces arising in the bulk of the fluid that are known to be of great importance in Stokes flows were ignored in the simple static analysis. The most obvious one of such forces is the drag force, which can be quantified with the Stokes law for a sphere in free stream:

$$F = 6\pi\mu R V_{\mathrm{f}}, \tag{5.12}$$

where $\mu$ is the viscosity of the fluid and $V_{\mathrm{f}}$ the flow velocity. In case the liquid is at rest, it can be taken as the velocity of the interface relative to the particle, $V$, and as such this force becomes very small for immersion velocities relevant to most experiments. The drag force can thus be generally ignored.

Let us therefore assume that the initial separation of colloids from the underlying substrate is primarily subject to the surface tension force; the particle begins moving away from the surface if the vertical component of the surface tension overcomes its adhesion to the surface. Leenaars and O'Brien argued that this is a necessary, but not sufficient, condition for the particles becoming permanently detached from the surface, since additional reactive forces may arise to counteract the surface tension force as soon as separation begins. In particular, it is important to realize that the surface tension force is only active during the wetting process of the particle, and ceases as soon as it is fully submerged while any reactive forces may still be felt by the particle in much longer timescales. In such case, it may get forced back into contact with the surface if the initial separation due to the surface tension was not sufficient.

It turns out such a reactive force does appear as soon as the particle has been

slightly elevated from the sample surface. It is the so-called viscous force, projected by the lubrication theory, and unlike the lateral drag force it is directed to oppose the vertical motion. The mathematical description of the viscous force can be carried out via the so-called lubrication approximation that deals with thin fluid layers.

Unlike the surface tension force, the viscous forces depend on the velocity of the particle in a continuous manner, and do not abruptly cease as the particle is fully immersed in liquid. Whether the particle becomes completely free of the substrate's influence then depends on whether the surface tension force is able to move it sufficiently far away from the surface; that is, the initial, momentary impulse given by the surface tension force must be large enough to overcome both the adhesion and the subsequent reactive viscous forces. This can be expressed simply by

$$\int_0^t (F_\gamma - F_\mathrm{A} - F_\mu)\,\mathrm{d}t = mv(t), \tag{5.13}$$

where $F_\gamma$, $F_\mathrm{A}$ and $F_\mu$ are the surface tension force, adhesion force and the viscous forces, respectively. It hence becomes evident that the timescale for which the surface tension forces operate is of great relevance, and this is how the immersion velocity affects the process.

Leenaars and O'Brien utilized this as a starting point for derivation of a one-dimensional equation of motion for a spherical particle under the influence of surface tension, viscous and adhesive (i.e. van der Waals) forces. This was done with the help of several simplifying approximations in the axisymmetric geometry (Fig. 5.1a). In explicit form, the equation reads

$$m\ddot{x} = 2\pi R\gamma \sin\left[\phi(t)\right] \sin\left[\theta - \phi(t)\right] - \frac{AR}{6x^2} - 6\pi\mu R^2 \frac{\dot{x}}{x}, \tag{5.14}$$

where $m$ is the particle mass and the coordinate $x$ points to the vertical direction, upwards from the sample surface. Finally, $x(t)$ is the particle-substrate separation as the function of time.

The equation of motion was then solved for analytical expression of $x(t)$ at the non-inertial limit of $m \to 0$, given that the inertial term is unlikely to play a significant role for such tiny particles. As a result, the only boundary condition relevant for the problem is $x(0) = H$, i.e. the initial displacement between the particle and the surface is taken as the equilibrium separation utilized in the relation for the van der Waals adhesion force for a sphere on a planar substrate, eq. 5.6. Unsurprisingly, that expression also appears as one of the terms in the equation of motion, where $A$ is now the compound Hamaker constant of the entire system. Both $H$ and $A$ are subject to great deal of uncertainty in any practical system; in particular, $H$ is not directly accessible, and must be taken as a rule-of-thumb estimate. Accordingly, the authors stressed that this is one of the main sources of uncertainty in their final solution.

The rest of the terms on the right-hand side of the equation represent the other

forces. The first one is simply the expression for the surface tension force (eq. 5.1). The final term, $6\pi\mu R^2\,\dot{x}/x$, represents the viscous reactionary force, and its expression was derived in the paper in a quasi-steady state in the axisymmetric picture of the wetting process. For the purpose of the problem at hand, it is sufficient to use an approximate solution given by

$$F_\mu = \frac{6\pi\mu R^2 W}{H}, \tag{5.15}$$

where $W$ designates the velocity the particle lifts vertically from the surface.

Leenaars and O'Brien provided the analytical solution for eq. 5.14 in both dimensionless and regular forms. The solution that preserves the dimensions allows us to take note of the key parameters:

$$\begin{aligned} x^2(t) =& H^2 \exp\left[\frac{2\gamma}{3\mu R}\int_0^t F_\phi(t')\,\mathrm{d}t'\right] - \frac{2A}{36\pi\mu R} \\ & - \exp\left[\frac{2\gamma}{3\mu R}\int_0^t F_\phi(t')\,\mathrm{d}t'\right]\int_0^t \exp\left[-\frac{2\gamma}{3\mu R}\int_0^{t'} F_\phi(t'')\,\mathrm{d}t''\right]\mathrm{d}t', \end{aligned} \tag{5.16}$$

where a shorthand notation $F_\phi(t) = \sin[\phi(t)]\sin[\theta - \phi(t)]$ has been used. We can see here that the fraction of the liquid surface tension and viscosity, $\gamma/\mu$, is of importance: the final exponential diminishes as the fraction approaches infinity, which limits the growth of the last term as a whole. In the meantime, the first term tends to infinity. This implies that the detachment is promoted for liquids that possess a large ratio of surface tension to viscosity, e.g. water.

The influence of the immersion velocity is similarly seen if the dimensionless form of the solution is written out, which also has the benefit of simpler appearance:

$$x^2(t) = \exp\left\{\frac{2}{\lambda}\left[I(t) - I(0)\right]\right\} - \frac{2\delta}{\lambda}\exp\left[\frac{2}{\lambda}I(t)\right]\int_0^t \exp\left[-\frac{2}{\lambda}I(\theta)\right]\mathrm{d}\theta, \tag{5.17}$$

where $\delta$ is a constant, $x$ and $t$ now designate their dimensionless equivalents, and $I(t)$ is the shorthand notation for the integral of the nondimensionalized expression for surface tension force. The details of the nondimensionalizing process will be omitted; the relevant point is the recurring dimensionless group $2/\lambda$, which corresponds to $\gamma/\mu V$, i.e. the reciprocal of the capillary number $\mathrm{Ca}$. The effect of the velocity $V$ in the process thus also becomes evident. At sufficiently high value of $V$, the impulse from the surface tension force becomes too brief to allow for sufficient separation of the colloid from the surface, and it falls back into contact as a result of the viscous recoil. This corresponds to the maximization of $x(t)$, and the possible measures towards this goal include anything that minimizes the capillary number $\mathrm{Ca}$ of the system.

## 5.3 Theoretical considerations: summary

We conclude that colloid detachment from smooth sample surfaces is generally explained by the simple static model originating from Leenaars & O'Brien [73,74]. The dominant detaching force in this model is the surface tension force, and its vertical component directly competes against the surface adhesion of the particle. In most cases, it is sufficient to consider the maximum of the vertical surface tension force: in simple terms, detachment takes place if it exceeds the adhesion force.

Our results can also be qualitatively understood based on the same model. The difference between the detachment of CNTs and debris particles mainly arises due to relative differences in the adhesion and detachment forces. Rough estimates suggest that the surface tension force should generally be effective at removing spherical debris particles given that the force is comparable to the adhesion, and both scale linearly with particle radius $R$. CNTs, on the other hand, generally benefit from their high aspect ratio which resulting in much greater adhesive force. This gives rise the selective detachment that is desirable for our applications.

The fact that lateral translocation of particles cannot be seen in our experiments indicates that the transverse component of the surface tension force is relatively weak. This can be understood as a consequence of the hydrophilic nature of our substrates, which should result to its diminishing. We also expect the imbibition phase (advancing contact line) to be far more relevant than the drainage phase (receding contact line) in the detachment as witnessed in other experiments carried out under similar circumstances [4,5,72], and indeed we have reason to believe that this is the case in our experiments. Possible causes of this include, e.g., hysteresis of the colloid contact angle (as argued in [4]), trailing films (as in [72]).

Likewise based on other works, we expect repeat processes to be ineffective in improving particle detachment [4,72,106]. This is also our experience, although the reasons for this may be complicated. In the previous studies, this has typically been attributed to particle attachment in the primary and secondary minima of the retarded vdW-interaction predicted by the DLVO theory, or preferential attachment to certain favored locations [5,106].

In our case, the chemistry of the Si/SiOx substrate is probably also permanently modified by the initial wetting process. For example, as mentioned in chapter 3, it is recognized that when a hydrophilic $SiO_2$ surface with OH groups comes in contact with liquid water, a few monolayers thick layer of $H_2O$ molecules is hydrogen-bonded to the surface in ice-like fashion [24]. Given that the function of the hydrophilic oxygen plasma treatment is to increase the density of these bonds, this behavior could be pronounced on our samples, and its effects on the particle detachment balance may be unpredictable. This factor could also play a role in explaining why the receding contact line does not appear to play a role in our experiments, given the initial wetting at the advancing line.

Of other parameters that may influence the extent of cleaning, the velocity of

the interface has been found to have an effect. In the existing studies, a correlation is typically found between decreasing velocity of the liquid interface and increasing particle detachment [4, 106, 111], but the quantitative relationship between these parameters is not very clear. Strong, linear, relationship has only been witnessed above the threshold of $\sim 0.1\,{}^{\mathrm{mm}}/_{\mathrm{s}}$ [4, 111], while our velocity scale lies between $0.01$ and $1\,{}^{\mathrm{mm}}/_{\mathrm{s}}$. As such, there is no reason for us to necessarily expect a very dramatic interdependence based on existing works.

We only saw a clear velocity dependent-detachment in our third paper, not in the second work. We attribute this difference primarily to the evaporated AFM imaging references: In the previous work, their presence may have disrupted the smooth progression of the contact line in the vicinity of the imaging region, obscuring the dependence. The positive correlation between decreasing interface velocity and detachment of debris particles is not only clear in the latest study, but also remarkably linear for all three solutions, even though our data is limited to three points in velocity only. Furthermore, the trend also remains clear for the CNTs.

The dynamic model of the colloid detachment introduces the viscous reactive forces that may inhibit particle detachment if the interface moves too quickly [74]. Most experiments are however generally well-explained by the static model alone, with the velocity dependence of particle detachment usually considered in terms of a probabilistic approach on the detachment process: the faster the interface moves, the shorter the duration of the particle-interface interaction, and less efficient the transfer of momentum on an average particle. Slower pace of wetting, on the other hand, promotes the formation of a three-phase contact line that is a prerequisite for the particle detachment [106]. This provides a sufficient explanation for the observed velocity-dependence in most cases, and suggests that the dynamic effects only become relevant at interface velocities much higher than what are relevant to us [111].

From application viewpoint, changing the immersion liquid is also unlikely to bring additional improvement in the extent of detachment, given that the surface tension $\gamma$ for water is hard to surpass for a practical experiment. Based on other works, the elastic shear force associated with deformation of the liquid contact line is however likely to also play some role in the detachment process, even though it is directed in parallel with the surface [5, 20]. Other factors that could play role in the detachment include hydrodynamic shear (i.e. drag) forces, which are however generally found negligible for micron-sized or smaller colloids [4, 74]. In our flow tube scheme, the rinsing flow may have been a factor contributing to the overall improved particle detachment, but trial experiments with samples immersed in different orientations relative to the flow direction did not indicate this to be a dominant factor. Likewise, gravity and buoyancy can be safely ignored at scales relevant to this work.

The main deviation between our studies and others is that a very hydrophilic

substrate surface ($\alpha \approx 0°$) is required for systematic cleaning for our samples; the oxygen plasma treatment utilized makes the silicon surfaces virtually completely wetting, and foregoing this step gives rise to non-systematic behavior even though unmodified Si/SiOx surfaces are relatively hydrophilic in ambient conditions ($\alpha \approx 30°$, cha. 3). This is in contrast to most other works, where good detachment has been achieved with moderate contact angles that generally correspond to that on unmodified silica ($20° < \alpha < 40°$). Furthermore, control experiments with substrates treated in dilute HF suggest the resulting moderate contact angle ($\alpha \approx 50°$) is already large enough to disrupt all cleaning behavior, although theoretical analyzes imply that the circumstances should still be relatively favorable for detachment [72,73].

Hydration interactions have so far not been discussed in the context of the colloid detachment and retention due to liquid interfaces, but may be very relevant for our nanoscale particles. The hydrophilic form of the interaction gives rise a substantial repulsive potential that may enhance the detachment of particles on hydrophilic surface. In the meantime, the hydrophobic interaction dominates the DLVO adhesion in the hydrophobic scenario. Given that we have no means to verify the value of the Hydra parameter $H_{\mathrm{y}}$, we do not know which type of interaction is active on our samples, but considering that the nanocarbon particles possess a hydrophobic nature, it seems likely that $H_{\mathrm{y}} > 0$, particularly for the control experiments carried out on substrates rendered hydrophobic. As such, hydrophobic interactions constitute a possible, and in my opinion, the most likely explanation as to why our experiments seem particularly sensitive to the surface chemistry of the substrate.

Another factor is that the wetting of our irregular carbon nanoparticles and carbon nanotubes is unlikely to be well-represented by the static model intended for smooth spherical colloids; given the hydrophobic nature of the irregular carbonaceous debris, the wetting may be incomplete in the nanoscale unless balanced out by superhydrophilic surface. An interesting question for further study would be how the ability of water molecules to infiltrate underneath the CNTs and debris particles depends on their contact angles and that of the substrate, as wetting of the contact would have a significant effect on the magnitude of the vdW-adhesion (eq. 5.3) via the Hamaker constant $A_{132}$. This could be investigated via molecular dynamics simulations.

Accurate mathematical description of a real-world mobile liquid contact line is always be fraught with difficulty. The biggest ambiguity in the analysis is no doubt related to the non-exact nature of the contact angles. One on hand, there's the question of the difference between the apparent, macroscopic contact angles that are measurable, and the microscopic contact angles that genuinely quantify the nature of the liquid contact at the submicron scale, but cannot be observed [14]. Second, even the measurable, apparent contact angles are generally non-exact, and subject to hysteresis that leads to different values for the advancing and receding static contact angles [64], and these further depend on the velocity of the interface as well.

Leenaars and O'Brien pointed this issue out in their joint work [74], and suggested that the tendency of the advancing contact angle to increase with increasing interface velocity could decrease the impulse delivered to the colloidal particle in the dynamic picture. This independent of the direct effect of interface velocity, so its influence to the detachment could then appear at lower velocities than initially thought. On the other hand, it was mentioned that other works suggest microscopic contact angle might in fact maintain a static value at all times, with the dynamic instabilities of the apparent value brought about by viscous distortions at submicron scale. This is supported also by more recent knowledge, although opposing views have also been presented; see e.g. Blake (2009) [14] for a review on the topic.

Given this ambiguity, considering the non-equilibrium contact angles for the purposes of particle detachment seems like a moot point, and as such we content ourselves with estimates for the static angle. This can be justified by our estimate in chapter 3, where we found that the effect of contact line motion on the contact angle should be limited to a few degrees in our arrangement, given the relevant velocity range. Much of the same reasoning applies to the liquid-colloid contact angles; they have generally been measured in the macroscopic perspective on colloid-covered substrates, and thus may not accurately represent the genuine angle associated with the interfacial interaction at single-colloid level. In the case of carbon nanotube depositions, the exact tube-liquid or particle-liquid angles are likewise inaccessible, and the situation becomes even more complicated as these two mix in a practical deposition.

Further uncertainty to our interpretations is brought about by the possible role of precursor films, which we have so far not considered. The quantitative descriptions for precursor and trailing films are still largely under debate, although they are believed to occur frequently in spreading and drying processes of liquids. Given that imbibition phase is dominant over drainage in our experiments, precursor film is the one relevant to us. In general, these films are considered to be present when the substrate-liquid contact angle is small. Given the extreme sensitivity of our cleaning process to the contact angle relative to other similar works, it is therefore good to note the possible relevance of such films to the interpretation of our results.

The kinematic role of the precursor film is to exhaust some of the free energy associated with the wetting process [27]. It is hard to find experimental data on the dimensions of the film in case of water, but some general remarks can be made based on theoretical considerations. For completely wetting liquids, the thickness of the film is typically from $10$ to $100\,\mathrm{nm}$, and its length $L_\mathrm{p}$ (i.e. how far it emanates the bulk liquid) depends inversely on the capillary number of the system, $L_\mathrm{p} \propto \mathrm{Ca}^{-1}$ [18]. For the velocity range relevant to our work, the capillary number is quite small, $10^{-6} < \mathrm{Ca} < 10^{-4}$, and as such the film may be rather pronounced. The plasma-processed silica surfaces utilized as substrates in our experiments can be considered virtually completely wetting. In case the contact angle of the system is finite, these

parameters become even harder to tabulate but in general the precursor film is expected to weaken [18].

The thickness of the film is of importance: molecular-thin films are unlikely to affect the mechanics of the detachment process, but a film whose thickness is a significant fraction of the particle dimensions may provide a degree masking from the macroscopic interface, similar to the wall film that could prevent efficient coupling of the interface and the particle in the flow channel in the air bubble experiments discussed before [4, 72, 111]. However, if the precursor becomes very thick, i.e. comparable to to thickness of the particles, it could in principle be the relevant detaching mechanism in itself for low-rising particles, i.e. our carbon nanotubes, as it progresses ahead the macroscopic interface.

While the validity of the static model for the detachment of spherical colloids has been confirmed for a broad velocity range, its applicability for carbon nanotubes or irregular debris particles is in question. There is a large gap in the size scales between spherical microcolloids and carbon nanotubes whose diameter is generally less than $20\,\mathrm{nm}$. Furthermore, the dimensions of the debris particles also extend far into the submicron regime. It is not clear whether the macroscopic surface tension concepts are directly applicable so far into the nanoscale. In particular, it is difficult to affirm the validity of the geometric considerations behind equation 5.1 (Fig. 5.1) in these non-standard geometries.

Microscopic irregularities that are present particularly in the CNT-debris particles, but also on the substrate, have a significant effect to the adhesive force and these were not taken into account in our analysis. Roughness associated with such microstructure may have unpredictable effects on the magnitude of the vdW-adhesion, depending on its size scale [96]. If the asperities are much smaller than the particles themselves, the adhesion is generally weakened as the size of the contact area is reduced. But if the size scale of the micro-structure exceeds that of the particle, the contact area may in fact grow, in which case the adhesion is strengthened.

Finally, changing the chemistry of the solution, in terms of ionic strength or pH, was expected to affect the particle adhesion in accordance to the classic DLVO picture of particle adhesion. Based on the results of our final work, the chemical environment does not however seem to play a very significant role, and colloid detachment is mainly dictated by physical interactions at the propagating contact line. A robust theoretical discussion of nanoparticle adhesion in terms of the DLVO theory would however require considering the entire adhesion curve as a function of the separation distance $H$, and both the primary and the secondary energy minima that arise. This would be challenging for CNTs and irregular debris alike. Aside from determining the chemical conditions of the detachment process, the associated experimental efforts would also demand a high degree of control over the deposition method and the environment. This could be difficult to achieve for unmodified carbon nanotubes with spin coating.

### 5.3.1 The orientation effect

As pointed out before, the interfacial forces provide possible pathways for some CNT orientation effects to rise as a result of the detachment process. We took interest in the possible observation of CNTs becoming re-oriented as a result of their interaction with the spreading droplet contact line in our initial study [51], however we were reluctant to draw direct conclusions due to complications of the analysis, in particular the parasitic residual orientation due to the spin coating whose effect could not be fully eliminated.

With our follow-up work on immersion cleaning [49], we were hoping to gain a more well-reasoned view with the comparative AFM method. Qualitatively, it was very clear that no re-orientation of individual MWNTs took place in these experiments. Only very few possible instances were identified, and even there the tube had locally bended, rather than re-oriented as a whole. This shows that if some effect to the tube orientation exists in response to the passing liquid interface, it predominantly due to selective removal of certain orientations in favor of others; the apparent re-orientation of the end-state then rises as a result of selective tube detachment.

Based on the strong dependence of the interface forces on the tube orientation discussed before, the species oriented parallel to the interface are likely favored in detachment versus the perpendicular ones. In order to explore this possibility, we manually identified all the MWNTs that had been removed over the immersion process on our set of quantitatively investigated samples, and measured their orientation from the data recorded prior to the immersion process. As a result, a clear picture of preferential detachment of horizontal CNTs (i.e. parellel to the interface) emerged, confirming our hypothesis. The effect is, however, weaker than one would anticipate considering the immense aspect ratio of an average MWNT ($\sim 100$), but this is understandable given that the contact line is not uniformly defined in the microscopic scale, and thus the preferred detachment orientation will have large local variance.

Use of a mobile liquid interfaces for systematic reorientation has been previously reported by Gerdes *et al.* for single-walled carbon nanotubes [101], and more recently by Khripin *et al.* for CNT-DNA composites [69]. In these works, the CNT re-orientation was understood in the context of the receding contact line of carbon nanotube dispersion interacting with the CNTs akin to the molecular combing method utilized for stretching and aligning DNA molecules [9,10]. Fundamentally, this technique relies on the elastic shear force we already discussed (eq. 5.4).

As per to the re-orientation mechanism as specified by Khripin *et al.*, the interface associated with the re-orientation was that of the receding carbon nanotube solution [69]. In both cases, the experiments were done on hydrophobic substrates, and functionalized, hydrophilic carbon nanotubes were used. This is in stark contrast with our case, where hydrophilic surface is a prequisite for the detachment of debris

particles, and the carbon nanotubes are in their native, hydrophobic state.

It is interesting to note that in Khripin's study, the possible role of detached CNTs on the overall orientation state was not discussed, although the deposition density of CNTs on the surface was found to be significantly lower than what was expected based on the theoretical calculation. This was explained as a result of the topmost tubes getting removed in the overlapping cases [69]. However, the sparsely populated deposition may also indicate that a significant fraction of the deposited CNTs detached in response to the contact line, although the high degree of coordinated alignment among the remaining species suggests that their model is otherwise valid.

# Chapter 6

# AFM analysis of particle detachment

Atomic force microscope (AFM) is utilized as the key quantitative imaging technique in our works. While traditionally seen as something of a niche instrument, the ever-growing variety of imaging modes and availability of affordable, easy-to-use commercial systems is rapidly turning AFM into a mainstream microscopy technique. Here, only a brief introduction to the technique will be provided; the main emphasis will be on the image analysis technique we have developed that features heavily in our works.

The main advantage of AFM over almost every other AFM technique (save for transmission electron microscopy, TEM) is superior resolution, particularly in the vertical direction. This is of particular interest for our carbon nanotube samples, where the thin CNTs can be detected, and their thicknesses estimated using AFM. The vertical resolution of AFM is very high, down to one angstrom, while the lateral resolution depends on the details of the probe and the surface structure and is typically in the range of tens of nanometers; even atomic resolution can be achieved with contemporary, commercial instruments on well-defined surfaces such as mica. Compared to electron microscopy, AFM is a completely ambient technique that does not require the surface to be conductive. As a result, preparation of the measurement and the sample is much easier.

The biggest drawback of AFM technique is its slow speed. Given the mechanical nature of the imaging process, increasing the scanning rate too much will greatly deteriorate the image quality. The image area is also limited, and capturing large images relevant to our work with sufficiently high resolution imposes strict requirements for imaging time. Each frame in AFM takes much longer than imaging the same area with scanning electron microscope (SEM), however the vertical height information can only be directly inferred in AFM, and there is no concern of the sample surface being affected by the imaging beam.

## 6.1 Introduction to atomic force microscopy

Atomic force microscope is a scanning-type microscopy technique that is used to study the topographic features of sample surfaces. Alternatively known as scanning force microscope (SFM), it is one of the chief subcategories of scanning probe microscopy (SPM), others being scanning tunneling microscope (STM) and scanning near-field optical microscope (SNOM). SPM techniques were invented in the early 1980's, starting with STM in 1981, and then the AFM in 1986, the same year Gerd Binnig and Heinrich Rohrer were awarded a half of the Nobel prize for inventing the STM [88].

In the SPM techniques, a nanometer-scale probe is dragged along the sample surface in a predesignated pattern, so that a specific interaction between the probe and the sample surface can be measured at each point. In STM, the interaction is the tunneling currently brought about by a potential difference applied between the conductive probe and a conductive sample. In AFM, the interaction is mechanical in nature; the surface forces (chiefly, the van der Waals force) will either attract or repulse the probe.

In a practical AFM (Fig. 6.1), the probe is a micron-scale cantilever equipped with a sharp nanometer-scale tip that closely tracks the surface topography. A feedback system is used to maintain the interaction between the probe and the surface constant during scanning. This translates into recording the surface topography from

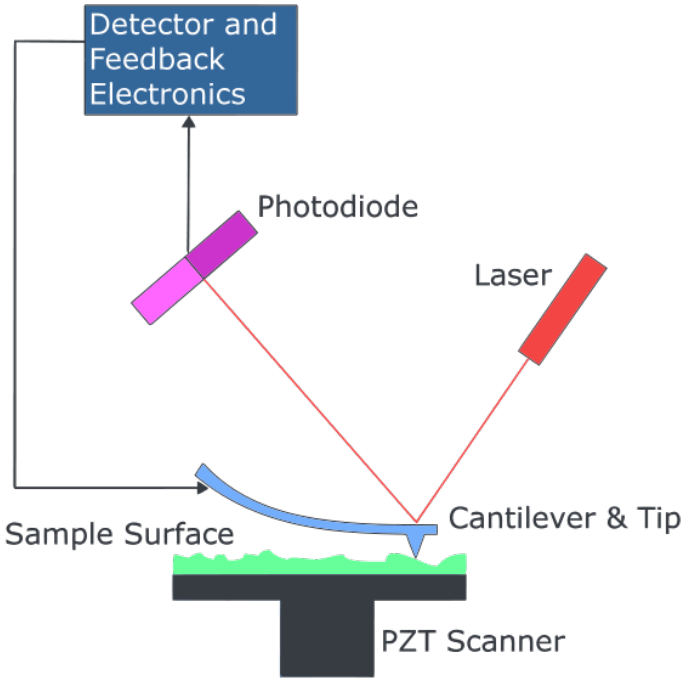


**FIGURE 6.1** Schematic of a typical AFM apparatus utilizing sample actuation and laser beam for the cantilever deflection measurement.

the corrective motions of the cantilever assembly, achieved through the means of piezoelectric actuation. Deflection of the cantilever beam is a relative measure of the force it experiences at any given time, and the vertical piezoactuator strives to maintain it constant. The deflection is typically measured through the means of a laser beam reflected from the cantilever back onto a position-sensitive photodetector. Piezoactuation is also utilized to realize the lateral scanning motion of the tip relative to the sample. Depending on the construction, either the tip or the sample may move, and the piezos for the vertical and lateral motions may be integrated or decoupled from one another.

Atomic force microscopy is in itself also an umbrella term for a variety of related techniques referred as imaging modes. Commercial instruments generally support a wide range of AFM modes, as well as STM. The method described so far is the contact mode AFM, which is nowadays rarely used. The most common, contemporary topographic imaging mode is the so called intermittent contact mode. In this mode, the cantilever is driven to oscillate near its resonance frequency, with the oscillation amplitude selected so that the tip merely taps the surface at the lower turning point of the oscillation[1]. In this case, the laser deflection scheme is utilized to measure the root-mean square (RMS) amplitude of the damped oscillation, which is used as the feedback signal. The RMS amplitude is kept constant by lifting or lowering the oscillating cantilever, and the topographic data is again inferred from these motions; the drive frequency and amplitude generally remain fixed.

Other than the surface topography, additional information can be inferred from the RMS amplitude signal that is otherwise constant but has a sharp feature whenever the feedback system adjusts scanner level. Therefore, all edges and other discontinuities are clearly visible in the amplitude signal. Furthermore, the phase of the cantilever oscillation relative to that of the drive signal can also be mapped, and provides information on the damping (e.g. mechanical properties of the sample surface) but is in practice often subject to severe disturbances.

In our work, all AFM measurements have been carried out in intermittent contact mode. In the original papers [49,51], two AFM instruments by Digital Instruments utilizing a Dimension3100 -type microscope stage have been utilized. In the most recent work, these instruments were upgraded to a Bruker Dimension Icon. This system features a better overall image quality with a closed-loop scanner imaging scheme that allows for larger individual images to be recorded with fewer artifacts. This simplifies the image analysis because we no longer need to worry about overlap between individual images when only a single frame is imaged per sample.

[1]The benefit of this approach is that the tip-surface interaction is much smaller than in full contact imaging, where the probe is dragged along the surface. This allows much more delicate samples to be probed. For CNT depositions, our practical experience suggests that the surface particles are rarely mobilized by the tip; this can be established by consecutive imaging of the same location on the deposition for several frames. Although the interaction force can still be substantial in the intermittent contact mode, the contact is very brief with the cantilever resonance frequency in the order of $\sim 100\,\mathrm{kHz}$.

The most important characteristics of AFM cantilevers are their resonance frequency $f_0$ and force constant $k$. In our latest work, imaging was carried out with series HQ:NSC14 ($f_0 = 160\,\mathrm{kHz}$, $k = 5\,{}^{\mathrm{N}}/_{\mathrm{m}}$) and HQ:NSC15 ($f_0 = 325\,\mathrm{kHz}$, $k = 40\,{}^{\mathrm{N}}/_{\mathrm{m}}$) commercial silicon probes by µmasch. These are typical values for intermittent contact mode probes. In general, good tracking of the surface is desired for high-quality image, while the interaction between the probe and the surface should be minimized. This requires careful optimization of the the imaging parameters (amplitude setpoint & feedback gains). The tracking is also affected by the lateral velocity of the tip: the scan rate was selected so that the tip velocity remained below $10\,{}^{\mu\mathrm{m}}/_{\mathrm{s}}$.

## 6.2 Quantitative image analysis methodology

I will now describe the image analysis methodology we utilized for our AFM data. The refined process outlined here applies for our most recent work [50]; for our earlier study, some of the details are different, and can be found in the online supplement of the paper [49]. The process as a whole is presented in the flow diagram of Fig. 6.2, where the various parameter values have also been indicated.

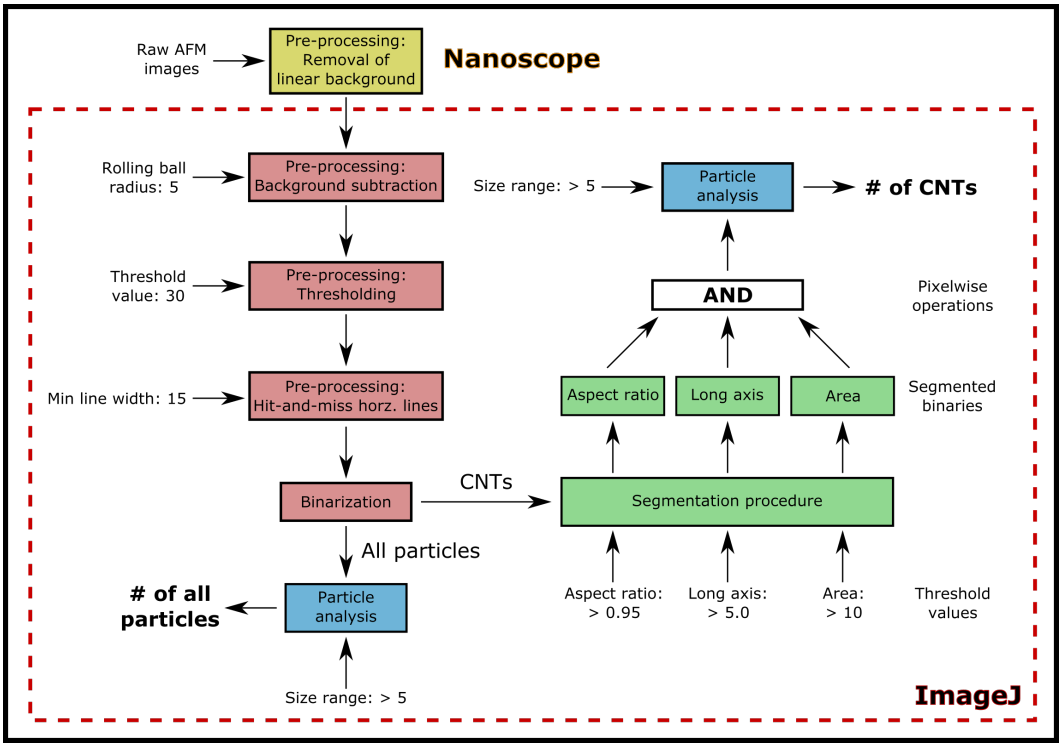


**FIGURE 6.2** Diagram of the refined analysis process in [50]. The analysis parameters related to the various process steps are highlighted.

### 6.2.1 Theoretical premises

Our objective is to tell apart tubular carbon nanotubes from debris particles of irregular shape. This can be treated as a very fundamental image analysis problem: separation of stick-like species from circular ones. Different approaches to deal with this challenge have been developed in the fields of e.g. life sciences, but no single, universal method exists. For our AFM data, an additional challenge exists since we wish to compare the numbers of each particle type in images taken prior to and following the cleaning process. In AFM, two images recorded of the same region are not completely identical: even if the exact same region can be identified in each image through, e.g., the presence of fixed references, there will always be a degree of asymmetry due to gradual wear of the AFM tip. In practice, non-linearity of the scanner will also give rise significant artifacts, such as field curvature and hysteresis, particularly for open-loop systems.

For these reasons, identification of particles based on their exact position in the image is difficult for AFM techniques. As such, we are limited to statistical evaluation of the total number of particles and MWNTs in each image, from which the detachment statistics can be inferred.

### 6.2.2 Image pre-processing

We used the topographical (height) images from our AFM measurements. First, the linear background that is inherent to the AFM images was removed in the instrument manufacturer's analysis program (Nanoscope Analysis) with a flatten thresholding tool (Fig. 6.3a).

The images were exported into a standard format (i.e. .bmp), and rotated as needed so that images recorded before and after the immersion treatment on each sample were oriented the same way. They were then cropped manually from their original $17\,\mu\mathrm{m} \times 17\,\mu\mathrm{m}$ size down to approx. $15\,\mu\mathrm{m} \times 15\,\mu\mathrm{m}$, so that the reference feature was eliminated and the image pairs reflected the same area. Following the subtraction of background with the default ImageJ "rolling paraboloid" function (Fig. 6.3b) [57], the images were then binarized via thresholding at a fixed grayscale cut-off value (Fig. 6.3c).

Subtracting the background completely from each image accommodates for best consistency and image quality following the binarization. In the absence of background subtraction, binarization with a fixed value good for one frame lead to salt-and-pepper type pixel noise in another one that corrupted the results. However, using a fixed background subtraction and thresholding parameters has the drawback that thin, faint CNTs may become fragmented in the process due to lacking contrast with the background, since the values must be made appropriate for each image frame with varying backgrounds.

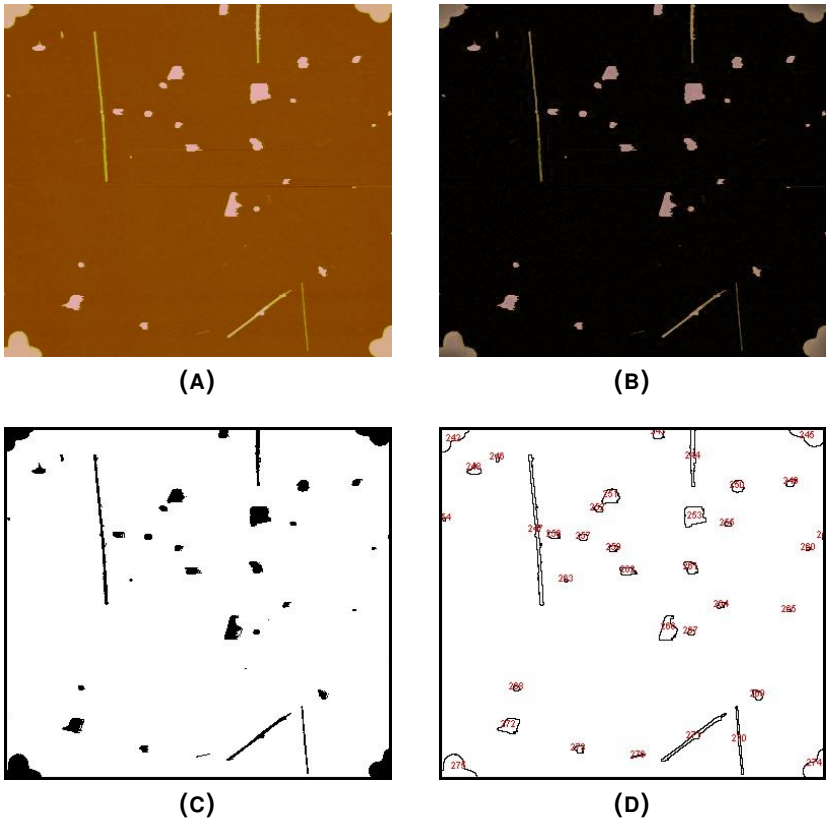


**FIGURE 6.3** Image preprocessing and analysis procedure for calculating the number of particles in an AFM frame. (a) The original AFM image with the intrinsic linear background flattened; (b) background fully subtracted; (c) thresholded binary image; (d) result of the particle count. Example taken from [49].

### 6.2.3 Identification of CNTs

CNTs were identified among the particles by their tubular shape, with characterization based on geometric parameters tabulated via image moments [40]. In principle, the process entails characterizing each particle by its area, eccentricity, orientation angle and long and short axes lengths, by approximating them as ellipsoids. While the eccentricity (aspect ratio) is the most important individual parameter in this respect, it does not guarantee a sufficiently exclusive condition alone. Together with aspect ratio, we also utilize particle's area and the length of long axis to filter out very small species that are irrelevant as CNTs. The angle data is not very useful in the segmentation process, but can be used independently to study the tube orientation.

The binary images (Fig. 6.3c) are thus given to a segmentation plug-in that maps each of these parameters into figures with magnitudes represented as gray scale values on each object. These figures can be binarized with appropriate threshold values, and the resulting binaries are then combined via pixelwise AND-operations. This results in exclusion of non-tubular species from the image frame (Fig. 6.4d), which we then take to accurately represent the CNTs within the region.

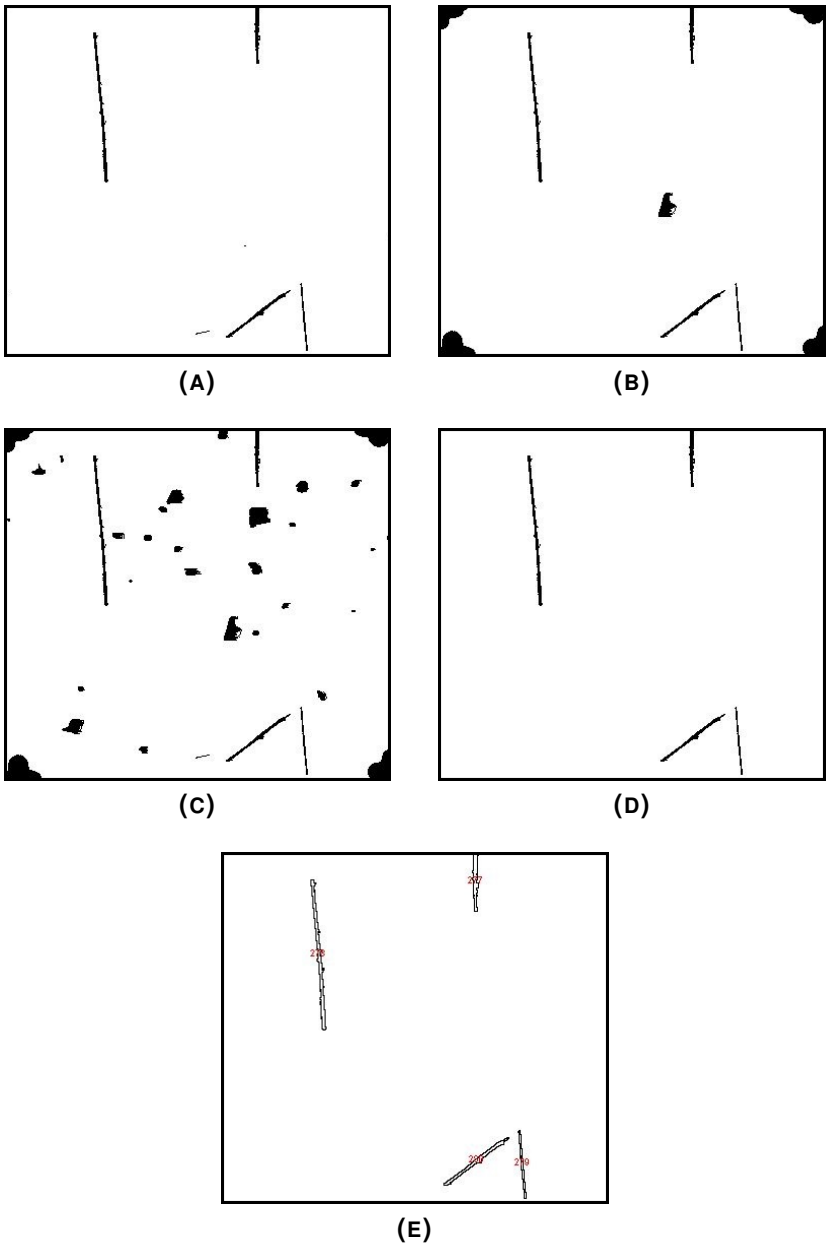


**FIGURE 6.4** Tabulating the number of CNTs in an AFM frame; segmentation and subsequent binarization of image 6.3c with respect to (a) aspect ratio, (b) long axis and (c) surface area, respectively. (d) The combined binary, formed via pixelwise AND-operations from the previous images. (e) Particle count result.

### 6.2.4 Particle & orientation analysis

The ImageJ particle analyzer is used to calculate the number of particles from the final binaries (e.g. Figs. 6.3c & 6.4d). At this point, we opt to impose a hard lower limit for the size of the objects to be incorporated in the count, to ensure that intrinsic artifacts such as surface roughness or pixel noise sometimes evident on the non-segmented binaries due to imperfect subtraction of the background does not affect the analysis. Consequentially, our analysis is thus valid only down to a certain minimum particle size.

We chose this cut-off value to be 5 pxl for our cropped AFM images sized $678\,\mathrm{pxl} \times 678\,\mathrm{pxl}$. It equals an effective particle radius of about $28\,\mathrm{nm}$ in real-world units. Considering that substantial broadening is brought about by the tip convolution effect at these scales, the true minimum radius for a particle to be included in the analysis is smaller than this. To that end, this is an acceptable condition, since the presence of individual particles this small is unlikely to be a significant hindrance for most applications.

Particle count results for the non-segmented and segmented binaries are show in Figures 6.3d & 6.4e for our example frame, respectively. We obtain the number of all particles in the frame from the non-segmented image, and that of the CNTs from the segmented one. We repeat the same process for both frames captured prior to and following the purification process. For each sample, we then compare the total numbers obtained this way to evaluate the detachment fractions for CNTs and debris particles.

The orientation-dependent detachment of carbon nanotubes can be investigated by utilizing the image moments to define the orientation of their major axes. This was done in our second work [49]; by manually comparing the segmented images taken before and after the cleaning process, detached carbon nanotubes are identified, and their orientation angles acquired from the pre-immersion data. We can then present the relative fraction of CNT detachment for as a function of tube orientation. Given that only the orientations measured from the pre-immersion images are then considered, we do not need to be concerned of indeterminacy of the orientation angles in before and after data that makes direct comparison of the orientation statistics problematic. However, care needs to be taken to take into account the initial orientation distribution of the depositions as a whole, because if there exists preferred orientation due to the spin coating [75], the detachment statistics tend to become skewed in favor of this direction.

### 6.2.5 Correction of image artifacts

A common type of image artifacts in AFM images is horizontal disturbance that arises from poor tracking of the surface. The tip is dragged in a raster pattern where the horizontal direction in the image is the fast-scan direction and the vertical direction

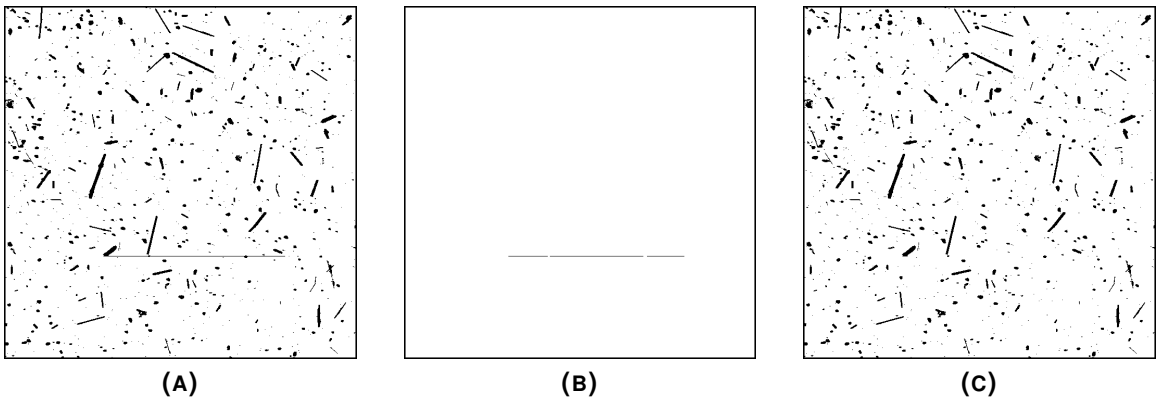


**FIGURE 6.5** An example of our approach for the elimination of horizontal disturbance: (a) the original binarized image; (b) output of the hit-and-miss analysis; (c) refined binary.

is the slow-scan direction. In the vertical, slow-scan direction, the tip may sometimes momentarily lose contact with the surface as a result of e.g. encountering a sharp irregularity even if the tracking appears good in the fast-scan direction. What results is a horizontal line defect where the pixels appear much higher than they are in reality. Proper contact is then typically retaining for the following line if the overall tracking is good.

We wanted to find a way to eliminate this type of disturbance from our images, given that it may occasionally take place even if the imaging parameters are optimized appropriately, and we cannot afford to increase the imaging time limitlessly. We accomplished this with hit-and-miss algorithm that we implemented as a separate ImageJ plugin (Fig. 6.5). It is a transform with a kernel that looks for horizontal lines in the binary, and compiles them as a separate image that can then be subtracted from the original binary. The thickness of the lines and their minimum length can be specified.

The major advantage of this approach compared to, for example, averaging of defective lines by their neighbors, is that it does not generally lead to fragmentation of carbon nanotubes, since the local thickness of the disturbance as it intersects a carbon nanotube is greater than unity. This process takes place following the binarization of the original AFM image (Fig. 6.3c). As such, it has effect on all the subsequent images. The drawback of this technique is that it may also give rise fragmentation of thin tubes that happen to be oriented horizontally. This can be inhibited by specifying a sufficiently large value for the minimum line length, but then the sensitivity to find genuine disturbance also suffers.

### 6.2.6 Caveats & limitations

I'll conclude with a brief discussion on the limitations of the analysis process as we utilize it at the time of writing this. The quality of the analysis can be discussed in terms of two quantities, precision and determinacy. The concept of precision, i.e. every particle is correctly categorized as a carbon nanotube or a particle, is non-exact in nature given that the identification is based on the geometric shape of the species that is always subject to interpretation. Determinacy or the analysis, i.e. the requirement that particles are classified systematically both prior to and following the immersion treatment, can however be evaluated in exact terms.

Technical limitations of the AFM result in particle shapes changing slightly in consecutive images. Compared to the original image, a degree of broadening is always expect in the features of the after-frame due to gradual wear of the tip, even if it is not changed. In addition, better tracking can generally be obtained in the post-immersion frames, since the initial image frames contain much more rough debris. Such topological differences lead to considerable indeterminacy between the images, even though utilizing the long axis as an additional condition for the segmentation process eases the problem.

Particularly, short tubules frequently exhibit indeterministic behavior in the analysis since their tabulated aspect ratio is greatly affected by the local imaging conditions, and given that they are of little practical interest it makes sense to always classify them as particles. We thus chose a long axis value of 5 as a low-end cut-off for the carbon nanotubes for this analysis. It corresponds to about $110\,\mathrm{nm}$ in real-world units, a rather lenient constraint, although this should not be taken as an exact measure of the tube length.

Fragmentation of carbon nanotubes in the binarization phase may take place as a consequence of improper subtraction of the background, and these instances are relatively common in the pre-immersion AFM data where the large particles tend to "shadow" neighbouring CNTs. This generally results in inflation of tube detachment in the immersion process, but the effect to the analysis is unpredictable because individual CNTs may break into several segments of different lengths. The number of these instances can be reduced by ensuring that the linear background intrinsic to the AFM images is properly thresholded away, but the thinnest CNTs are still vulnerable to fragmentation in the thresholding step. Inflation of the number of CNTs due to these fragments can be mitigated by appropriate choice of the long axis threshold value, but even then the fragmentation of tubes remains a significant factor that probably exaggerates the detachment of CNTs in our experiment.

Selection of the analysis parameters is non-exact. In particular, the cut-off for the particle size is largely arbitrary, and changing it tends to affect the overall detachment fractions. There is no definite way to choose its value, because smallest species include both genuine particles from the deposition, and artifacts such as surface features. Shifting of the recorded before and after frames with respect to one another

causes some additional indeterminacy because the exact same set of particles may not show in the image even after cropping them, but this problem is largely mitigated by imaging an individual, large frame rather than a patchwork of several small ones.

Finally, there are also cases where overlapping features cause indeterminacy. Overlapping carbon nanotubes, or tubes and particles, cannot be properly identified individually in our simple analysis, and are typically counted as a debris particle. Indeterminacy may arise when the overlapping object is removed in the purification treatment while the underlying tube is retained, and then correctly identified in the post-immersion data. Particularly in dense depositions relevant to our final study [50], CNTs frequently overlap, and are thus unable to be resolved in the analysis. As a result, some frames may even exhibit apparent increase in the number of CNTs following the immersion.

# Chapter 7

# Applications of the cleaning technique

I will conclude my presentation with an overview on the possible applications of our cleaning technique. At the moment, the scope utilizing mobile liquid interfaces for improving the quality of CNT samples is primarily limited to small-scale, in-situ applications that can be carried out by the end-user in laboratory; although the method is, in principle, fully scalable in the production of clean CNT depositions bound on silicon surfaces, its inherent on-chip nature makes it is difficult to adapt for the purposes of industrial production of CNT materials.

In this chapter, two practical applications for the technique will be demonstrated: the first one deals with Raman spectroscopy of individual carbon nanotubes, which we have already demonstrated in the second paper of this thesis [49]. Here, also more recent, unpublished results from our collaborators will be presented. The second application, nanomechanical measurements of individual CNTs, was also conceptually introduced in the previous paper, and here some practical results will be shown. Finally, I very briefly introduce the classical approach utilized in the fabrication of CNT-based electronic components via lithographic methods, to point out the potential benefits of our technique in such applications.

All of these applications showcase our technique as a method to remedy the contamination issues present in arc-discharge MWNT materials, which at present can be a major hindrance in efforts to investigate them with techniques specific to individual tubes. To that end, our technique can, at large, be applied in the preparation of samples for any practical experiment where clean CNT depositions with individual tubes are required, with the added benefit that their chemical nature is not jeopardized.

## 7.1 Raman spectroscopy

As mentioned before in chapter 2, contemporary Raman techniques are able to measure spectra from individual nanoparticles such as CNTs. In these microraman measurements, beam spot size as small as $1\ \mu\mathrm{m}$ can be routinely achieved. For CNTs,

it then becomes a challenge to prepare samples that contain an appreciable number of CNTs, and yet are sufficiently clean so that no contaminants reside in the immediate vicinity of individual tubes. This is particularly difficult for arc-discharge grown tubes due to the ever-present debris contamination; only a handful of publications exist on Raman spectroscopy of individual AD-MWNTs [53, 86, 131], and the number of tubes reported in these studies is limited.

With the help of our cleaning technique, clean samples with large numbers of individual, arc-discharge grown CNTs are easily accessible for such measurements. In our existing work [49], we already presented preliminary Raman measurements carried out on our samples (Fig. 7.1). The discernible features of this measurement include (a) small, or non-existing, D-peak (at $1300 - 1400\,\mathrm{cm}^{-1}$ range) associated with the disorder of the carbon material, and (b) very profound G-peak ($1500 - 1605\,\mathrm{cm}^{-1}$). In addition, some of the preliminary spectra also showed a degree of splitting in the G-mode. No RBM could be detected from the tubes on our samples, given the strong response from the underlaying Si substrate.

We have since carried out these measurements with the help of our collaborators in the Univ. of Witwatersrand in Johannesburg, South Africa. Additional spectra measured from samples provided by us, presented in Fig. 7.2, are qualitatively similar to the previous measurements. Both the negligible D-band and the intensity of the G-band can be associated with high degree of crystalline integrity of the arc-discharge grown CNTs, in comparison with the appreciably more disordered and defective CVD-grown materials. The remarkable features of AD-CNTs, witnessed in multiple tubes, are thus clearly highlighted.

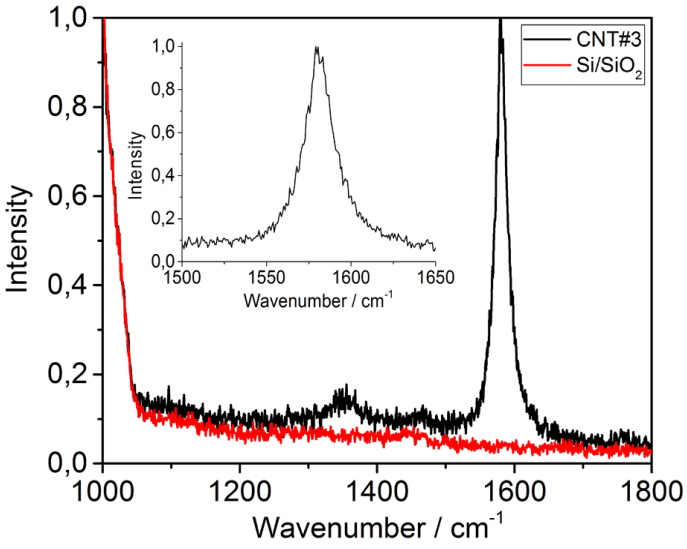


**FIGURE 7.1** Preliminary Raman spectrum recorded of an AD-MWNT on a immersion-cleaned sample. Signal recorded from the empty surface is also shown. An emphasis of the G-band is shown in the inset.

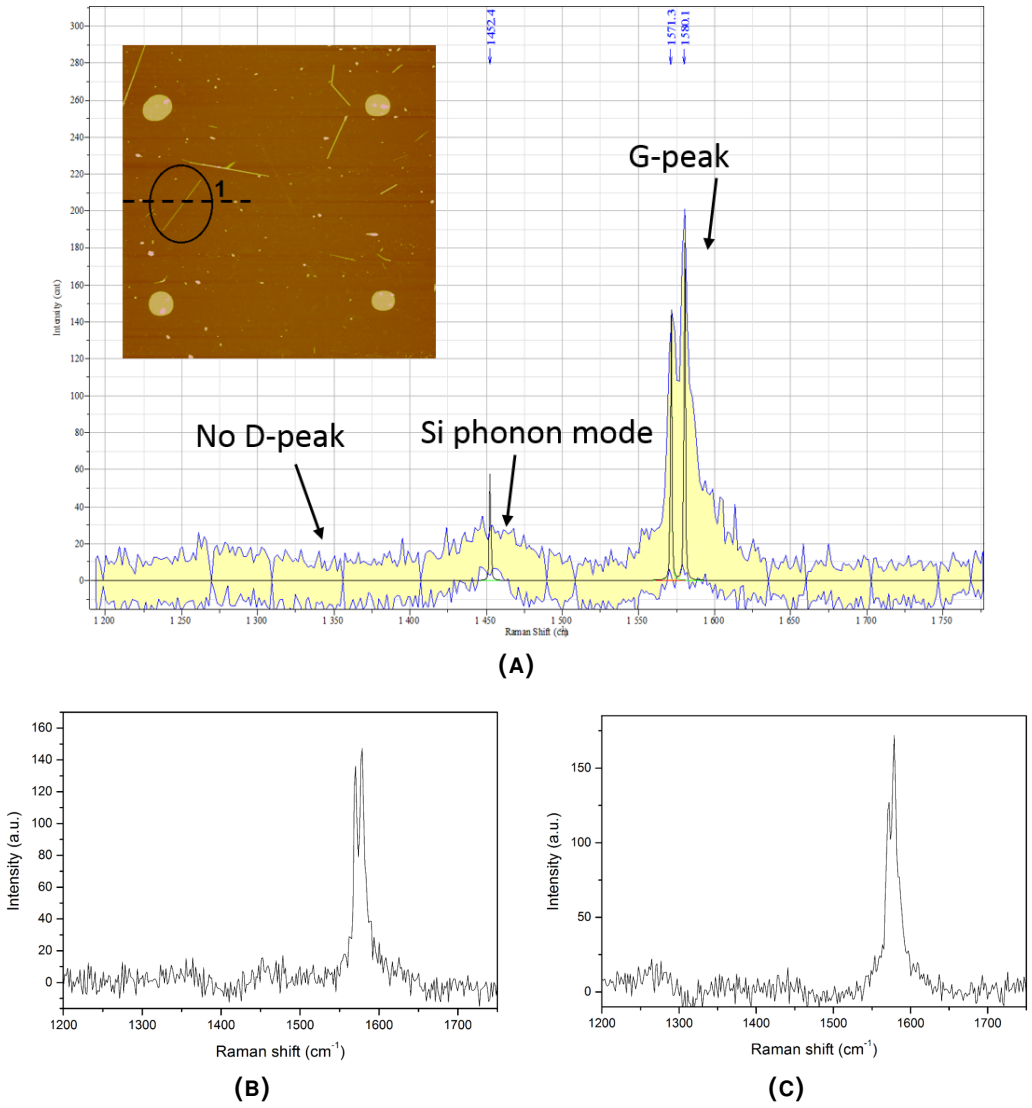


**FIGURE 7.2** (a) Raman spectrum of an arc-discharge MWNT on immersion-cleaned sample. The key features of the spectrum have been highlighted. The inset shows an AFM image of the tube in question, affirming that no debris particles exist in its immediate vicinity. (b, c) Additional Raman spectra recorded on samples provided by us from different CNTs. Splitting of the G-band is apparent for each tube. Figures courtesy of Christopher Coleman, Univ. of Witwatersrand.

What is particularly striking in the spectra of Fig. 7.2 is however the splitting of the G-band, which is very apparent and highly reproducible in several tubes. While similar splitting has been witnessed in the context of arc-discharge grown multi-walled tubes, most of the existing measurement do not show such a clear degree of separation where the mode shows two highly distinct sub-peaks; previously, subtle shoulder-like features have been observed aside the main band [86,131]. In unmodified, CVD-grown MWNTs, only weak splitting is similarly seen [15,71,97], although in these studies it is possible that ensembles of bundled CNTs, rather than individual fine tubes, were probed due to crowded nature of the depositions.

More distinct splitting of the MWNT G-band, reminiscent of the behavior in SWNTs, has been generally only witnessed at low temperatures, or as a consequence of surface-enhanced Raman conditions [39,53,131]. Although the interpretation of G-band splitting in MWNTs is far from settled, it has been suggested that the regular "graphitic" band that lies around $1580\,\mathrm{cm}^{-1}$ rises from the outer shells of the tube. Additional features could then indicate influence from the inner shells that might further be subject to splitting similar to SWNTs [53,86,131]. Our specimen thus show promise for more detailed Raman-based investigation of these questions.

## 7.2 Nanomechanical characterization

Another application devised for the immersion cleaning technique involves preparing clean CNT depositions on grooved substrates fabricated via lithographic methods. The objective is to produce dense depositions of suspended CNTs bridging over the grooves for the purposes of nanomechanical characterization via a combined SEM/AFM apparatus. The main challenge here is posed by the specialized instrument, where the range of motion afforded by the AFM probe is very limited compared to a conventional AFM with a macroscopic sample stage: the size of the accessible region is roughly $150\,\mu\mathrm{m}$ from the edge of the chip. Therefore, in order to carry out practical measurements for multiple tubes, a relatively dense deposition is required to ensure that suspended tubes can always be found on any experimental site in a random deposition. Normally, this would result in excessive debris contamination with arc-discharge synthesized material, but using our approach for purification a debris-free deposition can be obtained (Fig. 7.3).

This kind of measurements have been carried out on samples prepared by us in the Univ. of Karlstad by our collaborator, Krister Svensson. Figure 7.4a shows a CNT bridging over an etched gap being pressed by an AFM probe. In the experiment, the deflection of the AFM cantilever is monitored continuously during an downward-upward cycle: the CNT is first deflected as the tip presses upon it, and then recovers as it is withdrawn. From the deflection measurement, the force exerted on the probe can be inferred and represented as a function of the vertical displacement, i.e. a force-distance curve (Fig. 7.4b).

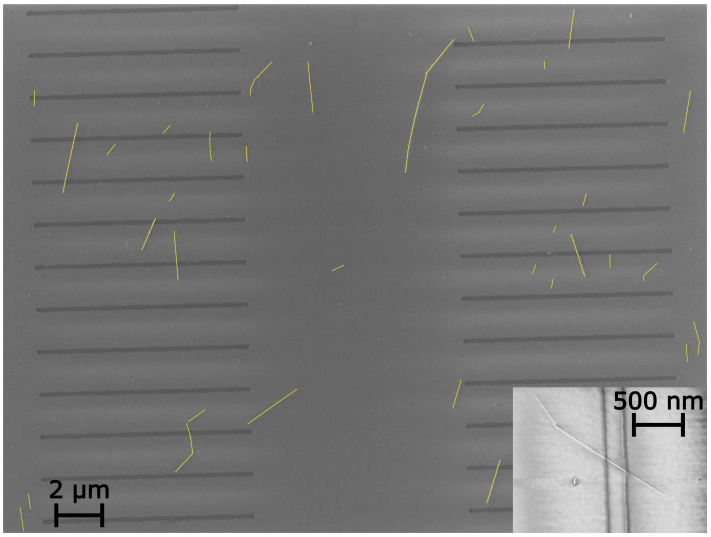


**FIGURE 7.3** SEM image of a suspended carbon nanotube deposition refined using the immersion cleaning method on an etched trench pattern. The CNTs were manually emphasized for clarity. The inset shows an individual crossover event.

The curve in Fig. 7.4b has sudden jumps and drops, particularly during the forward-pressing curve. These non-physical features reflect points where one end of the tube slipped along the surface. One can see that aside from these jumps, the continuous segments of the curve are predominantly linear, suggesting elastic bending and consecutive recovery of the tube.

The slope of the forward curve prior to the first slip can be used to estimate the force constant and, in turn, the Young's modulus of the tube. Given that neither of the tube-surface contacts has initially slipped, we may approximate the geometry as a hollow cylindrical beam clamped from both ends. The Young's modulus for such a system is

$$E = \frac{k_{\mathrm{CNT}} L^3}{192 \cdot I}, \tag{7.1}$$

where $I = {}^{\pi(D^4-d^4)}/_{64}$ is the bending moment for a hollow cylinder, $L \approx 805\,\mathrm{nm}$ the length of the suspended CNT segment (as measured from the SEM image prior to the deflection measurement), and $k_{\mathrm{CNT}}$ the force constant of the CNT that can be calculated from the slope in Fig. 7.4b. The slope itself is an effective force constant of the cantilever-CNT system, $k_{\mathrm{eff}}$, that relates to $k_{\mathrm{CNT}}$ as

$$k_{\mathrm{CNT}} = \frac{k_{\mathrm{eff}}}{1 - \frac{k_{\mathrm{eff}}}{k_{\mathrm{tip}}}}, \tag{7.2}$$

where the force constant of the cantilever ($k_{\mathrm{tip}} \approx 0.8\,{}^{\mathrm{N}}/_{\mathrm{m}}$) can be acquired via calibration curve recorded against hard surface. Taking $k_{\mathrm{eff}} \approx 0.4\,{}^{\mathrm{N}}/_{\mathrm{m}}$ from the slope of Fig. 7.4b, this yields $k_{\mathrm{CNT}} \approx 0.6\,{}^{\mathrm{N}}/_{\mathrm{m}}$. In eq. 7.1, the outer ($D \approx 16.4\,\mathrm{nm}$) diameter of the tube was acquired from close-up SEM micrographs of the suspended tube, while

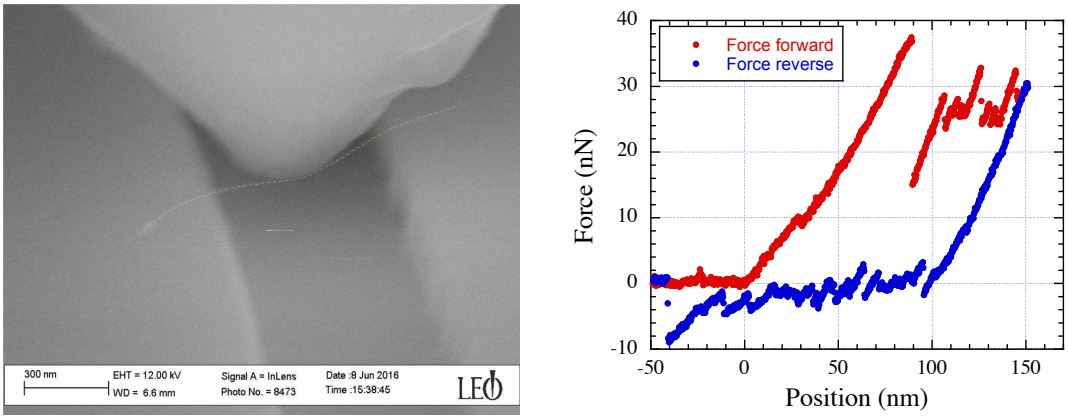


**FIGURE 7.4** (a) Scanning electron micrograph of a suspended carbon nanotube under shear stress exerted by the AFM probe. Manual dashed emphasis added to the CNT for clarity. (b) The force-distance curve recorded during the experiment. Images courtesy of Krister Svensson, Univ. of Karlstad.

the inner diameter $d$ that is very difficult to extract from SEM data was ignored (i.e. $D^4 - d^4 \approx D^4$); the result $E \sim 470\,\mathrm{GPa}$ is thus a lower-limit estimation. In addition, it should be noted that the values of $L$ and $D$ are furthermore subject to a high degree of uncertainty from the SEM estimation, and $E$ is strongly dependent on their exact values as well.

Given the slipping of the adhesion points, the data in fig. 7.4b also contains information about the tube-substrate adhesion. In the force curve, one can see that the first slip during the forward curve occurs at about $10\,\mathrm{nN}$ pressing force. This corresponds to a much higher tension force along the CNT due to the contact geometry; the value is dependent on the contact area between the tube and the surface. For the purposes of estimating the adhesion force, the diameter of the tube should be known accurately. To this end, one needs to be aware that the tubes may collapse as a result of the surface forces, i.e. their cross-sectional shape may flatten to elliptic, with height lower than the lateral width. This may have a significant impact on the adhesion.

The drawback of our technique in the context of such measurements is that with increasing width of the groove, CNTs seem to become more likely to detach, and even around $300\,\mathrm{nm}$ gap width the density of crossover tubes falls radically. As a result, reasonable number of measurements can only be obtained at relatively thin groove widths that limits the maximum curvature attainable in the experiment.

Similar experiments have been reported before for measurement of the bending stiffness of CNTs under increasing load [60–62]. In such measurements, two regimes of stiffness have been observed, where the tube first retains its crystalline integrity at low curvature, but ultimately suffers a failure at higher curvatures [60]. The point of failure signifies a transition to a rippled or buckled state, where the stiffness of the tube suddenly falls radically [62]. The specifics of the process depend on the

dimensions and crystallinity of the tube as well as the number of walls; therefore, arc-discharge grown multiwalled tubes make particularly interesting specimen for these trials given their high crystalline integrity [61].

## 7.3 Individual CNTs in electronics

The use of CNTs in electronic components is generally regarded as one of their most potent future applications. Based on the simple CNT-FET design that was introduced in chapter 2, the potential of individual CNTs as memory components [100] and biosensors [125] is well-demonstrated. More refined applications include logical gates, optoelectronics and oscillator devices [7]. For the purposes of electronic applications, the cleanliness of the carbon nanotube deposition is of utmost importance since even a minute amount of contamination would quickly degrade the device performance in large-scale manufacturing.

These troubles are also well-illustrated in laboratory-scale fabrication of individual CNT-FET structures for electric transport measurements; the basic fabrication process, based on electron beam lithography and metal evaporation, is illustrated in Fig. 7.5. First, the individual CNTs must be located on the sample surface. Usually, AFM, rather than SEM, is used, since the superior resolution accommodated by atomic force microscopy also allows for the evaluation tube diameters and lengths, as well as their overall quality. The AFM mapping is then utilized to design the electrode structure (Fig. 7.6a), which is fabricated lithographically. Figure 7.6b shows an AFM image of a complete two-probe device.

If the CNT deposition utilized in the fabrication process is populated by debris contamination, the irregular micron-scale particulates may threaten the integrity of the evaporated contact electrodes whose thickness is limited to some tens of microns. Since the line-widths of these contacts can be down to a few hundred nanometers, their fabrication is very susceptible to obstruction by surface particles. Furthermore, given that only a small part of the sample surface can ever be fully investigated in AFM, it is impossible to be aware of the contamination outside the imaging area. If such CNT-debris is sufficiently dense at the locale of several electrodes, incidental short-circuiting may take place. Finally, debris contamination is also a practical nuisance during the AFM imaging step, because on one it hand slows down the imaging process by making the surface more difficult to track, and on the other the tip wear increases due to greater surface roughness.

Given the simplicity of our cleaning technique, it provides an easy method to eliminate these issues, especially on arc-discharge grown CNT depositions where the carbonaceous debris contamination is a persistent issue. Again, we may appreciate the fact that no chemical modification of the CNTs is necessary at any point, which guarantees the preservation of their intrinsic electrical properties.

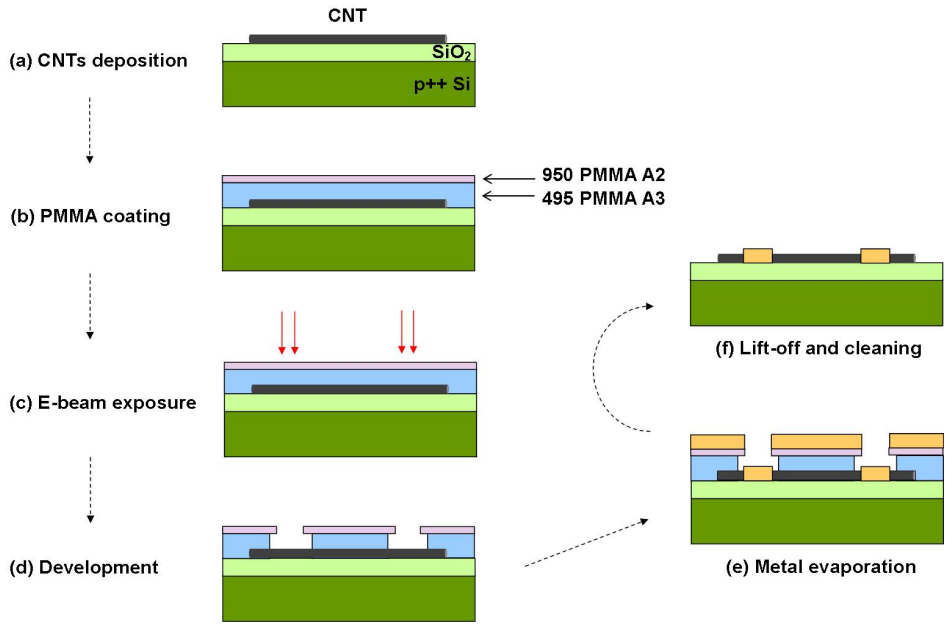


**FIGURE 7.5** The fabrication process of a practical CNT-FET on thermal $SiO_2$ substrates: (a) CNT deposition and AFM mapping; (b) spin coating of a bilayer PMMA e-beam resist; (c) e-beam exposure; (d) development – the exposed regions are dissolved; (e) evaporation of metal layer; (f) lift-off – excess resist dissolved. Figures courtesy of Peerapong Youtprayoonsak, used with permission.

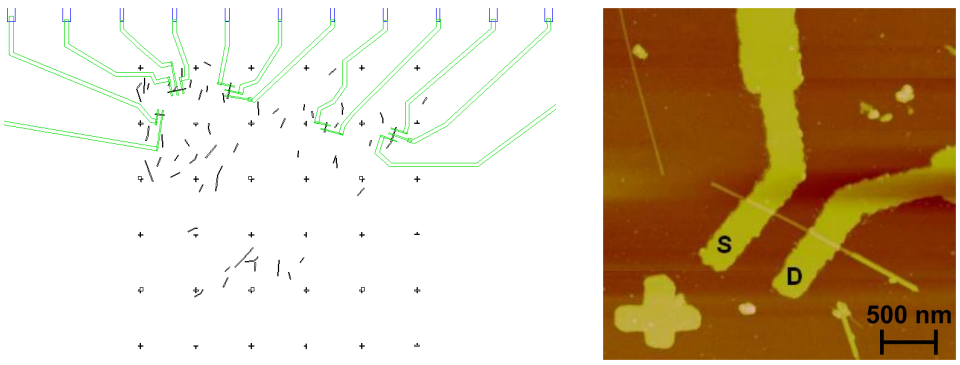


**FIGURE 7.6** (a) Contact electrode structure designed on a CNT sample based on AFM imaging: black crosses = pre-fabricated AFM references; black lines = approximate positions of the CNTs; green lines = the designed contact electrodes; blue lines = electrodes pre-fabricated as a part of the reference structure. (b) Close-up AFM image of a completed CNT-FET device.

# Chapter 8

# Conclusions

The work described in this thesis concerns the interactions of liquid interfaces with carbon-based nanoparticle matter, particularly spincoated carbon nanotube (CNT) depositions. The main objective of this thesis has been the development of a novel method for on-chip purification of arc-discharge grown carbon nanotubes, that are natively ridden with irregular, carbonaceous debris. This approach takes advantage of the interfacial interactions (surface tension) between the mobile three-phase contact line of liquid progressing along the sample surface, and the pre-deposited carbon nanotube matter. Given the vastly superior adhesion of the carbon nanotubes relative to the irregular debris, the tubes are generally retained on the surface while the debris is largely captured onto the propagating interface. The main benefit of this technique compared to other cleaning processes of CNTs is that the intrinsic chemical features of the CNTs can be fully preserved. Hydrophilic pre-treatment of the silicon substrate is, however, found essential in our experiments.

The first paper incorporated in the thesis dealt with the spreading of sessile water drops on CNT depositions. In this work, an annular depletion was realized following a spontaneous spreading process. Microscopy techniques confirmed that the depletion is due to vacation of irregular debris from the affected, ring-like area, while a large number of CNTs remain. Comparison of annular dimensions against the dynamic spreading curves confirms that the perimeter of the annulus correlates with the end-point of the drop-spreading, suggesting that the depletion effect is strictly due to a physical interaction at the interface of the spreading droplet. This gives rise a radially enhancing depletion effect that is most intense close to the outer annular perimeter, corresponding to deceleration of the contact line.

Experiments with compound droplets consisting of dilute isopropyl alcohol solutions lead to overall narrower drops, i.e. higher contact angles, with annuli that were both narrower and thinner. Together with changes in the fine-structure of the annuli, it is thus implied that improved detergency of the alcohol solution lead to stronger initial particle detachment, and faster subsequent pinning of the contact line due to the detached particles accruing there.

These finding motivated our second study, where we introduced the immersion

purification concept for practical CNT samples. Liquid contact line sweeping over the entire sample surface gave rise a substantial and uniform cleaning effect as visualized optically. We used comparative atomic force microscopy (AFM) to infer the number of debris particles and carbon nanotubes on the sample surfaces prior to and following the immersion process. For this purpose, a dedicated segmentation and analysis process was developed, which was thoroughly discussed in its own chapter.

We found that our cleaning process provides effective means for selective detachment of irregular debris from the arc-discharge synthesized CNT material deposited via spin coating. The detachment fractions for carbon nanotubes were on average down to $10\,\%$, while about a half of the debris particles could generally be removed. Analysis of the CNT detachment as a function of their initial angular orientation revealed that tubes oriented parallel to the propagating interface were far more likely to be vacated from the surface than perpendicular ones.

In our third work, we sought to deepen our understanding of the factors influencing the cleaning process on single-particle level. For this purpose, a refined experimental process was devised, based on a flow chamber where contamination of the immersed sample by the detached particles or chemical residues can be avoided, along with improvements of the AFM imaging and analysis methodology. With the help of the methodological improvements, we found that the detachment fractions could be improved significantly, up to $90\,\%$ for the debris particles, although the detachment of CNTs also increased substantially. In addition, we were now able to confirm a correlation between the detachment and velocity of the liquid interface, which could not be witnessed in the previous work.

Thanks to the refined methodology, we were also able to carry out experiments in ionic and acidic immersion solutions without excessive contamination issues. These experiments show that the effects of the solution chemistry are very limited, at least in the context of existing detachment and retention studies of CNTs reported for bulk liquid environments; to the detachment process at the air-liquid interface, physical interactions dominate the behavior. Furthermore, additional trials were made with with double-walled carbon nanotube material grown with the chemical vapor deposition (CVD) method. In the experiment, depositions based on the CVD-tubes behaved qualitatively similar to the arc-discharge synthesized ones. The extent of CNT detachment was however greater than anticipated, which we believe to be related to strong cohesive interactions and interconnectedness among these appreciable longer and more flexible tubes.

The theoretical interpretation of the detachment process was given in the context of an existing model developed for interfacial detachment of spherical microcolloids due to the surface tension force. In addition, the role of the elastic shear force resulting from deformation of the contact line in the immediate vicinity of an adhered particle was discussed. Particle adhesion is best described through the so-called DLVO-theory, that combines retarded van der Waals molecular adhesion with screening due to

electrostatic double layer in an electrolyte solution. We find that the essential feature of our experiments, selectivity of the detachment to irregular debris particles, can be qualitatively understood based on this model, although quantitative applicability to nanoscale species such as CNTs raises many questions. Furthermore, the velocity dependence verified in our last paper is in general agreement with existing experimental works on the microspheres.

Finally, we introduced some concrete applications for CNT samples purified through our technique, which benefit from its chemically inactive nature. These applications (microraman measurements of individual CNTs & nanomechanical experiments of suspended tubes) were introduced as a part of our second paper, and some additional results from our collaborators have been presented in this thesis. With such potential use, the liquid interface cleaning technique holds promise as means to remedy the contamination problem ever-present in arc-discharge grown CNTs, for the benefit of top-down, on-chip applications.

# Bibliography


[1] ABRAHAMSON, J., WILES, P. G., AND RHOADES, B. L., *Structure of carbon fibres found on carbon arc anodes*. Carbon **37** (1999) 1873–1874. Print of a conference proceeding from 1979, URL http://dx.doi.org/10.1016/S0008-6223(99)00199-2.

[2] AHLSKOG, M., HERRANEN, O., JOHANSSON, A., LEPPÄNIEMI, J., AND MTSUKO, D., *Electronic transport in intermediate sized carbon nanotubes*. Phys. Rev. B **79** (2009) 155408. URL http://dx.doi.org/10.1103/PhysRevB.79.155408.

[3] ALI, K., SHAH, A., BILAL, S., AND SHAH, A., *Surface tensions and thermodynamic parameters of surface formation of aqueous salt solutions: III. Aqueous solution of KCl, KBr and KI*. Colloids Surf., A **337** (2009) 194–199. URL http://dx.doi.org/10.1016/j.colsurfa.2008.12.023.

[4] ARAMRAK, S., FLURY, M., AND HARSH, J. B., *Detachment of Deposited Colloids by Advancing and Receding Air-Water Interfaces*. Langmuir **27** (2011) 9985–9993. URL http://dx.doi.org/10.1021/la201840q.

[5] ARAMRAK, S., FLURY, M., HARSH, J. B., ZOLLARDS, R. L., AND DAVIS, H. P., *Does Colloid Shape Affect Detachment of Colloids by a Moving Air-Water Interface?* Langmuir **29** (2013) 5770–5780. URL http://dx.doi.org/10.1021/la400252q.

[6] ARNOLD, M. S., GREEN, A. A., HULVAT, J. F., STUPP, S. I., AND HERSAM, M. C., *Sorting carbon nanotubes by electronic structure using density differentiation*. Nat. Nanotechnol. **1** (2006) 60–65. URL http://dx.doi.org/10.1038/nnano.2006.52.

[7] AVOURIS, P., CHEN, Z., AND PEREBEINOS, V., *Carbon-based electronics*. Nat. Nanotechnol. **2** (2007) 605–615. URL http://dx.doi.org/10.1038/nnano.2007.300.

[8] BAJWA, N., LI, X., AJAYAN, P. M., AND VAJTAI, R., *Mechanisms for Catalytic CVD Growth of Multiwalled Carbon Nanotubes*. J. Nanosci. Nanotechnol. **8** (2008) 6054–6064. URL http://dx.doi.org/10.1166/jnn.2008.SW02.

[9] BENSIMON, A., SIMON, A., CHIFFAUDEL, A., CROQUETTE, V., HESLOT, F., AND BENSIMON, D., *Alignment and sensitive detection of DNA by a moving interface*. Science **265** (1994) 2096–2098. URL http://dx.doi.org/10.1126/science.7522347.

[10] BENSIMON, D., SIMON, A. J., CHIFFAUDEL, A., CROQUETTE, V., AND BENSIMON, A., *Stretching DNA with a Receding Meniscus: Experiments and Models*. Phys. Rev. Lett. **74** (1995) 4754–4757. URL http://dx.doi.org/10.1103/PhysRevLett.74.4754.

[11] BERG, J. C., *An Introduction to Interfaces & Colloids: The Bridge to Nanoscience* (World Scientific, Singapore, 2010).

[12] BETHUNE, D. S., KIANG, C. H., VRIES, M. S. D., GORMAN, G., SAVOY, R., VAZQUEZ, J., AND BEYERS, R., *Cobalt-catalysed growth of carbon nanotubes with single-atomic-layer walls*. Nature **363** (1993) 605–607. URL http://dx.doi.org/10.1038/363605a0.

[13] BHUSHAN, B., *Springer Handbook of Nanotechnology* (Springer, Berlin Heidelberg, 2006), 2nd ed., pp. 1387–1388. Ed. B. Bhushan.

[14] BLAKE, T. D., *The physics of moving wetting lines*. J. Colloid Interface Sci. **299** (2006) 1–13. URL http://dx.doi.org/10.1016/j.jcis.2006.03.051.

[15] BOKOBZA, L., BRUNEEL, J.-L., AND COUZI, M., *Raman spectroscopic investigation of carbon-based materials and their composites. Comparison between carbon nanotubes and carbon black*. Chem. Phys. Lett. **590** (2013) 153–159. URL http://dx.doi.org/10.1016/j.cplett.2013.10.071.

[16] BOKOVA, S. N., OBRAZTSOVA, E. D., GREBENYUKOV, V. V., ELUMEEVA, K. V., ISHCHENKO, A. V., AND KUZNETSOV, V. L., *Raman diagnostics of multi-wall carbon nanotubes with a small wall number*. Phys. Status Solidi B **247** (2010) 2827–2830. URL http://dx.doi.org/10.1002/pssb.201000237.

[17] BOLOTOV, V. V., KAN, V. E., KNYAZEV, E. V., KORUSENKO, P. M., NESOV, S. N., STENKIN, Y. A., SACHOV, V. A., AND PONOMAREVA, I. V., *An observation of the radial breathing mode in the Raman spectra of CVD-grown multi-wall carbon nanotubes*. New Carbon Mater. **30** (2015) 385–390. URL http://dx.doi.org/10.1016/S1872-5805(15)60197-4.

[18] BONN, D., EGGERS, J., INDEKEU, J., MEUNIER, J., AND ROLLEY, E., *Wetting and spreading*. Rev. Mod. Phys. **81** (2009) 739–805. URL http://dx.doi.org/10.1103/RevModPhys.81.739.

[19] CHARLIER, J.-C., BLASE, X., AND ROCHE, S., *Electronic and transport properties of nanotubes*. Rev. Mod. Phys. **79** (2007) 677–732. URL http://dx.doi.org/10.1103/RevModPhys.79.677.

[20] CHATTERJEE, N. AND FLURY, M., *Effect of Particle Shape on Capillary Forces Acting on Particles at the Air-Water Interface*. Langmuir **29** (2013) 7903–7911. URL http://dx.doi.org/10.1021/la4017504.

[21] CHEN, K. L. AND ELIMELECH, M., *Relating Colloidal Stability of Fullerene ($c_{60}$) Nanoparticles to Nanoparticle Charge and Electrokinetic Properties*. Environ. Sci. Technol. **43** (2009) 7270–7276. URL http://dx.doi.org/10.1021/es900185p.

[22] CHOI, K., EOM, T.-J., AND LEE, C., *Comparison of the removal efficiency for organic contaminants on silicon wafers stored in plastic boxes between UV/$O_3$ and ECR oxygen plasma cleaning methods*. Thin Solid Films **435** (2003) 227–231. Proceedings of the Joint International Plasma Symposium of the 6th APCPST, the 15th SPSM and the 11th Kapra Symposia, URL http://dx.doi.org/10.1016/S0040-6090(03)00329-8.

[23] CUMINGS, J. AND ZETTL, A., *Localization and Nonlinear Resistance in Telescopically Extended Nanotubes*. Phys. Rev. Lett. **93** (2004) 086801. URL http://dx.doi.org/10.1103/PhysRevLett.93.086801.

[24] DABROWSKI, J. AND MUSSIG, H.-J., *Silicon surfaces and formation of interfaces - Basic science in the industrial world* (World Scientific Publishing Co., Singapore, 2000), p. 352.

[25] DEEGAN, R., BAKAJIN, O., DUPONT, T. F., HUBER, G., NAGEL, S. R., AND WITTEN, T. A., *Capillary flow as the cause of ring stains from dried liquid drops*. Nature **389** (1997) 827–829. URL http://dx.doi.org/10.1038/39827.

[26] DEEGAN, R. D., BAKAJIN, O., DUPONT, T. F., HUBER, G., NAGEL, S. R., AND WITTEN, T. A., *Contact line deposits in an evaporating drop*. Phys. Rev. E **62** (2000) 756–765. URL http://dx.doi.org/10.1103/PhysRevE.62.756.

[27] DEGENNES, P. G., *Wetting: statics and dynamics*. Rev. Mod. Phys. **57** (1985) 827–863. URL http://dx.doi.org/10.1103/RevModPhys.57.827.

[28] DEGENNES, P. G., BROCHARD-WYART, F., AND QUERE, D., *Capillarity and Wetting Phenomena: Drops, Bubbles, Pearls, Waves* (World Scientific Publishing Co. Ptc. Ltd., 2010).

[29] DONALDSON, S. H., RØYNE, A., KRISTIANSEN, K., RAPP, M. V., DAS, S., GEBBIE, M. A., LEE, D. W., STOCK, P., VALTINER, M., AND ISRAELACHVILI,

J., *Developing a General Interaction Potential for Hydrophobic and Hydrophilic Interactions*. Langmuir **31** (2015) 2051–2064.

[30] DRESSELHAUS, M. S., DRESSELHAUS, G., AND EKLUND, P. C., *Science of Fullerenes and Carbon Nanotubes* (Academic Press, New York, 1996).

[31] DRESSELHAUS, M. S., DRESSELHAUS, G., JORIO, A., FILHO, A. G. S., AND SAITO, R., *Raman spectroscopy on isolated single wall carbon nanotubes*. Carbon **40** (2002) 2043–2061. URL http://dx.doi.org/10.1016/S0008-6223(02)00066-0.

[32] EATEMADI, A., DARAEE, H., KARIMKHANLOO, H., KOUHI, M., ZARGHAMI, N., AKBARZADEH, A., ABASI, M., HANIFEHPOUR, Y., AND JOO, S. W., *Carbon nanotubes: properties, synthesis, purification, and medical applications*. Nanoscale Res. Lett. **9** (2014) 1–13. URL http://dx.doi.org/10.1186/1556-276X-9-393.

[33] EKLUND, P., AJAYAN, P., BLACKMON, R., HART, A. J., KONG, J., PRADHAN, B., RAO, A., AND RINZLER, A., *WTEC Panel Report on International Assessment of Research and Development of Carbon Nanotube Manufacturing and Applications*, ONLINE (2007). http://www.wtec.org/cnm/CNM_final_report.pdf (retrieved 2016/10/13).

[34] *Dropsnake Drop Shape Analysis for ImageJ*, ONLINE (2013). Documentation & plug-in available at: http://bigwww.epfl.ch/demo/dropanalysis/ (retrieved 2016/9/20).

[35] FERCHER, A. F., DREXLER, W., HITZENBERGER, C. K., AND LASSER, T., *Optical coherence tomography - principles and applications*. Reports on Progress in Physics **66** (2003) 239. URL http://stacks.iop.org/0034-4885/66/i=2/a=204.

[36] FREITAG, M., *Carbon Nanotubes: Properties and Applications* (CRC Press, Taylor & Francies Group, 2006), pp. 96–102. Ed. M. J. O'Connell.

[37] GADDAM, S., KAZI, H., DONG, B., DRIVER, M., AND KELBER, J., *Surface cleaning for enhanced adhesion to packaging surfaces: Effect of oxygen and ammonia plasma*. J. Vac. Sci. Technol. A **33** (2015). URL http://dx.doi.org/10.1116/1.4902334.

[38] GHAVAMIAN, A., RAHMANDOUST, M., AND ÖCHSNER, A., *On the determination of the shear modulus of carbon nanotubes*. Compos. Part B-ENG **44** (2013) 52–59. URL http://dx.doi.org/10.1016/j.compositesb.2012.07.040.

[39] GOHIL, S. AND GHOSH, S., *Surface enhanced Raman scattering from multiwalled carbon nanotubes at low temperatures*. Appl. Phys. Lett. **96** (2010). URL http://dx.doi.org/10.1063/1.3374862.

[40] GONZALES, R. C. AND WOODS, R. E., *Digital Image Processing, International Edition* (Prentice-Hall, Inc., 2002), 2nd ed.

[41] GOODELL, B., XIE, X., QIAN, Y., GEOFFREY, D., PETERSON, M., AND JELLISON, J., *Carbon Nanotubes Produced from Natural Cellulosic Materials*. J. Nanosci. Nanotechnol. **8** (2008) 2472–2474. URL http://dx.doi.org/10.1166/jnn.2008.235.

[42] GREGORY, J., *Approximate expressions for retarded van der waals interaction*. J. Colloid Interface Sci. **83** (1981) 138–145. URL http://dx.doi.org/10.1016/0021-9797(81)90018-7.

[43] GUO, T., NIKOLAEV, P., THESS, A., COLBERT, D. T., AND SMALLEY, R. E., *Catalytic growth of single-walled manotubes by laser vaporization*. Chem. Phys. Lett. **243** (1995) 49–54. URL http://dx.doi.org/10.1016/0009-2614(95)00825-O.

[44] H. N. WALTERNBURG, J. T. Y., *Surface Chemistry of Silicon*. Chem. Rev. **95** (1995) 1589–1673. URL http://dx.doi.org/10.1021/cr00037a600.

[45] HARDY, W. B., *III. The spreading of fluids on glass*. Phil. Mag. Series 6 **38** (1919) 49–55. URL http://dx.doi.org/10.1080/14786440708635928.

[46] HATA, K., FUTUBA, D. N., MIZUNO, K., NAMAI, T., YUMURA, M., AND IIJIMA, S., *Water-Assisted Highly Efficient Synthesis of Impurity-Free Single-Walled Carbon Nanotubes*. Science **306** (2004) 1362–1364. URL http://dx.doi.org/10.1126/science.1104962.

[47] HERMANSSON, K., LINDBERG, U., HÖK, B., AND PALMSKOG, G., *Wetting properties of silicon surfaces*, in *Solid-State Sensors and Actuators, 1991. Digest of Technical Papers, TRANSDUCERS '91., 1991 International Conference on* (1991), pp. 193–196. URL http://dx.doi.org/10.1109/SENSOR.1991.148835.

[48] HOKKANEN, M. J., *Hiilinanoputkien käyttö transistorikomponenteissa: hiilinanoputkinäytteiden laadun parantaminen, transistorikomponettien valmistus sekä niiden sähköiset ominaisuudet*, Master's thesis, University of Jyväskylä (2011).

[49] HOKKANEN, M. J., LAUTALA, S., DONGKAI, S., TURPEINEN, T., KOIVISTOINEN, J., AND AHLSKOG, M., *On-chip purification via liquid immersion of arc-discharge synthesized multiwalled carbon nanotubes*. Appl. Phys. A **122** (2016) 1–8. URL http://dx.doi.org/10.1007/s00339-016-0154-0.

[50] HOKKANEN, M. J., LAUTALA, S., FLAHAUT, E., AND AHLSKOG, M., *Experimental studies on the detachment of multi-walled carbon nanotubes by a mobile liquid interface*, Langmuir (2016) [SUBMITTED].

[51] HOKKANEN, M. J., LEHTO, R., TAKALO, J., SALMELA, J., HAAVISTO, S., BYKOV, A., MYLLYLÄ, R., TIMONEN, J., AND AHLSKOG, M., *Depletion of carbon nanotube depositions and tube realignment in the spreading of sessile drops*. Colloids Surf., A **482** (2015) 624–630. URL http://dx.doi.org/10.1016/j.colsurfa.2015.06.055.

[52] HOU, P.-X., LIU, C., AND CHENG, H.-M., *Purification of carbon nanotubes*. Carbon **46** (2008) 2003–2025. URL http://dx.doi.org/10.1016/j.carbon.2008.09.009.

[53] HOU, X., SHENG, L., YU, L., AN, K., ANDO, Y., AND ZHAO, X., *Surface-enhanced Raman spectra of individual multiwalled carbon nanotubes with small innermost diameters*. J. Raman Spectrosc. **43** (2012) 1381–1384. URL http://dx.doi.org/10.1002/jrs.4092.

[54] HU, H. AND LARSON, R. G., *Marangoni Effect Reverses Coffee-Ring Depositions*. J. Phys. Chem. B **110** (2006) 7090–7094. URL http://dx.doi.org/10.1021/jp0609232.

[55] IIJIMA, S., *Helical microtubules of graphitic carbon*. Nature **354** (1991) 56–58. URL http://dx.doi.org/10.1038/354056a0.

[56] IIJIMA, S. AND ICHIHASHI, T., *Single-shell carbon nanotubes of 1-nm diameter*. Nature **363** (1993) 603–605. URL http://dx.doi.org/10.1038/363603a0.

[57] *ImageJ Documentation Wiki: Subtract background*, ONLINE (2010). http://imagejdocu.tudor.lu/doku.php?id=gui:process:subtract_background (retrieved 2016/10/19).

[58] ISRAELACHVILI, J. N., *Intermolecular and surface forces* (Academic Press, 1991), 2nd ed., pp. 260–266.

[59] Izvestiya Akademii Nauk SSSR, Metals **3** (1982) 12–17. (AUTHOR & TITLE UNKNOWN).

[60] JACKMAN, H., KRAKHMALEV, P., AND SVENSSON, K., *Measurements of the critical strain for rippling in carbon nanotubes*. Appl. Phys. Lett. **98** (2011). URL http://dx.doi.org/10.1063/1.3587613.

[61] JACKMAN, H., KRAKHMALEV, P., AND SVENSSON, K., *Large variations in the onset of rippling in concentric nanotubes*. Applied Physics Letters **104** (2014). URL http://dx.doi.org/10.1063/1.4861605.

[62] JACKMAN, H., KRAKHMALEV, P., AND SVENSSON, K., *Mechanical behavior of carbon nanotubes in the rippled and buckled phase*. J. Appl. Phys. **117** (2015). URL http://dx.doi.org/10.1063/1.4913701.

[63] JAVEY, A., GUO, J., WANG, Q., LUNDSTROM, M., AND DAI, H., *Ballistic carbon nanotube field-effect transistors*. Nature **424** (2003) 654–657. URL http://dx.doi.org/10.1038/nature01797.

[64] JOANNY, J. F. AND DEGENNES, P. G., *A model for contact angle hysteresis*. J. Chem. Phys. **81** (1984) 552–562. URL http://dx.doi.org/10.1063/1.447337.

[65] KABZA, K. G., GESTWICKI, J. E., AND MCGRATH, J. L., *Contact Angle Goniometry as a Tool for Surface Tension Measurements of Solids, Using Zisman Plot Method. A Physical Chemistry Experiment*. J. Chem. Educ. **77** (2000) 63. URL http://dx.doi.org/10.1021/ed077p63.

[66] KAMIENIECKI, E. AND FOGGIATO, G. J., *Handbook of Semiconductor Wafer Cleaning Technology: Science, Technology and Applications* (Noyes Publications, Westwood, New Jersey, 1993), pp. 519–522. Ed. W. Kern.

[67] KATAURA, H., KUMAZAWA, Y., MANIWA, Y., UMEZU, I., SUZUKI, S., OHTSUKA, Y., AND ACHIBA, Y., *Optical properties of single-wall carbon nanotubes*. Synthetic Metals **103** (1999) 2555–2558. URL http://dx.doi.org/10.1016/S0379-6779(98)00278-1.

[68] KAYA, S., RAJAN, P., DASARI, H., INGRAM, D. C., JADWISIENCZAK, W., AND RAHMAN, F., *A Systematic Study of Plasma Activation of Silicon Surfaces for Self Assembly*. ACS Appl. Mater. Interfaces **7** (2015) 25024–25031. URL http://dx.doi.org/10.1021/acsami.5b08358.

[69] KHRIPIN, C. Y., ZHENG, M., AND JAGOTA, A., *Deposition and meniscus alignment of DNA-CNT on a substrate*. J. Colloid Interface Sci. **330** (2009) 255–265. URL http://dx.doi.org/10.1016/j.jcis.2008.10.073.

[70] KROTO, H. W., HEATH, J. R., O'BRIEN, S. C., CURL, R. F., AND SMALLEY, R. E., *$C_{60}$: Buckminsterfullerene*. Nature **318** (1985) 162–163. URL http://dx.doi.org/10.1038/318162a0.

[71] KUZNETSOV, V. L., BOKOVA-SIROSH, S. N., MOSEENKOV, S. I., ISHCHENKO, A. V., KRASNIKOV, D. V., KAZAKOVA, M. A., ROMANENKO, A. I., TKACHEV, E. N., AND OBRAZTSOVA, E. D., *Raman spectra for characterization of defective CVD multi-walled carbon nanotubes*. Phys. Status Solidi B **251** (2014) 2444–2450. URL http://dx.doi.org/10.1002/pssb.201451195.

[72] LAZOUSKAYA, V., WANG, L. P., OR, D., WANG, G., CAPLAN, J. L., AND JIN, Y., *Colloid mobilization by fluid displacement fronts in channels*. J. Colloid Interface Sci. **406** (2013) 44–50. URL http://dx.doi.org/10.1016/j.jcis.2013.05.078.

[73] LEENAARS, A. F. M., *A new approach to the removal of sub-micron particles from solid (silicon) surfaces*, in *Particles on surfaces 1: Detection, Adhesion, and Removal*, edited by K. Mittal, Fine Particle Society (Plenum Press, New York, 1988), pp. 361–372. Proceedings of a symposium held in conjunction with the Seventeenth Annual Meeting of the Fine Particle Society.

[74] LEENAARS, A. F. M. AND O'BRIEN, S. B. G., *Particle removal from silicon substrates using surface tension forces*. Philips J. Res. **44** (1989) 183–209.

[75] LEMIEUX, M. C., ROBERTS, M., BARMAN, S., JIN, Y. W., KIM, J. M., AND BAO, Z., *Self-Sorted, Aligned Nanotube Networks for Thin-Film Transistors*. Science **321** (2008) 101–104. URL http://dx.doi.org/10.1126/science.1156588.

[76] MA, X., WIGINGTON, B., AND BOUCHARD, D., *Fullerene $c_{60}$: Surface Energy and Interfacial Interactions in Aqueous Systems*. Langmuir **26** (2010) 11886–11893. URL http://dx.doi.org/10.1021/la101109h.

[77] MANUKYAN, S., SAUER, H. M., ROISMAN, I. V., BALDWIN, K. A., FAIRHURST, D. J., LIANG, H., VENZMER, J., AND TROPEA, C., *Imaging internal flows in a drying sessile polymer dispersion drop using Spectral Radar Optical Coherence Tomography (SR-OCT)*. J. Colloid Interface Sci. **395** (2013) 287–293. URL http://dx.doi.org/10.1016/j.jcis.2012.11.037.

[78] MARTINEZ, N., *Wettability of Silicon, Silicon Dioxide and Organosilicate Glass*, Master's thesis, University of North Texas (2009).

[79] MENDE, G., FINSTER, J., FLAMM, D., AND SCHULZE, D., *Oxidation of etched silicon in air at room temperature; Measurements with ultrasoft X-ray photoelectron spectroscopy (ESCA) and neutron activation analysis*. Surf. Sci. **128** (1983) 169–175. URL http://dx.doi.org/10.1016/S0039-6028(83)80024-7.

[80] MINTMIRE, J. W., DUNLAP, B. I., AND WHITE, C. T., *Are fullerene tubules metallic?* Phys. Rev. Lett. **68** (1992) 631–634. URL http://dx.doi.org/10.1103/PhysRevLett.68.631.

[81] MIZUNO, K., ISHII, J., KISHIDA, H., HAYAMIZU, Y., YASUDA, S., FUTABA, D. N., YUMURA, M., AND HATA, K., *A black body absorber from vertically aligned single-walled carbon nanotubes*. Proc. Natl. Acad. Sci. USA **106** (2009) 6044–6047. URL http://dx.doi.org/10.1073/pnas.0900155106.

[82] MOISALA, A., NASIBULIN, A. G., AND KAUPPINEN, E. I., *The role of metal nanoparticles in the catalytic production of single-walled carbon nanotubes-a review*. J. Phys. Condens. Matter **15** (2003) S3011. URL http://stacks.iop.org/0953-8984/15/i=42/a=003.

[83] MTSUKO, D., KOSHIO, A., YUDASAKA, M., IIJIMA, S., AND AHSLKOG, M., *Measurements of the transport gap in semiconducting multiwalled carbon nanotubes with varying diameter and length*. Phys. Rev. B **91** (2015) 195426. URL http://dx.doi.org/10.1103/PhysRevB.91.195426.

[84] MURR, L. E., BANG, J. J., ESQUIVEL, E. V., GUERRERO, P. A., AND LOPEZ, D. A., *Carbon Nanotubes, Nanocrystal Forms, and Complex Nanoparticle Aggregates in common fuel-gas combustion sources and the ambient air*. J. Nanopart. Res. **6** (2004) 241–251. URL http://dx.doi.org/10.1023/B:NANO.0000034651.91325.40.

[85] MYLLYPERKIÖ, P., HERRANEN, O., RINTALA, J., JIANG, H., MUDIMELA, P. R., ZHU, Z., NASIBULIN, A. G., JOHANSSON, A., KAUPPINEN, E. I., AHLSKOG, M., AND PETTERSON, M., *Femtosecond Four-Wave-Mixing Spectroscopy of Suspended Individual Semiconducting Single-Walled Carbon Nanotubes*. ACS Nano **4** (2010) 6780–6786. URL http://dx.doi.org/10.1021/nn1015067.

[86] NANOT, S., MILLOT, M., RAQUET, B., BROTO, J.-M., MAGREZ, A., AND GONZALEZ, J., *Doping dependence of the G-band Raman spectra of an individual multiwall carbon nanotube*. Physica E **42** (2010) 2466–2470. URL http://dx.doi.org/10.1016/j.physe.2010.06.006.

[87] *Legendary Swords' Sharpness, Strength From Nanotubes, Study Says*, ONLINE (2006). http://news.nationalgeographic.com/news/2006/11/061116-nanotech-swords.html (retrieved 2016/10/13).

[88] *The Nobel Prize in Physics 1986*, ONLINE (2016). http://www.nobelprize.org/nobel_prizes/physics/laureates/1986/ (retrieved 2016/9/20).

[89] OBERLIN, A., ENDO, M., AND KOYAMA, T., *Filamentous growth of carbon through benzene decomposition*. Journal of Crystal Growth **32** (1976) 335–349. URL http://dx.doi.org/10.1016/0022-0248(76)90115-9.

[90] OSBORNE, K. L. I., *Temperature-Dependence of the Contact Angle of Water on Graphite, Silicon and Gold*, Master's thesis, Worchester Polytechnic Institute (2009).

[91] PENG, B., LOCASCIO, M., ZAPOL, P., LI, S., MIELKE, S. L., SCHATZ, G. C., AND ESPINOSA, H. D., *Measurements of near-ultimate strength for multiwalled*

*carbon nanotubes and irradiation-induced crosslinking improvements*. Nat. Nanotechnol. **3** (2008) 626–631. URL http://dx.doi.org/10.1038/nnano.2008.211.

[92] PISCANEC, S., LAZZERI, M., MAURI, F., AND FERRARI, A. C., *Optical phonons of graphene and nanotubes*. Eur. Phys. J. ST **148** (2007) 159–170. URL http://dx.doi.org/10.1140/epjst/e2007-00236-2.

[93] POP, E., MANN, D., WANG, Q., GOODSON, K., AND DAI, H., *Thermal Conductance of an Individual Single-Wall Carbon Nanotube above Room Temperature*. Nano Lett. **6** (2006) 96–100. URL http://dx.doi.org/10.1021/nl052145f.

[94] RADUSHKEVICH, L. V. AND LUKYANOVICH, V. M., *O strukture ugleroda obrazujucegosja pri termiceskom razlozenii okisi ugleroda na zeleznom kontakte*. Soviet journal of Physical Chemistry **26** (1952).

[95] RAFIEE, J., MI, X., GULLAPALLI, H., THOMAS, A. V., YAVARI, F., SHI, Y., AJAYAN, P. M., AND KORATKAR, N. A., *Wetting transparency of graphene*. Nat. Mater. **11** (2012) 217–222. URL http://dx.doi.org/10.1038/nmat3228.

[96] RANADE, M. B., *Adhesion and Removal of Fine Particles on Surfaces*. Aerosol Sci. Tech. **7** (1987) 161–176. URL http://dx.doi.org/10.1080/02786828708959155.

[97] REBELO, S. L. H., GUEDES, A., SZEFCZYK, M. E., PEREIRA, A. M., ARAÚJO, J. P., AND FREIRE, C., *Progress in the Raman spectra analysis of covalently functionalized multiwalled carbon nanotubes: unraveling disorder in graphitic materials*. Phys. Chem. Chem. Phys. **18** (2016) 12784–12796. URL http://dx.doi.org/10.1039/C5CP06519D.

[98] REIBOLD, M., PAUFLER, P., LEVIN, A. A., KOCHMANN, W., PÄTZKE, N., AND MEYER, D. C., *Materials: Carbon nanotubes in an ancient Damascus sabre*. Nature **444** (2006). URL http://dx.doi.org/10.1038/444286a.

[99] REN, Z. F., HUANG, Z. P., XU, J. W., WANG, J. H., BUSH, P., SIEGAL, M. P., AND PROVENCIO, P. N., *Synthesis of Large Arrays of Well-Aligned Carbon Nanotubes on Glass*. Science **282** (1998) 1105–1107. URL http://dx.doi.org/10.1126/science.282.5391.1105.

[100] RINKIÖ, M., JOHANSSON, A., PARAOANU, G. S., AND TÖRMÄ, P., *High-Speed Memory from Carbon Nanotube Field-Effect Transistors with High-$\kappa$ Gate Dielectric*. Nano Lett. **9** (2009) 643–647. URL http://dx.doi.org/10.1021/nl8029916.

[101] S. GERDES, T. ONDARÇUHU, S. CHOLET, AND C. JOACHIM, *Combing a carbon nanotube on a flat metal-insulator-metal nanojunction*. Europhys. Lett. **48** (1999) 292–298.

[102] SAITO, R., DRESSELHAUS, G., AND DRESSELHAUS, M. S., *Physical Properties of Carbon Nanotubes* (Imperial College Press, London, 1998).

[103] SAMPO, J., TAKALO, J., SILTANEN, S., MIETTINEN, A., LASSAS, M., AND TIMONEN, J., *Curvelet-based method for orientation estimation of particles from optical images*. Opt. Eng. **53** (2014) 033109. URL http://dx.doi.org/10.1117/1.OE.53.3.033109.

[104] SHANG, J., FLURY, M., AND DENG, Y., *Force measurements between particles and the air-water interface: Implications for particle mobilization in unsaturated porous media*. Water Resources Research **45** (2009). URL http://dx.doi.org/10.1029/2008WR007384.

[105] SHANMUGASUNDARAM, K., CHANG, K., SHALLENBERGER, J., DANEL, A., TARDIF, F., VEILLEROT, M., AND RUZYELLO, J., *Reversing of silicon surface aging by lamp cleaning*, in *Cleaning Technology In Semiconductor Device Manufacturing VIII*, edited by J. Ruzyllo, T. Hattori, R. Opila, and R. Novak (The Electrochemical Society, Inc., 2003), vol. PV 2003-26 of *ECS Proceedings*, pp. 348–350.

[106] SHARMA, P., FLURY, M., AND ZHOU, J., *Detachment of colloids from a solid surface by a moving air-water interface*. J. Colloid Interface Sci. **326** (2008) 143–150. URL http://dx.doi.org/10.1016/j.jcis.2008.07.030.

[107] SHIN, Y. J., WANG, Y., HUANG, H., KALON, G., WEE, A. T. S., SHEN, Z., BHATIA, C. S., AND YANG, H., *Surface-Energy Engineering of Graphene*. Langmuir **26** (2010) 3798–3802. URL http://dx.doi.org/10.1021/la100231u.

[108] SINGH, P. AND JOSEPH, D., *Fluid dynamics of floating particles*. J. Fluid Mech **530** (2005) 31–80. URL http://dx.doi.org/10.1017/S0022112005003575.

[109] SMALLEY, R. E., LI, Y., MOORE, V. C., PRICE, B. K., COLORADO, J. R., SCHMIDT, H. K., HAUGE, R. H., BARRON, A. R., AND TOUR, J. M., *Single Wall Carbon Nanotube Amplification: En Route to a Type-Specific Growth Mechanism*. J. Am. Chem. Soc. **128** (2006) 15824–15829. URL http://dx.doi.org/10.1021/ja065767r.

[110] SPUDAT, C., MÜLLER, M., HOUBEN, L., MAULTZSCH, J., GOSS, K., THOMSEN, C., SCNEIDER, C. M., AND MEYER, C., *Observation of Breathing-like Modes in an Individual Multiwalled Carbon Nanotube*. Nano Lett. **10** (2010) 4470–4474. URL http://dx.doi.org/10.1021/nl102305a.

[111] SUÁREZ, C. G., NOORDMANS, J., VAN DER MEI, H. C., AND BUSSCHER, H. J., *Removal of Colloidal Particles from Quartz Collector Surfaces As Stimulated by the Passage of Liquid-Air Interfaces*. Langmuir **15** (1999) 5123–5127. URL http://dx.doi.org/10.1021/la981608c.

[112] TANNER, L. H., *The spreading of silicone oil drops on horizontal surfaces*. J. Phys. D: Appl. Phys. **12** (1979) 1473. URL http://stacks.iop.org/0022-3727/12/i=9/a=009.

[113] TARKIAINEN, R., AHLSKOG, M., ZYUZIN, A., HAKONEN, P., AND PAALANEN, M., *Transport in strongly disordered multiwalled carbon nanotubes*. Phys. Rev. B **69** (2004) 033402. URL http://dx.doi.org/10.1103/PhysRevB.69.033402.

[114] THESS, A., LEE, R., NIKOLAEV, P., DAI, H. J., PETIT, P., ROBERT, J., XU, C. H., LEE, Y. H., KIM, S. G., RINZLER, A. G., COLBERT, D. T., SCUSERIA, G. E., TOMANEK, D., FISCHER, J. E., AND SMALLEY, R. E., *Crystalline Ropes of Metallic Carbon Nanotubes*. Science **273** (1996) 483–487. URL http://dx.doi.org/10.1126/science.273.5274.483.

[115] THOSTENSON, E. T., LI, C., AND CHOU, T.-W., *Nanocomposites in context*. Compos. Sci. Technol. **65** (2005) 491–516. JNC13-AMAC-Strasbourg, URL http://dx.doi.org/10.1016/j.compscitech.2004.11.003.

[116] TRONEL-PEYROZ, E. AND LHASSANI, A., *Interpretation of the Contact Angle Data of Binary Liquids Mixtures with a Modified Equation of state for Interfacial Tensions*. J. Colloid Interface Sci. **171** (1995) 522–524. URL http://dx.doi.org/10.1006/jcis.1995.1213.

[117] VAZQUEZ, G., ALVAREZ, E., AND NAVAZA, J. M., *Surface Tension of Alcohol Water + Water from 20 to 50 °C*. J. Chem. Eng. Data **40** (1995) 611–614. URL http://dx.doi.org/10.1021/je00019a016.

[118] VISSER, J., *The Adhesion of Colloidal Particles to a Planar Surface in Aqueous Solutions*, Ph.D. thesis, Council for National Academic Awards, London (1973).

[119] WANG, M. AND REVIL, A., *Electrochemical charge of silica surfaces at high ionic strength in narrow channels*. J. Colloid Interface Sci. **343** (2010) 381–386. URL http://dx.doi.org/10.1016/j.jcis.2009.11.039.

[120] Y.-H. LIU, S. M., H. MARUYAMA, *Effect of Particle Impact on Surface Cleaning Using Dry Ice Jet*. Aerosol Sci. Tech. **45** (2011) 1519–1527. URL http://dx.doi.org/10.1080/02786826.2011.603769.

[121] YANG, Y. H. AND LI, W. Z., *Radial elasticity of single-walled carbon nanotube measured by atomic force microscopy*. Appl. Phys. Lett. **98** (2011). URL http://dx.doi.org/10.1063/1.3546170.

[122] YANG, Z.-P., CI, L., BUR, J. A., LIN, S.-Y., AND AJAYAN, P. M., *Experimental Observation of an Extremely Dark Material Made By a Low-Density Nanotube Array*. Nano Lett. **8** (2008) 446–451. URL http://dx.doi.org/10.1021/nl072369t.

[123] YI, P. AND CHEN, K. L., *Influence of Solution Chemistry on the Release of Multiwalled Carbon Nanotubes from Silica Surfaces*. Environ. Sci. Technol. **47** (2013) 12211–12218. URL http://dx.doi.org/10.1021/es403133r.

[124] YI, P. AND CHEN, K. L., *Release Kinetics of Multiwalled Carbon Nanotubes Deposited on Silica Surfaces: Quartz Crystal Microbalance with Dissipation (QCM-D) Measurements and Modeling*. Environ. Sci. Technol. **48** (2014) 4406–4413. URL http://dx.doi.org/10.1021/es405471u.

[125] YOTPRAYOONSAK, P., SZILVAY, G. R., LAAKSONEN, P., LINDER, M. B., AND AHLSKOG, M., *The Effect of Hydrophobin Protein on Conductive Properties of Carbon Nanotube Field-Effect Transistors: First Study on Sensing Mechanism*. J. Nanosci. Nanotechnol. **15** (2015) 2079–2087. URL http://dx.doi.org/10.1166/jnn.2015.10337.

[126] YOUNG, T., *An Essay on the Cohesion of Fluids*. Philos. Trans. Soc. London **95** (1805) 65–87. URL http://dx.doi.org/10.1098/rstl.1805.0005.

[127] YU, M., CHEN, S., ZHANG, B., QIU, D., AND CUI, S., *Why a Lotus-like Superhydrophobic Surface Is Self-Cleaning? An Explanation from Surface Force Measurements and Analysis*. Langmuir **30** (2014) 13615–13621. URL http://dx.doi.org/10.1021/la5041272.

[128] YU, M.-F., LOURIE, O., DYER, M. J., MOLONI, K., KELLY, T. F., AND RUOFF, R. S., *Strength and Breaking Mechanism of Multiwalled Carbon Nanotubes Under Tensile Load*. Science **287** (2000) 637–640. URL http://dx.doi.org/10.1126/science.287.5453.637.

[129] ZAITSEV, S., SHTEMPLUCK, O., AND BUKS, E., *Effects of electron beam induced carbon deposition on the mechanical properties of a micromechanical oscillator*. Sensor. Actuat. A-Phys **179** (2012) 237–241. URL http://dx.doi.org/10.1016/j.sna.2012.02.039.

[130] ZHANG, H. AND HAN, S., *Viscosity and Density of Water + Sodium Chloride + Potassium Chloride Solutions at 298.15 K*. J. Chem. Eng. Data **41** (1996) 516–520. URL http://dx.doi.org/10.1021/je9501402.

[131] ZHAO, X., ANDO, Y., QIN, L.-C., KATAURA, H., MANIWA, Y., AND SAITO, R., *Multiple splitting of G-band modes from individual multiwalled carbon nanotubes*. Appl. Phys. Lett. **81** (2002) 2550–2552. URL `http://dx.doi.org/10.1063/1.1502196`.